

UNCONFINED FLAME SYNTHESIS OF MONO-LAYER GRAPHENE AND OTHER  
NANOSTRUCTURED MATERIALS

by

HUA HONG

A dissertation submitted to the

Graduate School-New Brunswick

Rutgers, The State University of New Jersey

In partial fulfillment of the requirements

For the degree of

Doctor of Philosophy

Graduate Program in Mechanical and Aerospace Engineering

Written under the direction of

Stephen D. Tse

And approved by

---

---

---

---

New Brunswick, New Jersey

October, 2017

## ABSTRACT OF THE DISSERTATION

Unconfined Flame Synthesis of Mono-layer Graphene and Other Nanostructured

Materials

By HUA HONG

Dissertation Director:

Stephen D. Tse

A modified multi-element inverse-diffusion flames (m-IDFs) burner setup is utilized to synthesize mono-layer graphene and carbon nanotubes (CNTs) on metal and non-metal substrates. The growth mechanisms of mono-, bi-, and few-layer graphene (MLG, BLG, and FLG, respectively) and their defect level using unconfined flame synthesis is investigated, with systematic variation of parameters such as substrate material, temperature, growth time, carbon precursor, and hydrogen flow rate. In-situ Raman measurement is employed to observe the evolution of the gas-phase precursor species in the synthesis flow. The growth of graphene on copper is observed for a wide range of temperatures ranging from 850 °C to 1000 °C, with high-quality graphene produced at 1000 °C. An effective etching phenomenon on graphene layers reducing the number of layers is uncovered in a post-growth hydrogen annealing process using the same setup, where the

hydrocarbon precursor flow is turned off, but the hydrogen m-IDFs are maintained. Such effect enables the growth of MLG in an open-atmosphere environment for the first time.

The effects of hydrogen annealing on graphene with different starting qualities and substrates are investigated. The hydrogen annealing technique can also be utilized to create defects (depending on the critical initial defect level) such as nanoscale pores and vacancies in the graphene layer(s). The critical D-peak-to-G-peak intensity ( $I_D/I_G$ ) ratio found in this work is  $\sim 0.6$ . The  $I_D/I_G$  ratio increases dramatically after hydrogen annealing when as-synthesized graphene on Cu exhibits an initial ratio of at least 0.6. However, the  $I_D/I_G$  ratio does not change obviously after annealing if the initial ratio is lower than 0.6. By controlling the annealing condition, highly-defective graphene films with tunable defects are directly synthesized using a two-step flame method. Such defective graphene is important in its own right (compared to single-crystal graphene), as it has a myriad of applications, such as ultrafiltering membranes, gas sensors, and optoelectronics. Here, graphene-based ion-selective membranes are fabricated and preliminarily tested for permeability and ion rejection rate.

Using the same setup, carbon nanotube (CNT) growth is examined on silicon wafers with pre-deposited catalytic nanoparticle seeds. Different seeding recipes and processes are used to study the effects of catalytic nanoparticles on CNT growth on non-metal substrates using flame synthesis. The transition from growing iron oxide nanocrystals to CNTs on stainless-steel substrates with different carbon content is studied. At low temperature (e.g., 500 °C) the growth of uniform  $\alpha$ -Fe<sub>2</sub>O<sub>3</sub> nanoparticle films is found on

alloys of 304, 304L, and 316L stainless steel. On the other hand, at high temperature (e.g., 850 °C), the growth of CNTs are observed on 304 stainless steel because of the carbide-induced breakup of the surface, but not on 316L, whose carbon content is much lower. In addition, the growth of CNTs and  $\gamma$ -Fe<sub>2</sub>O<sub>3</sub> hybrid materials is achieved by performing a two-step flame synthesis, where the temperature is initially set at 500 °C and then tuned to 850 °C. Such hybrid materials afford applications in many areas, such as batteries and sensors.

## Preface

The bulk of this thesis focuses on the fundamental study of the flame synthesis of nanostructured carbon materials, using unconfined flame setup, parametric-study method, and advanced in-situ and ex-situ characterization techniques. Much of the content in Chapters 4, 5, 6, 7 is verbatim from soon to be submitted for publication papers [1-3], and the permission to include the collaborative work in my thesis is obtained from the co-authors. In addition, other chapters contain wording similar or identical to that in the paper referenced below.

## References

- [1] Hong, H., Xiong, G., Dong, Z., Kear, B., and Tse, S., “Unconfined Flame Synthesis of Monolayer and Bilayer Graphene in Open Atmosphere,” Manuscript prepared.
- [2] Hong, H., Cetindag, S., Pennington, A., Dong, Z., Xiong, G., Kear, B., and Tse, S., “Hydrogen-Post-Treated Flame Synthesis of Highly-Defective Graphene and Its Properties,” Manuscript prepared.
- [3] Memon, N., Hong, H., Al-Sharab, J., Kear, B., and Tse, S., “Selective Growth of  $\gamma$ -Fe<sub>2</sub>O<sub>3</sub> Nanocrystal Films on Stainless Steel Using Flame Synthesis,” Manuscript prepared.

## Acknowledgements

I would like to express my sincere thanks to my advisor, Professor Stephen Tse, and to my co-advisor, Professor Bernard Kear. Dr. Tse's knowledge, intelligence, and creativity provided me with an abundant and productive graduate experience. I thank him for providing me the opportunity to work on interdisciplinary projects in a collaborative environment, which motivated me to study in a broad range and work at a higher level. In addition to his guidance, I am very thankful for the encouragement and support he gave me since I joined Rutgers as a Master student. I am also very fortunate to have Dr. Kear as a co-advisor. I owe a great deal to him, who, in addition to providing expert advice and expertise throughout my doctoral work, broadened my horizons to the impact of research. I also owe thanks to Professor Jerry Shan and Professor Assimina Pelegri for their assistance in our collaborative work and kindly help during my graduate life.

I could never achieve my research goal without the help of numerous people. Firstly, I would like to thank Dr. Gang Xiong and Dr. Zhizhong Dong for all their counseling and assistance for my research work. I would also like to thank Nasir Memon, William Mozet, Robert Horvath, Yuqian Zhang, Tianyin Xia, Hadi Halim, Mustafa Mozael, and all my excellent lab mates, who gave me a lot of support in these years. I also want to thank Semih Cetindag, Max Tenorio, and Ashley Pennington for providing their expertise in our collaborations. I also want to thank John Petrowski for his assistance in building my experimental setup.

The financial support from the National Science Foundation (grant CBET-1249259), Army Research Office (grant W911NF-17-1-0111), and teaching assistantships from the Mechanical and Aerospace Engineering Department at Rutgers University are gratefully acknowledged.

I am extremely grateful to my family for supporting me in my decision to live and study abroad for ten years. Thank you, Mom and Dad, for your endless support and encouragement as I pursued my dreams. At last, special thanks to my wife, Duo, for her love and support.

## Table of Contents

ABSTRACT OF THE DISSERTATION .....	ii
Preface.....	v
Acknowledgements.....	vi
Table of Contents .....	viii
List of Tables.....	xiv
List of Illustrations.....	xv
Chapter 1 .....	1
1. Introduction.....	1
1.1 Motivation.....	2
1.2 Research Innovation.....	3
1.3 Research Objective .....	6
1.4 Approach.....	10
1.5 Outline of this dissertation .....	11
Chapter 2.....	13
2. Literature Review.....	13
2.1 Introduction.....	13
2.2 Graphene Background .....	15
2.2.1 Graphene fundamentals.....	15
2.2.1.1 <i>Electrical properties</i> .....	17
2.2.1.2 <i>Thermal properties</i> .....	18
2.2.1.3 <i>Mechanical properties</i> .....	20



2.2.1.4	<i>Optical properties</i>	21
2.2.2	Graphene synthesis	22
2.2.2.1	<i>Micromechanical cleavage</i>	23
2.2.2.2	<i>Liquid-phase exfoliation</i>	23
2.2.2.3	<i>Epitaxial growth on silicon carbide (SiC)</i>	25
2.2.2.4	<i>Chemical vapor deposition (CVD)</i>	26
2.2.2.5	<i>Plasma synthesis</i>	33
2.2.3	Graphene applications	34
2.2.3.1	<i>Electronics</i>	34
2.2.3.3	<i>Membranes</i>	37
2.3	Carbon Nanotube Background	40
2.3.1	Carbon Nanotube Fundamentals	40
2.3.1.1	<i>CNT properties</i>	40
2.3.2	CNT Synthesis	43
2.3.2.1	<i>Arc-discharge</i>	43
2.3.2.2	<i>Laser ablation</i>	44
2.3.2.3	<i>Chemical vapor deposition (CVD)</i>	45
2.3.3	Carbon Nanotubes Applications	46
2.3.3.1	<i>Transistors</i>	46
2.3.3.2	<i>Composites</i>	47
2.4	Flame Synthesis Background	48
2.4.1	Flame Synthesis of Nanostructured Metal Oxides	49
2.4.2	Flame Synthesis of Nanostructured Carbon	51

2.4.2.1	<i>Flame synthesis of carbon nanotubes (CNTs)</i>	52
2.4.2.2	<i>Flame synthesis of graphene</i>	54
2.5	Summary	56
Chapter 3		57
3.	Experimental Setup	57
3.1	Modified Multi-Element Inverse-Diffusion Flame Burner	57
3.2	Numerical Simulation	59
3.3	Temperature Measurement	61
3.4	Experimental Procedures	61
3.5	Sample Preparation	61
3.6	In-situ Raman Spectroscopy	62
3.7	Ex-situ Characterization Techniques	63
3.7.1	Raman Spectroscopy	64
3.7.2	Scanning Electron Microscopy	67
3.7.3	Transmission Electron Microscopy	68
3.7.4	Atomic-Force Microscopy	68
3.7.5	X-ray Photoelectron Microscopy	69
3.7.6	X-ray Diffraction	69
Chapter 4		71
4.	Fundamental Study of Graphene Growth Conditions Using Unconfined Flame Synthesis	71
4.1	Introduction	71
4.2	Experiment	74

4.3	Results and Discussion .....	75
4.3.1	Effect of Substrate Temperature .....	76
4.3.2	Effect of Methane-to-Hydrogen Flow Rate ( $J_{CH_4}:J_{H_2}$ ) Ratio .....	78
4.3.3	Effect of Growth Time.....	80
4.3.4	Effect of Substrate Material.....	82
4.3.5	Effect of Hydrocarbon Precursor.....	85
4.3.6	Effect of Flow Field Profile.....	87
4.3.7	Effect of Transfer Process .....	90
4.3.8	In-situ Raman Spectroscopy of Gas-phase Species Profile.....	91
4.4	Concluding Remarks.....	95
Chapter 5 .....		96
5.	Hydrogen-Post-Treated Flame Synthesis of Monolayer Graphene in Open- Atmosphere .....	96
5.1	Introduction.....	96
5.2	Experiment.....	98
5.3	Results and Discussion .....	100
5.4	Concluding Remarks.....	104
Chapter 6 .....		106
6.	Effect of Hydrogen Annealing on Flame-Synthesized Graphene and Direct Synthesis of Highly Defective Graphene.....	106
6.1	Introduction.....	106
6.2	Experiment.....	109
6.3	Results and Discussion .....	112

6.3.1	Effect of Hydrogen Annealing on Graphene with Different Substrates	112
6.3.2	Direct Synthesis of Highly Defective Graphene .....	115
6.3.3	Potential Applications of Highly Defective Graphene .....	124
6.4	Concluding Remarks.....	127
Chapter 7	.....	129
7.	Unconfined Flame Synthesis of CNTs on Metals and Nonmetals.....	129
7.1	Introduction.....	129
7.2	Experiment.....	131
7.3	Results and Discussion .....	135
7.3.1	Synthesis of CNTs and Iron Oxide Nanoparticles on Stainless Steel	135
7.3.1.1	<i>Low-Temperature growth of <math>\alpha</math>-Fe<sub>2</sub>O<sub>3</sub> Nanoparticle Film .....</i>	135
7.3.1.2	<i>High-Temperature growth of <math>\gamma</math>-Fe<sub>2</sub>O<sub>3</sub> Nanocrystals, and CNTs</i>	140
7.3.1.3	<i>Two-step growth of <math>\gamma</math>-Fe<sub>2</sub>O<sub>3</sub> Nanocrystals and CNTs Hybrid Materials .....</i>	142
7.3.2	CNT Synthesis on Non-metal Substrate.....	144
7.3.2.1	<i>CNT growth using iron catalyst .....</i>	144
7.3.2.2	<i>CNT growth using Co-Mo co-catalyst .....</i>	148
7.4	Concluding Remarks.....	151
Chapter 8	.....	153
8.	Conclusions.....	153
8.1	Summary of Results .....	153

8.2	Suggestions for Future Work .....	159
	References .....	162

## List of Tables

Table 2.1 History of carbon materials (reproduced from [1]).....	14
Table 2.2 Elastic modulus, specific modulus and cost of various CNT and CF reinforced composites (reproduced with caption from [2]) .....	48
Table 3.1 List of substrate investigated.....	62
Table 3.2 List of characterization techniques .....	64
Table 6.1 Band energies of defective graphene with different ID/IG ratio.....	121
Table 6.2 Results of conductance measurements and estimated open-area diameter and percentage respect to different $I_D/I_G$ ratios.....	126
Table 7.1 Chemical composition of various types of stainless steel.....	133
Table 7.2 Gibbs free energies of reactions, calculated with thermochemical data from NIST-JANAF tables (1998) at 1 atm, for the investigated growth of $\alpha$ -Fe <sub>2</sub> O <sub>3</sub> .....	136
Table 7.3 Elemental analysis using EDS on SEM. ....	148
Table 7.4 Gibbs free energies of reactions, calculated with thermochemical data from NIST-JANAF tables (1998) at 1 atm, for the investigated growth of CoO. ....	150

## List of Illustrations

Figure 1.1 a) Schematic diagram of m-IDF burner used in flame synthesis of few-layer graphene (reproduced with caption from [4]). Hydrogen and hydrocarbon precursor are delivered in the same fuel passageways. b) Schematic diagram of m-IDF burner modified with multiple distinct precursor delivery tubes staged above the m-IDF burner surface. Hydrocarbon precursors are delivered into the post-flame region and directed at a substrate. ....	5
Figure 1.2 Scheme of general approach used in this study for flame synthesis of nanocarbon. ....	11
Figure 2.1 Structures of selected carbon allotropes (reproduced from [5]). ....	13
Figure 2.2 Graphene is a 2D building material for carbon materials of all other dimensionalities. It can be wrapped up into 0D buckyballs, rolled into 1D nanotubes or stacked into 3D graphite (reproduced with caption from [6]). ....	16
Figure 2.3 Bandgap in graphene. Schematic diagrams of the lattice structure of (A) monolayer and (B) bilayer graphene. The green and red colored lattice sites indicate the A (A1/A2) and B (B1/B2) atoms of monolayer (bilayer) graphene, respectively. The diagrams represent the calculated energy dispersion relations in the low-energy regime and show that monolayer and bilayer graphene are zero-gap semiconductors. (C) When an electric field (E) is applied perpendicular to the bilayer, a band gap is opened up in bilayer graphene, whose size ( $2\Delta$ ) is tunable by the electric field. (reproduced with caption from [7]) .....	18

Figure 2.4 (a) Raman spectrum of suspended graphene. (b) Optical microscope and (c) scanning electron microscopy images of suspended graphene sample. The scale bars are 10  $\mu\text{m}$ . (d) Schematic diagram of the experimental setup for thermal conductivity measurement of graphene using Raman spectroscopy (reproduced with caption from [8])..... 19

Figure 2.5 (A) Scanning electron micrograph of a large graphene flake spanning an array of circular holes 1  $\mu\text{m}$  and 1.5  $\mu\text{m}$  in diameter. (B) Noncontact mode AFM image of one membrane. The solid blue line is a height profile along the dashed line. The step height at the edge of the membrane is about 2.5 nm. (C) Schematic of nanoindentation on suspended graphene membrane. (D) AFM image of a fractured membrane. (reproduced with caption from [9])..... 20

Figure 2.6 Looking through one-atom-thick crystals. (A) Photograph of a 50- $\mu\text{m}$  aperture partially covered by graphene and its bilayer. The line scan profile shows the intensity of transmitted white light along the yellow line. (B) Transmittance spectrum of single-layer graphene (open circles). Slightly lower transmittance for  $\lambda < 500$  nm is probably due to hydrocarbon contamination. The red line is transmittance  $T = (1 + 0.5\pi\alpha)$  expected for two-dimensional Dirac fermions, whereas the green curve takes into account a nonlinearity and triangular warping of graphene's electronic spectrum. The gray area indicates the standard error of our measurements. (Inset) The transmittance of white light as a function of the number of graphene layers. (reproduced with caption from [10])..... 21



Figure 2.7 Schematic of two main approaches used in graphene synthesis: Top-down approach and Bottom-up approach. ....	22
Figure 2.8 Mechanical cleavage of graphene using scotch tape from HOPG. (reproduced with caption from [11]). ....	23
Figure 2.9 (A) Schematic illustration of the graphene chemical exfoliation process. (B) Photograph of graphene dispersion in solution (reproduced with caption from [11])	24
Figure 2.10 a, A commercial model high-shear mixer with mixing head (b) and rotor and stator (c). d, Graphene-NMP dispersions produced by shear exfoliation (reproduced with caption from [12]). ....	25
Figure 2.11 (A) Processes involved in graphene synthesis using low carbon solid solubility catalysts (Cu) in a CVD process. (B) Mass transport and surface reaction fluxes under steady state conditions (reproduced with caption from [13]). ....	28
Figure 2.12 (A) Schematic of roll-to-roll production of graphene films grown on a copper foil. The process includes adhesion of polymer supports, copper etching (rinsing) and dry transfer-printing on a target substrate. (B) Photographs of the roll-to-roll process. (C) A 30-inch graphene film transferred on a 35-inch PET sheet. (D) A touch screen made of graphene/PET film. (reproduced with caption from [14]). ....	29
Figure 2.13 In situ SEM images recorded at 1000 °C during LPCVD growth showing the nucleation and growth of carbon sheets (characterized by darker contrast). White arrows highlight nucleation events at grain boundaries. $t^*$ corresponds to the induction period from $C_2H_4$ dosing until the first nucleation events can be detected.	

Growing graphene sheets are characterized by a dark contrast. The smooth contrast of the copper surface is due to a sublimation-induced surface buckling. Grain boundaries in the copper foil are highlighted by green dotted lines in the top left image. Differences in contrast for different grains are due to electron channeling. The scale bar measures 5 $\mu\text{m}$ (reproduced with caption from [15]).	31
Figure 2.14 Processes for transfer of graphene films (“Gr” = graphene). The top-right and bottom-left insets are the optical micrographs of graphene transferred on $\text{SiO}_2/\text{Si}$ wafers (285 nm thick $\text{SiO}_2$ layer) with “bad” and “good” transfer, respectively. The bottom-right is a photograph of a $4.5 \times 4.5 \text{ cm}^2$ graphene on a quartz substrate (reproduced with caption from [16]).	33
Figure 2.15 Schematic diagram illustrating the structure of graphene, NG and GO membrane, the mechanism for selective mass transmembrane transport and possible uses (reproduced with caption from [17]).	38
Figure 2.16 a, Detection of changes in the ionic current through a nanopore in a graphene membrane due to the passage of a DNA molecule. b, Modulations of a tunnelling current through a nanogap between two graphene electrodes due to the presence of a DNA molecule. c, Variations in the in-plane current through a graphene nanoribbon due to traversal of a DNA molecule. d, Changes in a graphene current due to the physisorption of DNA bases onto the graphene (reproduced with caption from [18])	39

Figure 2.17. Schematic honeycomb structure of a graphene sheet, Carbon atoms are at the vertices. SWNTs can be formed by folding the sheet along lattice vectors. The two basis vectors $a_1$ and $a_2$ , and several examples of the lattice vectors are shown (reproduced with caption from [19]).	42
Figure 2.18 Schematic structures of SWNTs. (a) A (10,10) arm-chair nanotube (metallic nanotube). (b) A (12, 0) zigzag nanotube (a small band gap can develop due to the curvature of the nanotube). (c) The (14, 0) zigzag tube (semiconducting nanotube). (d) A (7, 16) tube is semiconducting. This figure illustrates the extreme sensitivity of nanotube electronic structures to the diameter and chirality of nanotubes (reproduced with caption from [19]).	42
Figure 2.19 (A) Schematic illustration of the arc-discharge method for CNT synthesis. (B) Schematic of the laser ablation process for CNT synthesis (reproduced with caption form [20])	44
Figure 2.20 Schematic of various typical flame configurations used for nanomaterials synthesis (reproduced with caption from [21]).	51
Figure 2.21 Schematic of the flame synthesis of FLG film using a) dual flame method, b) multiple inverse-diffusion flame method (reproduced with captions from [4], [22])	55
Figure 3.1 Schematic diagram of a modified m-IDF setup modified with uniform-distributed precursor tubes staged above the burner surface at a fixed height.	58
Figure 3.2 Screenshot of LabVIEW program for controlling MFCs.	59

Figure 3.3 Fluent Computation Fluid Dynamics (CFD) simulation results of the m-IDF burner at adiabatic boundary condition using two-step laminar reaction mechanism (a), constant temperature boundary condition (1600 K) using GRI-Mech 1.2 mechanism (b).....	60
Figure 3.4 Schematic diagram of the in-situ Raman measurement setup. The burner is located on a 2-D translator in order to move in x and z directions. The emissions are collected at 90° by a 400-mm focal-length achromatic lens, passed through a Raman holographic notch filter (Kaiser HSPF-532.0-2.0), focused by a 300-mm focal-length achromatic lens onto the slit of a 0.5m imaging spectrometer.....	63
Figure 3.5 A) Illustration of energy transitions leading to Rayleigh, Stokes and Anti-Stokes spectra. B) Schematic Raman scattering spectrum showing Rayleigh line, Stokes and Anti-Stokes Raman lines (reproduced with caption from [23], [24]).....	65
Figure 3.6 Raman spectra of graphite, metallic and semiconducting CNTs, low and high sp <sup>3</sup> amorphous carbons (reproduced with caption from [25]). .....	66
Figure 3.7 Raman spectrum of a graphene edge using 514 nm excitation (reproduced with caption from [26]). .....	67
Figure 3.8 Raman spectra of graphene with various numbers of layers (reproduced with caption from [27]). .....	67
Figure 4.1 Growth kinetics on CVD-produced graphene on various catalysts: Case of CH <sub>4</sub> on Ni and Cu (reproduced with caption from [28]). .....	72

Figure 4.2 The modified m-IDF setup provides fuel-rich hydrogen flame and active carbon species leading to graphene growth on Cu substrate in open-atmosphere.....	74
Figure 4.3 Raman spectra of graphitic carbon structure grown on Cu at low-temperature range from 700 °C to 850 °C. Substrate background signals are all subtracted. The spectra are normalized with the G band.....	77
Figure 4.4 Raman spectra of graphene grown on Cu at different temperatures. Substrate background signals are all subtracted. The spectra are normalized with the G band. ....	78
Figure 4.5 Raman spectra of graphene grown on Cu at different $J_{CH_4}:J_{H_2}$ ratios. Substrate background signals are all subtracted. The spectra are normalized with the G band.....	80
Figure 4.6 Raman spectra of graphene grown on Cu at different growth time. Substrate background signals are all subtracted. The spectra are normalized with the G band. ....	82
Figure 4.7 Raman spectra of graphene grown on different substrates. Substrate background signals are all subtracted. The spectra are normalized with the G band. ....	84
Figure 4.8 Raman spectra of graphene grown on different substrates. Substrate background signals are all subtracted. The spectra are normalized with the G band. ....	85

Figure 4.9 Raman spectra of graphene grown on Cu using $C_2H_4$ and $C_2H_2$ . Substrate background signals are all subtracted. The spectra are normalized with the G band.	86
Figure 4.10 a) Schematic of the substrate placed perpendicular, tilted and parallel against the flow. b) Raman spectra of graphene grown on Cu with different orientations. Substrate background signals are all subtracted. The spectra are normalized with the G band.	89
Figure 4.11 Streamline of the velocities in a CFD simulation of stagnation flow. The inset chart shows the velocity versus axial position with a zoom-in around the zero point.	90
Figure 4.12 Raman spectra of a BLG sample sitting on Cu and Si/SiO <sub>2</sub> before and after the transfer process. Substrate background signals are all subtracted. The spectra are normalized with the G band.	91
Figure 4.13 In-situ Raman signals of hydrocarbon species (a) as well as hydrogen and water vapor (b) evolved along the flow axis from the exits of precursor tubes to substrate. The position 0 mm corresponds to the exits of precursor tubes, while 5 mm corresponds to the lower edge of the substrate.	94
Figure 5.1 Schematic of two-step flame synthesis of monolayer graphene using modified m-IDF setup.	99
Figure 5.2 a) Typical Raman spectra of graphene sample before and after post-growth hydrogen annealing treatment. b) Single Lorentzian fitting of a Raman spectra from	

monolayer graphene sample. Substrate background signals are subtracted. The spectra are normalized with the G band.....	102
Figure 5.3 TEM images of monolayer graphene with different resolutions (a) (b). The top right inset shows the SAED pattern, and the top left inset shows magnified image of the hexagonal lattice in the circled edge (a). AFM image of monolayer graphene with highlight spots of residuals from transfer process (c).....	103
Figure 6.1 Schematic and SEM image of single-layer graphene suspended on a 5- $\mu$ m-diameter hole. For nanoporous graphene fabrication, several approaches have been utilized: bombardment by ions, by electrons and via O <sub>2</sub> plasma treatment. b, Raman spectra (514 nm excitation) of suspended graphene after different exposure times to oxygen plasma (reproduced with caption form [29]). .....	107
Figure 6.2 a, b, Aberration-corrected STEM images of graphene after 1.5 s exposure to oxygen plasma. Pores with characteristic dimensions of $\sim 1$ nm are clearly seen. c, Raman spectra of graphene sample used for STEM imaging in a, b, which shows $I_D/I_G \approx 1$ (reproduced with caption form [29]). .....	108
Figure 6.3 a) Schematic of transferring defective graphene from Cu to pinhole substrate. b) Schematic of an electrochemical workstation for conductance measurements of defective graphene membranes. The top-right inset of (b) is a photo of the testing membrane.....	111
Figure 6.4 (a) Typical Raman spectra of few-layer graphene grown on nickel at 1000 °C. (b) Raman spectra of few-layer graphene on Si/SiO <sub>2</sub> using Pulse Laser Deposition at	

900 °C in vacuum (provided by William Mozet). Substrate background signals are subtracted. The spectra are normalized with the G band.....	114
Figure 6.5 Raman spectra of defective graphene with different hydrogen annealing time.	
Substrate background signal is subtracted. The spectra are normalized with the G band.....	118
Figure 6.6 a) High-resolution TEM image of flame-synthesized defective graphene captured by Room Temperature Scanning/Transmission Electron Microscope (FEI Talos F200X S/TEM, 200 kV). b) Enlarged image of the selected area (red circled) of (a). c) Enlarged TEM image of Fig. 5.3a. ....	
119	
Figure 6.7 Band energies of flame-synthesized defective graphene with Cu substrate at different post-growth hydrogen annealing time. The background from Cu Plasmonic resonance (580 nm) is subtracted for all the samples. ....	
121	
Figure 6.8 Normalized Kubelka Munk of Graphene samples, increasing time and increasing defects leads to a red-shift in the $\pi$ - $\pi^*$ transition of the aromatic C=C bond in graphene.....	
122	
Figure 6.9 Raman spectra of ultrasmooth Cu sample before and after hydrogen annealing. Ssubstrate background signal is subtracted. The spectra are normalized with the G band.....	
123	
Figure 7.1 Schematic diagram of m-IDF burner used to synthesize CNTs. ....	
132	
Figure 7.2 Fe 2p XPS spectrum is showing Fe <sub>3</sub> O <sub>4</sub> on raw surface of stainless steel.....	
134	



Figure 7.3 Iron oxide nanocrystalline film grown on stainless steel at a temperature of 500 °C. (a) SEM image shows the morphology of iron oxide nanocrystalline film stainless steel. The top right inset shows a magnified image of the film. The bottom right inset shows an optical image of the film. Raman spectrum confirms the  $\alpha$ -Fe<sub>2</sub>O<sub>3</sub> phase growth on 304 (b), 304L (c), 316L (d) stainless steel. .... 137

Figure 7.4 Fe 2p XPS spectrum is showing  $\alpha$ -Fe<sub>2</sub>O<sub>3</sub> for the nanocrystalline film growth on type 304 (a), 304L (c), 316L (e) stainless steel at 500 °C. Fe 2p XPS spectrum of the sample on type 304 (b), 304L (d), 316L (f) stainless steel after argon ion beam etching of the surface. It indicates the thickness of the  $\alpha$ -Fe<sub>2</sub>O<sub>3</sub> film is less than 5 nm. .... 139

Figure 7.5 SEM images for 850 °C high-temperature growth on stainless steel. (a) The growth of  $\gamma$ -Fe<sub>2</sub>O<sub>3</sub> nanocrystals is observed on type 316L stainless steel. (b) The growth of  $\gamma$ -Fe<sub>2</sub>O<sub>3</sub> nanocrystals with some rogue iron oxide nanorods is observed on type 304L stainless steel. (c) The growth of micro- and nanoscale carbon fibers and tubes are observed on the type 304 stainless steel. The top right insets show the magnified SEM image of the films. .... 141

Figure 7.6 XRD for 850 °C high-temperature growth on stainless steel. The growth of  $\gamma$ -Fe<sub>2</sub>O<sub>3</sub> is confirmed on type 316L (a), 304L (b) stainless steel with the appearance of iron background signals implying thin film growth of oxide layer. .... 142

Figure 7.7 (a) FESEM confirms the hybrid growth of CNTs and iron oxide nanocrystals on type 304 stainless steel using 500 °C-to-850 °C two-step growth process. The top

right inset shows the magnified SEM image of the film. (b) Raman spectrum is confirming the presences of carbon nanostructure and $\gamma$ -Fe <sub>2</sub> O <sub>3</sub> particles. ....	143
Figure 7.8 SEM image of flame synthesis of CNTs grown on a silicon wafer using 10 mMole/L FeCl <sub>3</sub> seeding solution (a), and 1 mMole/L FeCl <sub>3</sub> seeding solution (b). .	145
Figure 7.9 SEM image of CNTs grown on silicon wafers using 1 mMole/L FeCl <sub>3</sub> and 2 mMole/L ethylenediamine (C <sub>2</sub> H <sub>4</sub> (NH <sub>2</sub> ) <sub>2</sub> ) seeding solution for 10-min growth (a), and 20-min growth (b). ....	146
Figure 7.10 SEM image of CNTs grown on silicon wafers using 0.1 mMole/L FeCl <sub>3</sub> and 0.2 mMole/L ethylenediamine (C <sub>2</sub> H <sub>4</sub> (NH <sub>2</sub> ) <sub>2</sub> ) seeding solution. The top-right inset is an enlarged image of the selected area. ....	148
Figure 8.1 A scheme of graphene, h-BN and MoS <sub>2</sub> lateral and vertical heterostructures (reproduced with caption from [30]). ....	160

## Chapter 1

### 1. Introduction

Flame synthesis has been used for manufacturing fine powders since the 1940s, when fumed silica was first mass-produced and marketed under the name of Aerosil by Degussa AG (now Evonik) [31]. Today, flame synthesis is widely used in commercial production of nanoparticles; in descending order of production mass, they include: carbon blacks, pigmentary titania, zinc oxides, fumed silica and optical fibers, with a total annual production on the order of million metric tons [32]. A typical process of synthesizing ceramic powders is by hydrolysis of chloride-based precursor vapor injected into a flame. Flame processes readily provide the high temperatures needed for gas-phase synthesis. The key reasons flame synthesis is favored by large-scale manufactures are its scalability and relatively low cost.

Flame synthesis is currently used in producing various advanced nanomaterials, e.g., carbon nanotubes (CNTs) and nanoparticles with complex compositions [21]. However, most studies still focus on flame aerosol approach. Although chemical vapor deposition (CVD)-type flame synthesis of nanostructured carbon and metal oxides has been demonstrated in recent years, its ability for large production needs more development. Nevertheless, flame synthesis has the potential of extending its use into CVD-type

processes for the controllable growth of large-area nanomaterials on substrates and surfaces with advantages in scalability and cost.

### 1.1 Motivation

Graphene, as a single atomic sheet of  $sp^2$ -bonded carbon atoms in a honeycomb structure, is the basic structural element of other allotropes of carbon, including fullerenes (0-D), carbon nanotubes (1-D), carbon nanoribbons (2-D) and graphite (3-D). The zero-gap conical band structure and ballistic transport of charges make graphene one of the most promising materials for semiconductor and other electronic applications [33], [34]. Additionally, because of its unique optical property and excellent mechanical strength, graphene is an excellent material for use as a transparent conductive electrode in a wide range of flexible devices like solar cells [35], touch screens, and displays [14]. Currently, graphene can be produced by mechanical exfoliation, epitaxial growth on SiC annealed in ultrahigh vacuum (UHV), liquid-phase exfoliation, chemical vapor deposition (CVD), and plasma-enhanced CVD.

Carbon nanotubes (CNTs), in the form of 1-D nanostructures rolled from graphene nanoribbons, exhibit exceptional electrical, thermal, and mechanical properties. Current techniques developed to produce CNTs include arc discharge, laser ablation, plasma, and CVD. Carbon nanotubes are found naturally formed in hydrocarbon combustion process along with fullerenes and soot. However, the products are not well controlled in size and quality.

Because of the advantages in scalability, processing time, and cost, flame synthesis method has been widely employed in producing various metal-oxide and carbide nanostructures. Recent studies have revealed the capability of flame synthesis in producing various morphologies of CNTs and few-layer graphene in controlled flame environments. In the flame synthesis process, fuel serves as both the hydrocarbon reactant for growth and the energy source to elevate the temperature. Compared with current methods, flame synthesis method has advantages in growth rate, total yield density, scalability, and cost. Since the growth of high-quality nanostructured carbon films over large areas efficiently and economically remains a challenge, there is a strong need to develop an unconfined and cost-effective synthesis method suitable for mass production. Moreover, an investigation into the parameters of flame synthesis is necessary to understand the fundamentals and optimize the process.

## 1.2 Research Innovation

In previous studies, the multi-element inverse-diffusion flames (m-IDF) burner was utilized to synthesize few-layer graphene and CNTs on metal substrates by running multiple diffusion flames in an inverse mode (“under-ventilated”). However, monolayer and bilayer graphene samples were not achieved because of certain aspects of the setup. Hydrocarbon precursor was delivered along with hydrogen in the same passageways to the burner, where most hydrocarbon species decomposed when passing through the flame front (with a smaller portion reacting with the oxidizer in the flame zone of an individual inverse

diffusion flame; see Fig. 1.1a). The hydrocarbon precursor also served as fuel, and the total flow rate of fuel issuing through the burner had to be above a certain rate to stabilize each individual diffusion flame. Therefore, the precursor delivery rate and flame synthesis condition, which are two key factors for carbon nanomaterials growth, were coupled. Previous work reported that no graphene growth was observed when a low hydrocarbon/hydrogen ratio was issued through the burner (i.e.,  $< 1/40$ ). In order to decouple these two effects, we separate issuing of the hydrocarbon precursor from the hydrogen fuel. Here, a new synthesis configuration is designed and implemented by adding to the m-IDF burner multiple distinct precursor delivery tubes staged above the m-IDF burner surface (see Fig. 1.1b). Now, hydrocarbon species can be directly delivered downstream of the burner without passing through or near the flame front, thereby delaying decomposition of the precursor to limit the number of graphene layers formed on the substrate. The modified m-IDF burner can create radially-uniform temperature gradient and profiles of chemical species downstream of the burner. Using diffusion flames (burning stoichiometrically in the flame front) can avoid flame-speed considerations, flashback, and cellular instabilities associated with premixed flames. In short, hydrocarbon precursors are delivered into the post-flame region and directed at a substrate to grow carbon nanomaterials.

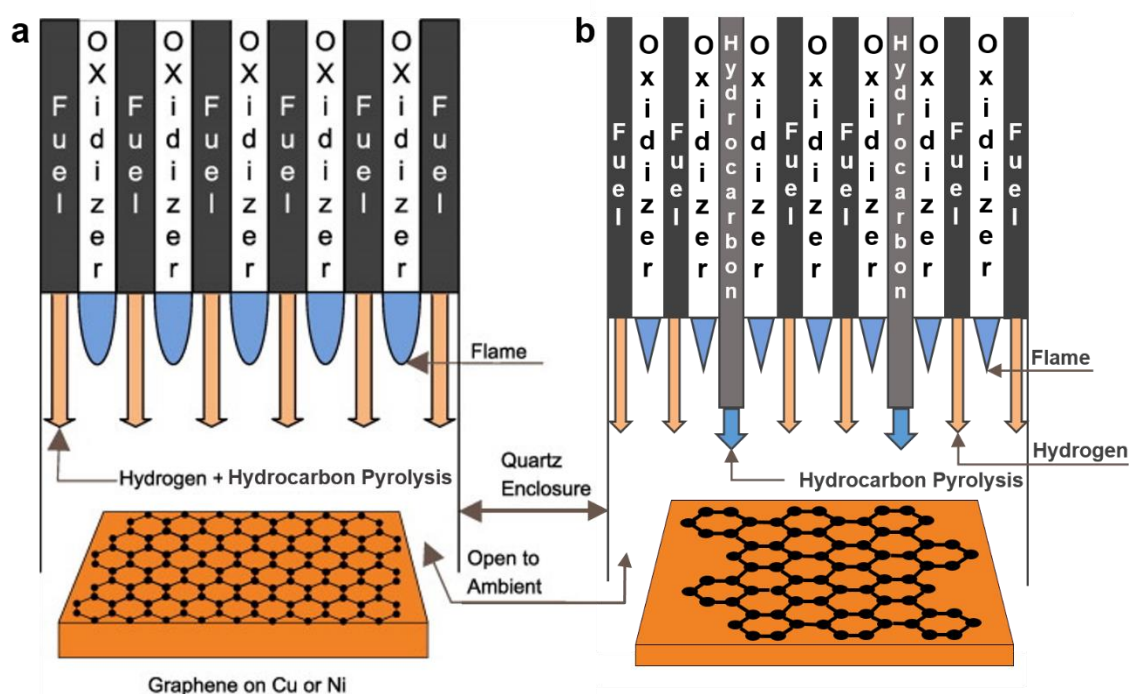


Figure 1.1 a) Schematic diagram of m-IDF burner used in flame synthesis of few-layer graphene (reproduced with caption from [4]). Hydrogen and hydrocarbon precursor are delivered in the same fuel passageways. b) Schematic diagram of m-IDF burner modified with multiple distinct precursor delivery tubes staged above the m-IDF burner surface. Hydrocarbon precursors are delivered into the post-flame region and directed at a substrate.

Unlike CVD process confined to a reaction chamber, flame synthesis can be operated in open environments because of the consumption of oxidizer at the flame front. Moreover, the burner has no scaling problem since all flow rates can be independent of the burner size, given the use of diffusion flames. Therefore, this flame synthesis setup has a potential to be scaled up for efficient growth over a large-area surface in continuous production. In cases where the fuel is used as both reagent and heat source, the method becomes further cost-effective and efficient.

This thesis primarily explores growing nanostructured carbon on various metal and non-metal substrates, such as copper, nickel, stainless steel and silicon wafers. No external pretreatment of the substrate is needed in this method. The key parameters, i.e., substrate material, flame temperature, flow profile, precursor delivery rate, synthesis time, hydrogen addition for producing graphene and CNTs in the flame are investigated. Also, using the same m-IDF setup in a single experimental run, the effect of switching the gas composition to allow for post-growth hydrogen annealing that can control the quality of graphene formed in the flame.

### 1.3 Research Objective

The production of CNTs has been reported using various flame aerosol processes. However, very limited results have been reported using flame synthesis to produce graphene. The growth of graphene may be more challenging compared with CNTs. CVD methods mainly use transition metals as growth substrates for graphene. Among them, Cu is reported to have a self-limiting growth mechanism for graphene while other transition metals like Co and Ni exhibit a segregation mechanism which requires precise control of the cooling rate to achieve high-quality graphene synthesis. The temperature and species gradient in most flames are not suitable for graphene growth, which needs a well-controlled uniform gas-phase condition. Also, the flow flux and pressure play important roles in graphene growth. All these factors have prevented flame techniques from producing mono- and bi-layer graphene in the past decade. The research in this thesis involves operating a



modified multi-element diffusion flame burner running in an inverse mode to produce nanocarbon, along with adjusting relevant parameters to optimize certain growth characteristics, in open atmosphere. The fundamental growth mechanisms are further investigated by probing profiles of temperature and chemical species in the flow field. Finally, applications for the produced graphene films are examined.

The objective of this thesis is to investigate into the growth fundamentals of graphene and CNTs (and possible metal-oxides) using a modified multi-element diffusion-flame burner. Various parameters, such as growth time, precursor flow rate, substrate material, and temperature, are studied, along with mapping of temperature and species profiles in the gas-phase. The optimal growth conditions for graphene and CNTs on different substrates are studied.

The research components of this thesis involve:

A. Modified Multi-Element Inverse-diffusion Flame Setup

This new flame configuration is based on multi-element inverse diffusion flames and modified with individual precursor delivery tubes staged above the burner surface. This new setup is designed for the synthesis of monolayer graphene and other nanostructured carbon materials.

B. Parametric Study of Graphene Synthesis in Open-atmosphere Flame

Few-layer graphene has been synthesized using flame synthesis in previous studies [4], [22]. However, mono- and bi-layer graphene were not produced. Therefore, the key

growth parameters of flame synthesis of graphene such as substrate temperature and materials, precursor and hydrogen flow rates, and growth time, are examined and optimized in this work. Raman spectroscopy and transmission electron microscopy (TEM) are employed as the main tools to characterize the quality of graphene samples.

#### C. Monolayer Graphene Synthesis

A goal of this research is to grow monolayer graphene using unconfined flame synthesis. Even though high-quality monolayer graphene films have been produced by CVD and mechanical cleavage methods, an efficient and open-environment gas-phase method is urgently needed to meet the increasing demands for graphene applications. The flame system described in this thesis running in the open atmosphere has the potential to grow monolayer graphene over large areas at fast processing times and low cost.

After optimization of the flame condition, bilayer graphene also can be produced. A post-growth hydrogen annealing process in-situ is employed to tailor bilayer graphene towards monolayer graphene. Monolayer graphene synthesized in the flame is readily transferred to other substrates, like silicon wafer or glass, for further study and applications.

#### D. Highly Defective Graphene Synthesis

The effect of the in-situ post-growth hydrogen annealing process on flame-synthesized graphene is investigated in this thesis. Graphene samples with different original conditions and substrate materials are examined. The same multi-element inverse-

diffusion flames perform the hydrogen annealing treatment sequentially by simply turning off the hydrocarbon precursor and maintaining the inverse hydrogen flames at the base of the burn. Raman spectroscopy is used ex-situ to evaluate the quality of graphene samples with and without hydrogen annealing treatment.

Hydrogen annealing exhibits strong etching effect on defected graphene samples. Therefore, such approach can be used to manufacture highly defective graphene films with tunable defects, which have applications in ion selective membranes and sensors. Highly-defective graphene samples are fabricated into graphene-based membranes for ion-selection tests.

#### E. CNT Synthesis on Metal and Non-Metal Substrates

CNT growth has been studied using various flame aerosol processes. Nevertheless, the progress of CNTs grown on non-metal substrates is limited. In this thesis, the chemical-solution-seeding technique widely-used in CVD is employed to grow CNTs directly on Si wafer. CNTs deposited on insulators are required for many electronic applications.

Carbon-metal oxide nanocomposites have received considerable research attention for their high performance in batteries and supercapacitors. The hybrid growth of CNTs and iron oxides on stainless steel substrates is explored in this thesis using multi-element inverse-diffusion flames. Additionally, the conditions for a transition from CNT growth to various phases of iron oxides growth are examined.

Scanning electron microscope is used to study the morphology of samples. X-ray photoelectron spectroscopy and X-ray diffraction are employed to study the phase of iron oxide nanocrystals. Raman spectroscopy is also used to study the phase of iron oxide and detect carbon nanostructures.

#### 1.4 Approach

The general approach used for the flame synthesis of nanostructured carbon materials consists of two main parts as depicted in Figure 1.2. The results from the ex-situ characterization help to direct the experiments. A number of parameters are investigated and optimized for nanostructured carbon growth. This approach consists of parametric study, and in-situ/ex-situ characterization provides the opportunity to understand the growth mechanisms of nanostructured carbon using flame synthesis.

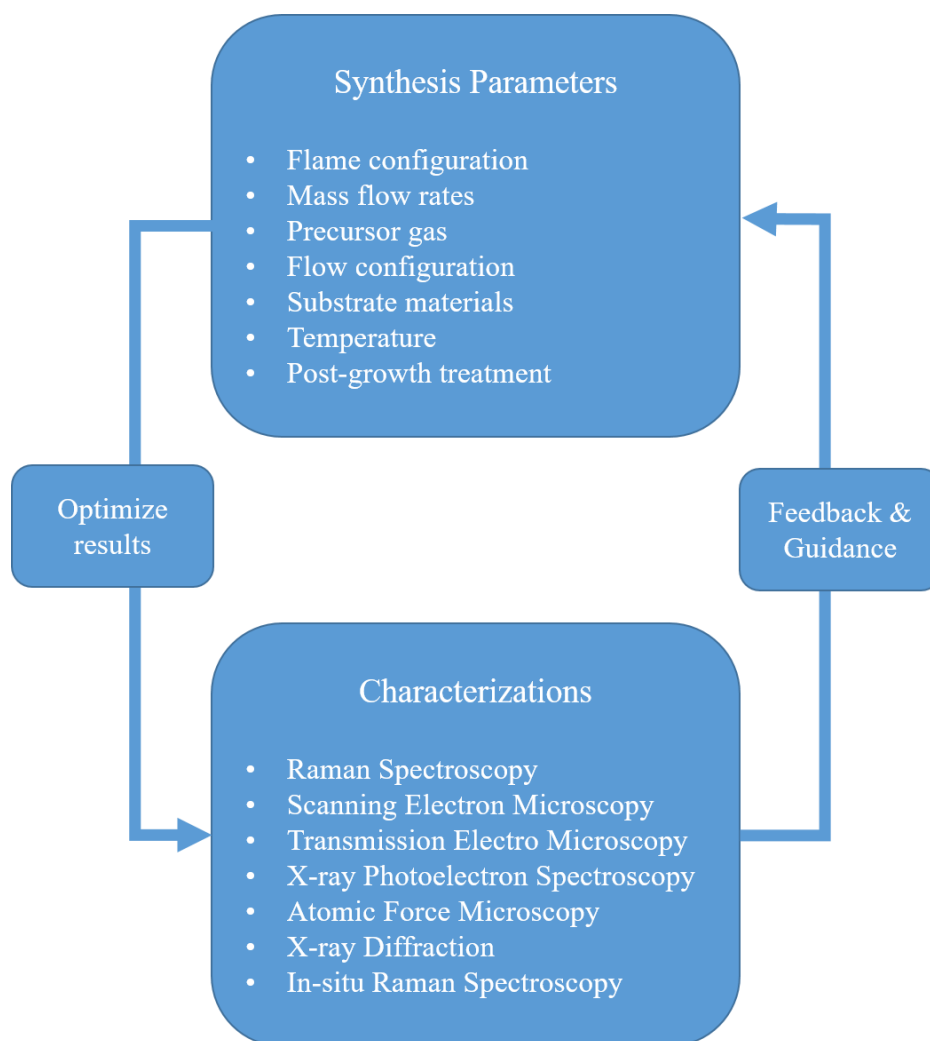


Figure 1.2 Scheme of general approach used in this study for flame synthesis of nanocarbon.

## 1.5 Outline of this dissertation

Chapter 2 presents a literature review on the background of nanostructured carbon materials, specifically graphene and carbon nanotubes, along with the flame synthesis method. Chapter 3 describes the general research tools including experimental setup and in-situ and ex-situ characterization techniques employed in this research. Chapter 4 is a

systematic study of graphene growth condition in flame synthesis. Parameters investigated in this chapter are substrate temperature, methane-to-hydrogen flow rate ratio, growth time, substrate material, hydrocarbon precursor, flow field profile, and transfer process. Chapter 5 describes the synthesis of monolayer graphene using a sequential hydrogen-fuel-only m-IDFs for annealing. Chapter 6 discusses the impact of hydrogen annealing on flame-synthesized graphene samples with different as-synthesized graphene qualities and substrate materials. Chapter 7 presents the transition growth from  $\alpha$ -Fe<sub>2</sub>O<sub>3</sub> nanoparticle films to  $\gamma$ -Fe<sub>2</sub>O<sub>3</sub> nanocrystals, in combination with CNTs, on stainless steel substrates, the hybrid growth of CNT-Fe<sub>2</sub>O<sub>3</sub> nanocomposites on stainless steel, and CNTs growth on Si wafers using a chemical-solution-seeding process.

## Chapter 2

### 2. Literature Review

#### 2.1 Introduction

Carbon materials have attracted considerable research attention for their extensive applications in past decades. Carbon forms a number of allotropes based on different arrangements of carbon atoms (Fig. 2.1). The best-known carbon materials are graphite and diamond. Because of the various types of carbon bonds, carbon allotropes share some similarities but can exhibit very different properties. Diamond is transparent in the visible and known as the hardest natural material, while graphite is opaque in the visible and is one of the softest substances. Carbon is the 15<sup>th</sup> most abundant element in the Earth's crust and one of the few elements known since antiquity. However, new carbon allotropes and structures have been discovered in past decades along with the development of science over time (Table 2.1).

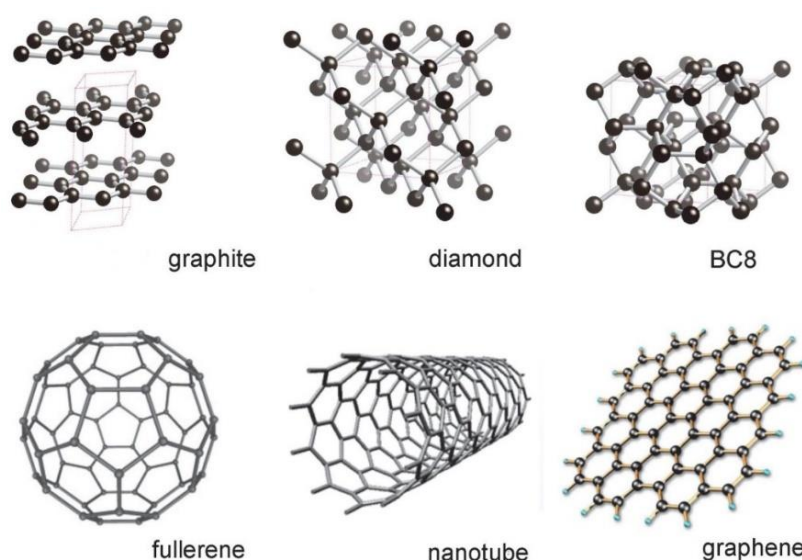


Figure 2.1 Structures of selected carbon allotropes (reproduced from [5]).

Table 2.1 History of carbon materials (reproduced from [1])

First “Lead” pencils	1600’s
Discovery of carbon composition of diamond	1797
First carbon electrode for electric arc	1800
Graphite recognized as a carbon polymorph	1855
First carbon filament	1879
Chemical vapor deposition (CVD) of carbon patented	1880
Production of first molded graphite (Acheson process)	1896
Carbon dating with $^{14}\text{C}$ isotope	1946
Industrial production of pyrolytic graphite	1950’s
Industrial production of carbon fibers from rayon	1950’s
Development and production of vitreous carbon	1960’s
Development of carbon fibers	1960’s
Discovery of low-pressure diamond synthesis	1970’s
Production of synthetic diamond suitable for gem trade	1985
Development of diamond-like carbon (DLC)	1980’s
Discovery of the fullerene molecules	Late 1980’s
Discovery of carbon nanotubes (CNTs)	1991
Industrial production of CVD diamond	1992
Discovery of graphene	2004
Sorting of CNTs by size and properties	2006
Development of CVD graphene	Late 2000’s
CNT transistors outperform silicon for the first time	2016



Nanostructured carbon can be classified as zero-, one-, two-, and three-dimensional materials, namely fullerene, carbon nanotube, graphene, and nanodiamond, respectively. Moreover, carbon materials can be functionalized for new physical or chemical properties by assembling or architecturing with functional parts. For example, graphene can be doped with hetero-atoms or chemically modified to be semiconductors. The broad applications of nanostructured carbon materials require a fundamental understanding of the synthesis process to design the nanostructure. Therefore, this chapter will review the fundamentals, current synthesis methods, and applications of nanostructured carbon, specifically focusing on graphene and CNTs.

## 2.2 Graphene Background

### 2.2.1 Graphene fundamentals

Graphene, a new paradigm in materials science and condensed matter physics, has drawn extensive research interest since Kostya Novoselov, Andre Geim, et al. [36] proved single-atom-thick graphene to exist in the free state in 2004. This atomically thin carbon film with a “two-dimensional” honeycomb array of  $sp^2$ -bonded carbon atoms is the building material for other allotropes of carbon (Fig. 2.2). Graphene sheets can stack to form bulk graphite with van der Waals forces between individual layers. The fullerene, discovered in 1985 [37], can be viewed as a “zero-dimensional” carbon ball rolled from graphene sheets. Graphene also can be rolled into “one-dimensional” carbon nanotubes. Since graphene received enormous attention, some other layered compounds including

hexagonal boron nitride (h-BN), dichalcogenides (e.g.,  $\text{MoS}_2$ ,  $\text{WS}_2$ ), and artificially stacked atomic layers (heterostructures) have been extensively studied [38].

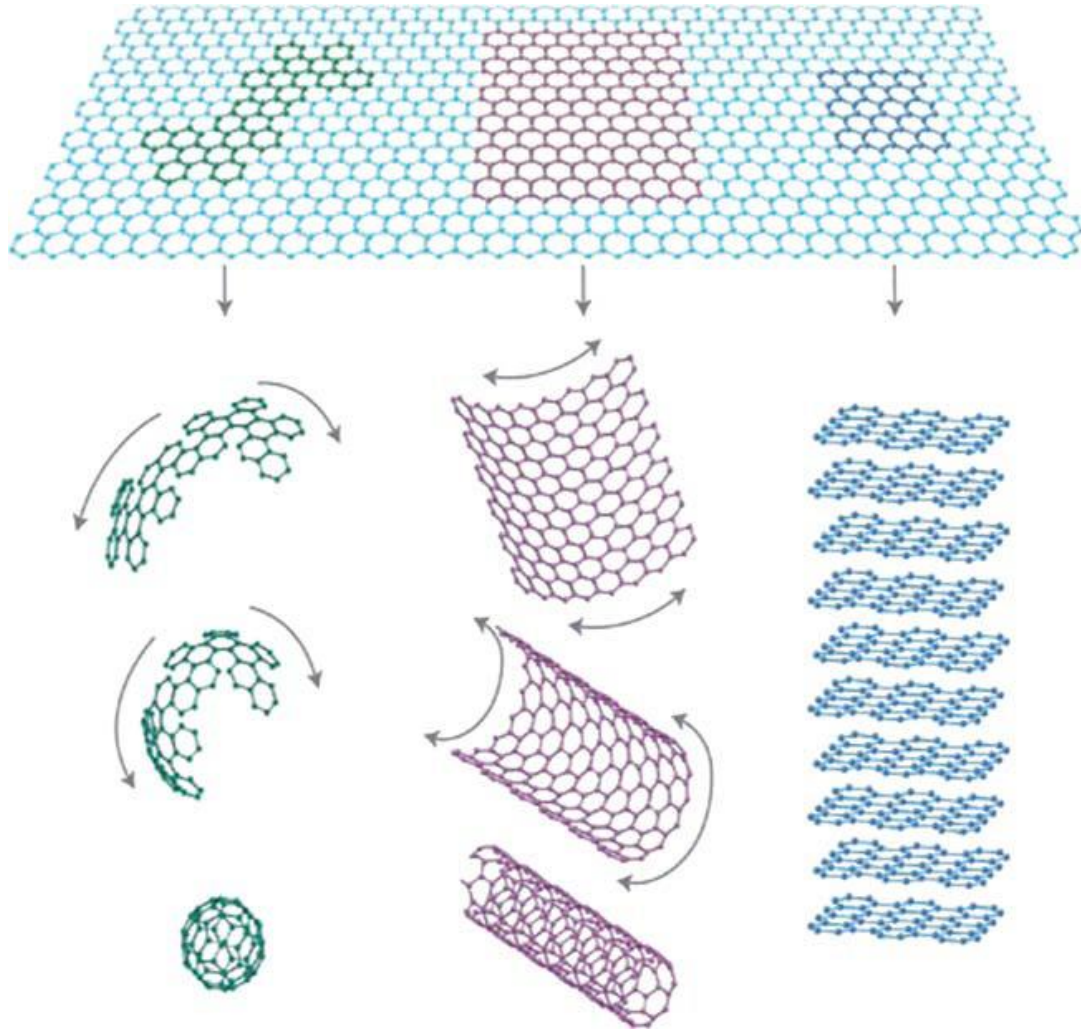


Figure 2.2 Graphene is a 2D building material for carbon materials of all other dimensionalities. It can be wrapped up into 0D buckyballs, rolled into 1D nanotubes or stacked into 3D graphite (reproduced with caption from [6]).

### *2.2.1.1 Electrical properties*

The micromechanical cleavage technique for obtaining graphene from graphite using scotch tape enabled the direct observation of the quantum mechanically enhanced transport phenomena when electrons are confined in two-dimensional materials [39]. The observation of quantum Hall effect in graphene provided direct evidence of graphene's theoretically predicted massless relativistic particles (Dirac fermions) [40]. Graphene has a unique conical band structure where cones are located at two inequivalent Brillouin zone corners. Since its conduction and valence bands meet at the Dirac points, graphene is a zero-band-gap semiconductor (see Fig. 2.3A, B). However, by applying an electric field on the bilayer graphene, a widely tunable bandgap is observed (see Fig. 2.3C) [7], [41]. The intrinsic mobility of graphene is at  $\sim 200,000 \text{ cm}^2\text{V}^{-1}\text{s}^{-1}$  at a carrier density of  $10^{12} \text{ cm}^{-2}$ , while the extrinsic mobility of graphene on  $\text{SiO}_2$  is  $\sim 40,000 \text{ cm}^2\text{V}^{-1}\text{s}^{-1}$  at room temperature, comparable to the best field-effect transistors (FETs) [39], [42], [43]. The extrinsic limit to the mobility of graphene on  $\text{SiO}_2$  is mainly due to the scattering of electrons by optical phonons of the substrate [42]. The exceptional mobility property of graphene allows for room-temperature electronic devices based on quantum transport.

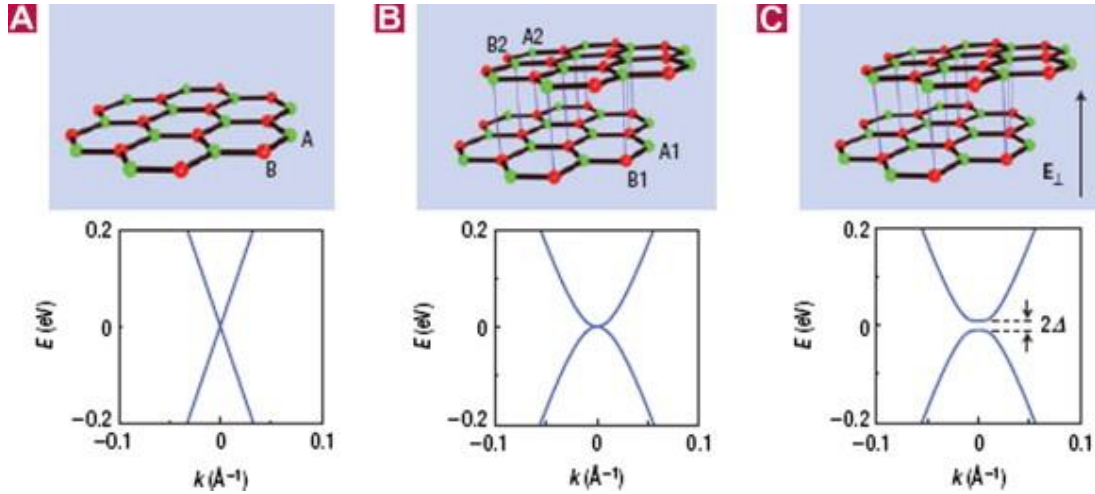


Figure 2.3 Bandgap in graphene. Schematic diagrams of the lattice structure of (A) monolayer and (B) bilayer graphene. The green and red colored lattice sites indicate the A (A1/A2) and B (B1/B2) atoms of monolayer (bilayer) graphene, respectively. The diagrams represent the calculated energy dispersion relations in the low-energy regime and show that monolayer and bilayer graphene are zero-gap semiconductors. (C) When an electric field ( $E$ ) is applied perpendicular to the bilayer, a band gap is opened up in bilayer graphene, whose size ( $2\Delta$ ) is tunable by the electric field. (reproduced with caption from [7])

### 2.2.1.2 Thermal properties

For graphene-based electronic devices, thermal conductivity is a key factor that determines the performance. Thermal transport in graphene has attracted much attention because of the potential thermal management applications. The superior room-temperature thermal conductivity of a suspended single-layer graphene was reported with values in the range from  $\sim 4,840$  to  $5,300$  W/mK in 2008 [44]. This value is more than double of the values found in diamond and pyrolytic graphite [45]. However, later studies reported much lower values in the range from  $\sim 1800$  to  $2500$  W/mK near room temperature [8], [45]. The big difference in measured values may be because the thermal conductivity of

graphene is a function of temperature and length [46], and can be affected by the sample preparation processes and experimental conditions. Raman scattering spectroscopy setup (see Fig. 2.4) has been employed to measure the thermal conductivity of suspended pristine graphene. The temperature change is monitored by measuring the shift in the graphene Raman 2D band, and thermal conductivity can be deduced from heat diffusion equations [8].

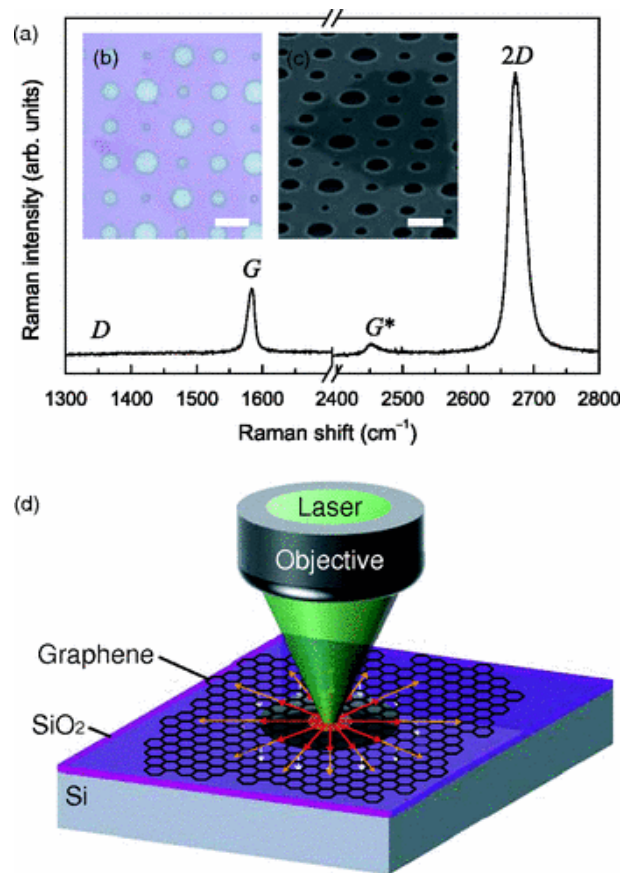


Figure 2.4 (a) Raman spectrum of suspended graphene. (b) Optical microscope and (c) scanning electron microscopy images of suspended graphene sample. The scale bars are 10  $\mu\text{m}$ . (d) Schematic diagram of the experimental setup for thermal conductivity measurement of graphene using Raman spectroscopy (reproduced with caption from [8]).

### 2.2.1.3 Mechanical properties

Since carbon atoms in a graphene layer are connected by  $\sigma$ -bonds, the strongest type of covalent chemical bonds, graphene is reported as the strongest material ever measured with Young's modulus of 1 TPa and fracture strength of 130 GPa [9]. The elastic properties and mechanical strength of free-standing graphene have been measured by nanoindentation in an atomic force microscope (see Fig. 2.5).

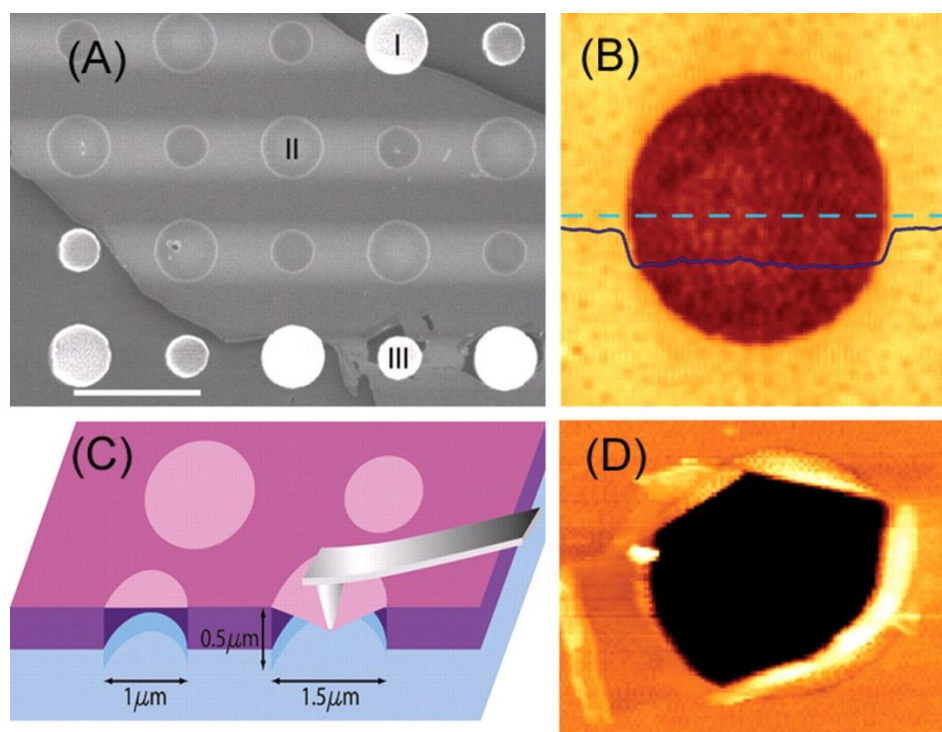


Figure 2.5 (A) Scanning electron micrograph of a large graphene flake spanning an array of circular holes 1  $\mu\text{m}$  and 1.5  $\mu\text{m}$  in diameter. (B) Noncontact mode AFM image of one membrane. The solid blue line is a height profile along the dashed line. The step height at the edge of the membrane is about 2.5 nm. (C) Schematic of nanoindentation on suspended graphene membrane. (D) AFM image of a fractured membrane. (reproduced with caption from [9]).



### 2.2.1.4 Optical properties

Graphene exhibits a unique optical property with a frequency-independent absorbance having a magnitude given by  $\pi\alpha \approx 2.3\%$  ( $\alpha$  denotes the fine structure constant) in the infrared-to-visible spectral range [47]. The absorbance of suspended graphene crystals agrees with the calculated absorption of light by ideal two-dimensional Dirac fermions (see Fig. 2.6). Theoretical prediction and measurements yield monolayer graphene's opacity of  $2.3 \pm 0.1\%$  and reflectance  $< 0.1\%$ . Therefore, the transmittance of white light can be used as an indicator for the number of graphene layers.

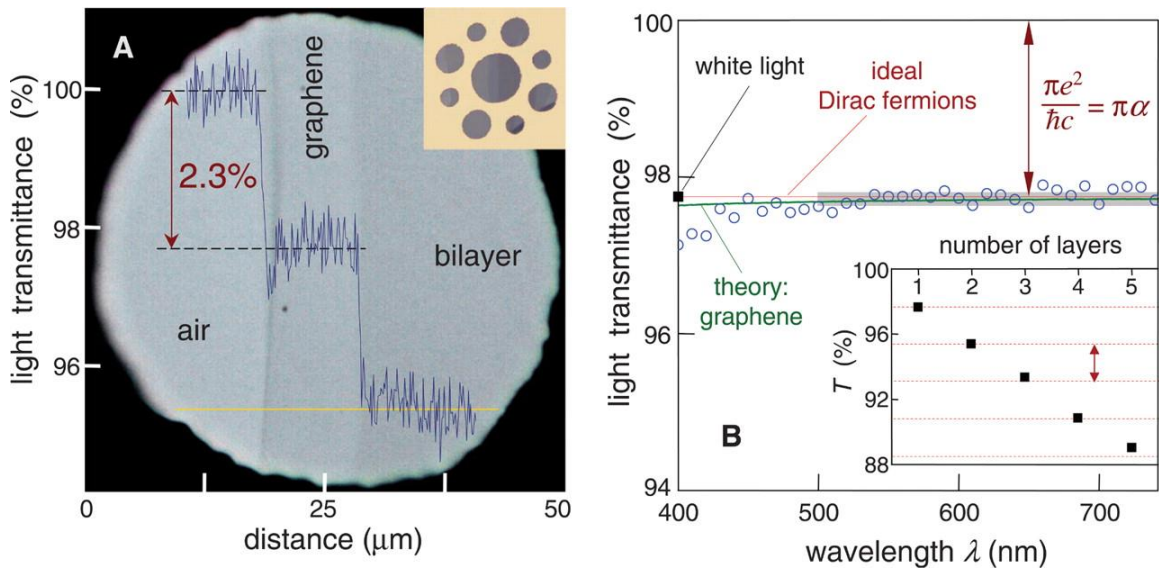


Figure 2.6 Looking through one-atom-thick crystals. (A) Photograph of a 50-μm aperture partially covered by graphene and its bilayer. The line scan profile shows the intensity of transmitted white light along the yellow line. (B) Transmittance spectrum of single-layer graphene (open circles). Slightly lower transmittance for  $\lambda < 500$  nm is probably due to hydrocarbon contamination. The red line is transmittance  $T = (1+0.5\pi\alpha)$  expected for two-dimensional Dirac fermions, whereas the green curve takes into account a nonlinearity and triangular warping of graphene's electronic spectrum. The gray area indicates the standard error of our measurements. (Inset) The transmittance of white light as a function of the number of graphene layers. (reproduced with caption from [10])

### 2.2.2 Graphene synthesis

A number of synthesis methods have been studied since graphene was first isolated from highly ordered pyrolytic graphite (HOPG). Current production methods of graphene can be categorized into the top-down approach and bottom-up approach (see Fig. 2.7). Top-down methods separate graphene sheets from bulk graphite via mechanical or liquid-phase exfoliation. The bottom-up approach is a vapor-phase synthesis of graphene films on catalytic substrates, such as copper, nickel, silicon carbide, etc. Bottom-up methods, including chemical vapor deposition (CVD), epitaxial growth, and flame synthesis, are expected to be more feasible for continuous mass production of large-area graphene for various electronic applications.

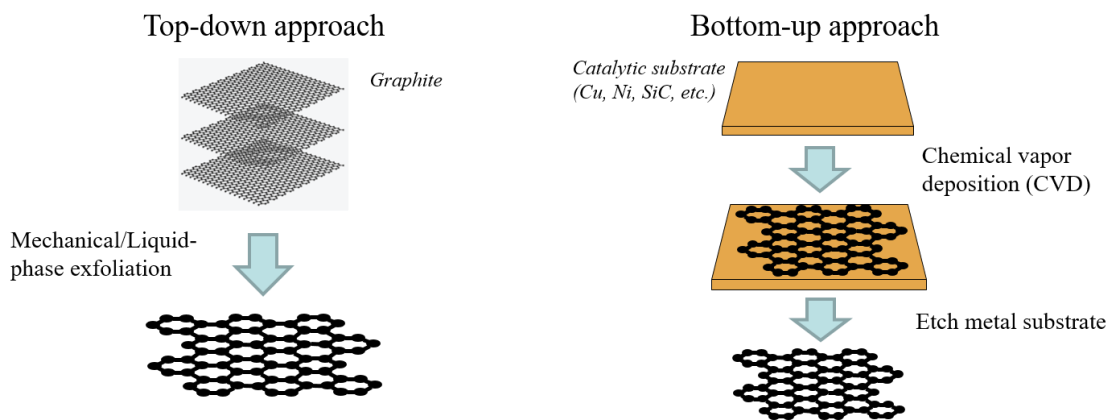


Figure 2.7 Schematic of two main approaches used in graphene synthesis: Top-down approach and Bottom-up approach.



### 2.2.2.1 Micromechanical cleavage

Micromechanical cleavage is the method used to first isolate graphene with lowest defects and best electrical properties in 2004 [36]. The layered structure of graphite and weak  $\pi$ -bond between layers enable the production of graphene by peeling graphite. Scotch tape is the simple tool used for pulling graphene sheets away from HOPG (see Fig.2.8). After peeling is performed multiple times, monolayer and few-layer graphene can be made. Although the physical properties of mechanical-exfoliated graphene sheets are excellent, this method is not feasible for large-scale continuous production of uniform graphene films.

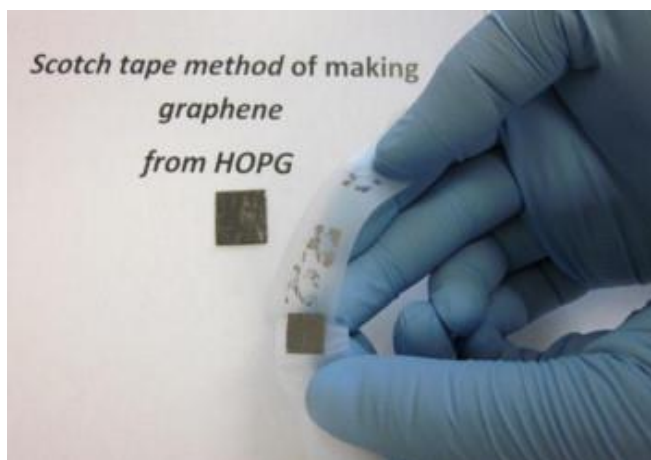


Figure 2.8 Mechanical cleavage of graphene using scotch tape from HOPG. (reproduced with caption from [11]).

### 2.2.2.2 Liquid-phase exfoliation

Graphene oxide sheets can be isolated through a liquid-phase oxidation process (see Fig.2.9), where strong aqueous oxidizing agents such as sulfuric acid, nitric acid, sodium nitrate, or potassium permanganate are commonly used [48]. Graphene oxide is further

reduced to graphene following chemical reduction or thermal annealing. However, the inevitable structural defects introduced by the invasive chemical oxidation are virtually impossible to restore [11]. Chemical exfoliation method allows mass production of graphene at low cost, but the reduced graphene oxide does not exhibit the same properties as pristine graphene.

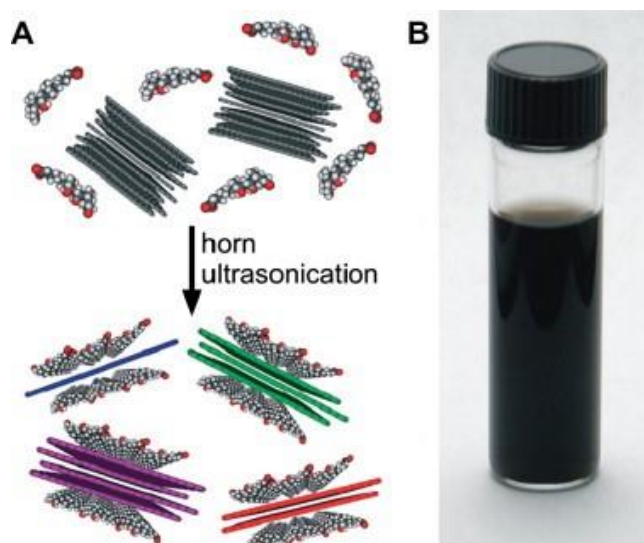


Figure 2.9 (A) Schematic illustration of the graphene chemical exfoliation process. (B) Photograph of graphene dispersion in solution (reproduced with caption from [11])

Non-chemical exfoliation of graphite has been reported using organic solvents such as N-methyl-pyrrolidone (NMP) [49]. In general, commercial graphite powder is first ultrasonicated in NMP solution and followed by a mild centrifugation for removing aggregates. The similar surface energy of NMP and graphene enable such approach. High-quality monolayer graphene can be produced at a significant yield via such liquid-phase method. However, the high cost of the solvent hinders this process from commercial use.

High-shear mixing is another liquid-exfoliation process, where shear mixing substitutes sonication for graphene production (see Fig. 2.10). Effective exfoliation of graphite occurs once the local shear rate exceeds  $10^4 \text{ s}^{-1}$  in the solvent NMP, aqueous surfactant solutions such as sodium cholate, or polymers such as polyvinylalcohol [12]. Such approach can produce low-defect graphene dispersion in various solutions at a high production rate using a high-shear mixer, a scalable and widely accessible equipment.

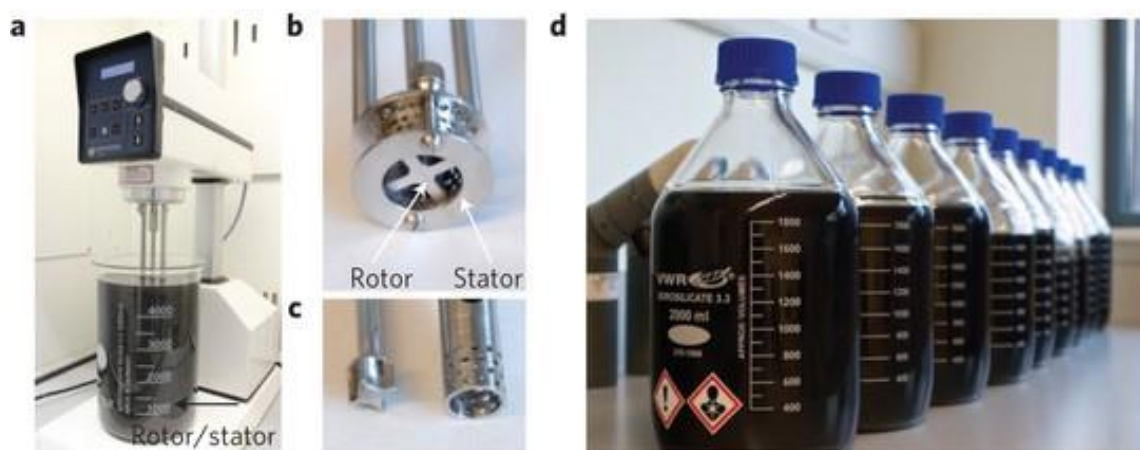


Figure 2.10 a, A commercial model high-shear mixer with mixing head (b) and rotor and stator (c). d, Graphene-NMP dispersions produced by shear exfoliation (reproduced with caption from [12]).

### 2.2.2.3 Epitaxial growth on silicon carbide (SiC)

Even though liquid-phase methods have the potential for large-scale manufacturing of graphene, they are not very feasible for the semiconductor industry, where high-quality pristine graphene films on insulators are required before processing devices. Epitaxial growth of graphene on SiC has attracted much research attention because of the advantage

of direct graphene growth on an insulating surface, ready for many electronic applications. Silicon atoms sublime from the SiC surface, and carbon atoms rearrange into graphene structures when the substrate is annealed at a temperature around 1200°C under ultrahigh vacuum (UHV) [50]. The formation of few-layer graphene typically takes a few minutes. The impacts on graphene quality and morphology from a number of growth parameters such as annealing time, temperature, pressure, and different SiC polar faces (i.e., Si face or C-face) have been studied [11]. Atmospheric-pressure annealing on 6H-SiC(0001) substrate leads to better graphene quality and grain size than annealing in vacuum [51]. Graphene film on SiC with a nominal thickness of 1.2 monolayers (monolayer film with the presence of bilayer) is formed in argon (p=900 mbar, T=1650 °C) via such approach. However, the expensive SiC wafer is a key disadvantage preventing the epitaxial growth method from commercial use. Moreover, the difficulty in transferring graphene from SiC substrate to other substrates limits the application of such method.

#### *2.2.2.4 Chemical vapor deposition (CVD)*

CVD, a well-established method in the semiconductor industry for producing thin films, is considered as a viable method for commercial production of high-quality graphene. Graphene growth on various transition metal substrates, including iridium [52], nickel [53], and copper [54], [55] using CVD has been reported. Carbon solubility in transition metals plays a key role in growth quality of graphene.

For transition metals with moderately-high carbon solubility such as iron, cobalt and nickel, the growth mechanism of graphene is described as a segregation process where extra layers of graphene can precipitate out upon cooling the system [56], [57]. At the growth temperature, carbon atoms diffuse into the metal thin film forming intermediate compounds like  $\text{Ni}_3\text{C}$ , which lowers the energy pathway for graphene growth. The subsequent rapid quenching of the metal substrate causes the incorporated carbon atoms to precipitate out and form graphene layers on the metal surface [11]. When using nickel substrate, it is common to get few-layer graphene, but monolayer graphene can be produced on thin nickel film when the cooling rate is well-controlled [27].

The low carbon solubility and filled 3d shells make copper an ideal metal for monolayer graphene growth. Unlike nickel or cobalt, graphene growth on copper is mainly a surface reaction mechanism. In a typical CVD process on copper, carbon species (e.g. methane) first diffuse through the boundary layer (steady-state boundary layer flow is assumed) and get adsorbed on the surface, then decompose to form active carbon species, and diffuse on the surface of the catalyst (e.g. copper) leading to graphene growth (see Fig. 2.11).

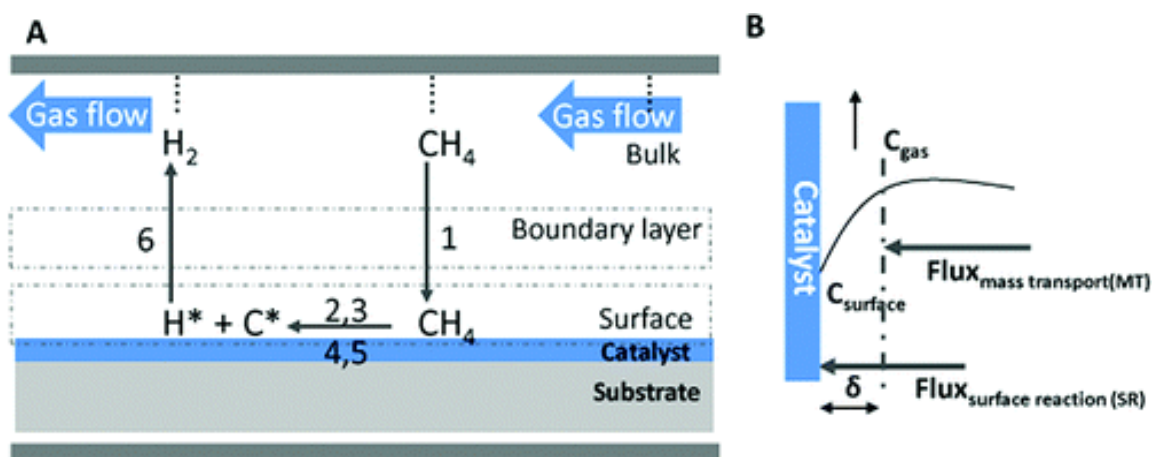


Figure 2.11 (A) Processes involved in graphene synthesis using low carbon solid solubility catalysts (Cu) in a CVD process. (B) Mass transport and surface reaction fluxes under steady state conditions (reproduced with caption from [13]).

Large-domain (up to 0.5 mm) single crystal graphene with room-temperature mobility greater than  $4,000 \text{ cm}^2 \text{V}^{-1} \text{s}^{-1}$  is grown on copper by low-pressure chemical vapor deposition (LPCVD) at  $1035^\circ \text{C}$  [58]. Additionally, a roll-to-roll production of 30-inch graphene films via CVD has been reported [14] (see Fig. 2.12). The films obtained from this process have sheet resistances as low as  $\sim 125 \text{ } \Omega/\text{square}$  and 97.4% optical transmittance, indicating potential application as transparent electrodes for touch-screen panel devices. However, CVD typically uses high operating temperatures ( $\sim 1000^\circ \text{C}$ ) and vacuum chambers, which increase the cost of such technique.

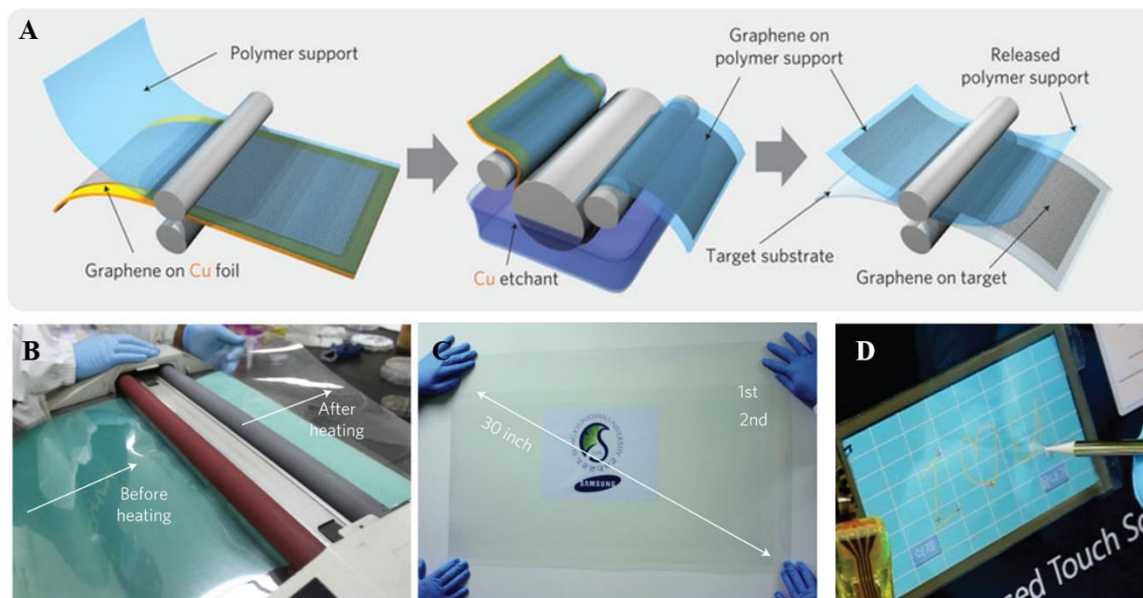


Figure 2.12 (A) Schematic of roll-to-roll production of graphene films grown on a copper foil. The process includes adhesion of polymer supports, copper etching (rinsing) and dry transfer-printing on a target substrate. (B) Photographs of the roll-to-roll process. (C) A 30-inch graphene film transferred on a 35-inch PET sheet. (D) A touch screen made of graphene/PET film. (reproduced with caption from [14]).

Attributed to the low solubility of carbon in copper, graphene growth on copper is expected to be self-limited to a single monolayer. This self-limiting mechanism has been validated in LPCVD. However, recent studies have demonstrated that few-layer graphene can form on copper using atmospheric-pressure chemical vapor deposition (APCVD) [59]. Even though the thermodynamics of graphene growing on copper at a particular temperature is the same for low-pressure and atmospheric-pressure CVD, the kinetics (cooling rate, the pressure of reaction chamber, etc.) of the CVD process has great impact on the growth rate and quality of graphene [13]. Copper substrate is subjected to a pre-treatment in a hydrogen atmosphere at high temperature to eliminate any oxide layer

on the metal surface and enlarge its grain size [60]. This step is critical for large-area graphene growth.

A direct observation of graphene growth on copper during a LPCVD process has been achieved by using in-situ scanning electron microscopy (SEM) [15]. The nucleation and growth of graphene on copper at 1000 °C is recorded (see Fig. 2.13). Graphene starts to nucleate out and grow when supersaturation is reached. The nucleation rate drops significantly after the initial stage because of a shortage of carbon building blocks. The growth speed drops rapidly as the growth fronts of adjacent sheets approach each other.



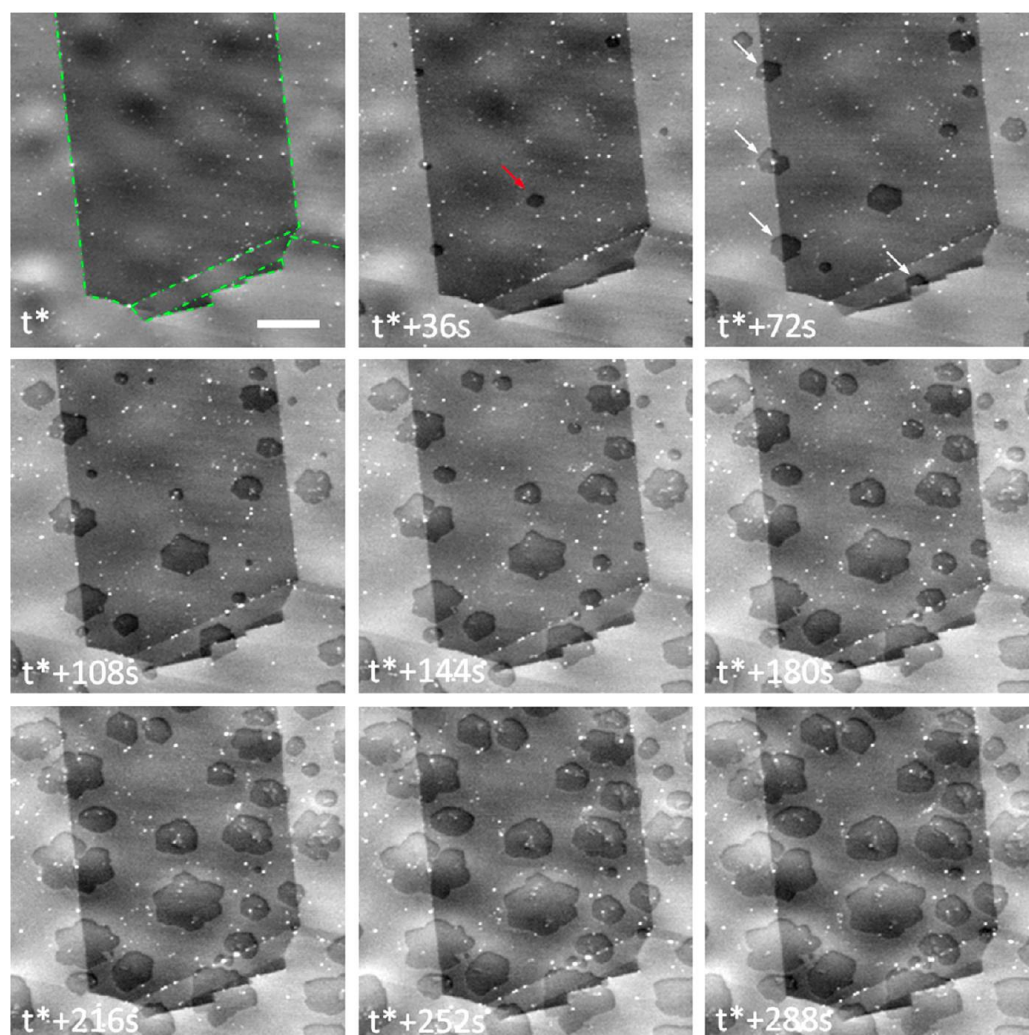


Figure 2.13 In situ SEM images recorded at 1000 °C during LPCVD growth showing the nucleation and growth of carbon sheets (characterized by darker contrast). White arrows highlight nucleation events at grain boundaries.  $t^*$  corresponds to the induction period from  $C_2H_4$  dosing until the first nucleation events can be detected. Growing graphene sheets are characterized by a dark contrast. The smooth contrast of the copper surface is due to a sublimation-induced surface buckling. Grain boundaries in the copper foil are highlighted by green dotted lines in the top left image. Differences in contrast for different grains are due to electron channeling. The scale bar measures 5  $\mu m$  (reproduced with caption from [15]).

Graphene deposited on copper can be transferred onto other substrates for characterization or fabrication of devices. The common transfer process of graphene using wet-chemistry method is shown in Fig. 2.14. As-grown graphene on Cu is first spin-coated with a poly(methyl methacrylate) (PMMA) protective coating. After the PMMA coating is cured, the Cu substrate is etched away by using iron nitride or iron chloride aqueous solution. The PMMA/Graphene stack is washed in deionized (DI) water and transferred to the target substrate. The last step is to remove the PMMA coating with acetone. However, the traditional process can cause the graphene to form cracks because of intrinsic mechanical properties of monolayer graphene. Before removing the initial PMMA layer, redepositing another layer of PMMA can reduce the cracks of graphene after the transfer process [16]. Transfer to an insulating surface (e.g., silicon or quartz) is required to measure optical and electronic properties of synthesized graphene. Silicon wafer is a common support material for graphene-based semiconductor applications.

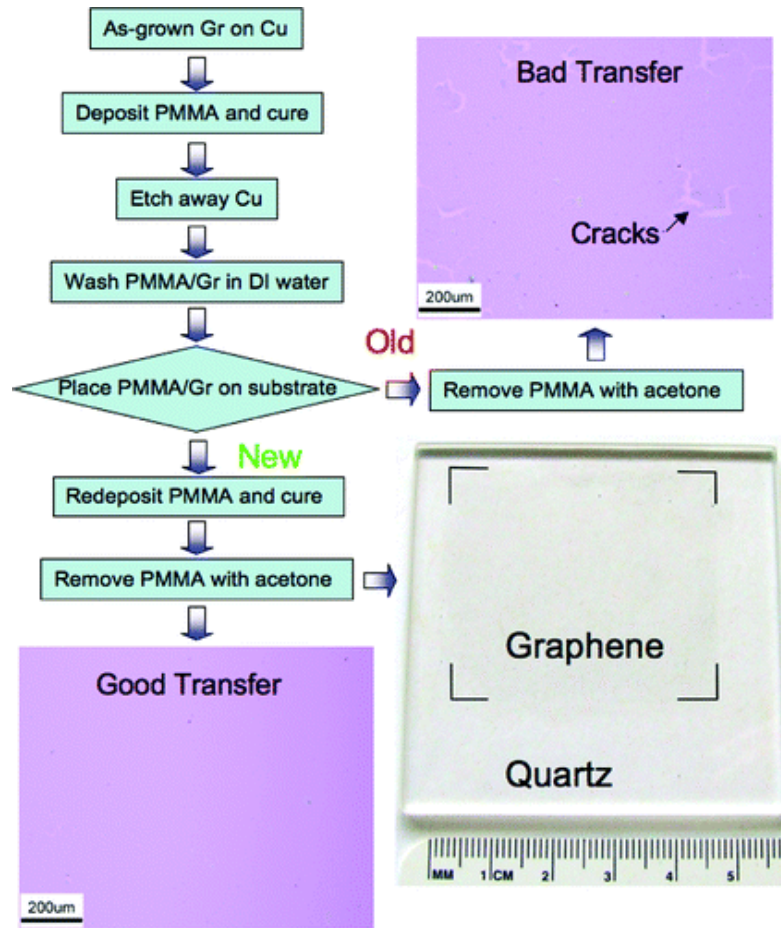


Figure 2.14 Processes for transfer of graphene films (“Gr” = graphene). The top-right and bottom-left insets are the optical micrographs of graphene transferred on SiO<sub>2</sub>/Si wafers (285 nm thick SiO<sub>2</sub> layer) with “bad” and “good” transfer, respectively. The bottom-right is a photograph of a 4.5 × 4.5 cm<sup>2</sup> graphene on a quartz substrate (reproduced with caption from [16]).

#### 2.2.2.5 Plasma synthesis

Plasma-enhanced chemical vapor deposition (PECVD) is utilized to grow graphene at a lower substrate temperature (300 – 900 °C) with faster processing time than that for thermal CVD [61]. Both mono- and few-layer graphene have been deposited on various substrates using gas mixtures of 5 – 100% CH<sub>4</sub> in H<sub>2</sub> at 900 W power and 680 °C substrate

temperature, using a radio frequency PECVD system [11]. The core part of the PECVD system is the plasma generator, which can be categorized into three types: microwave plasma (commonly 2.45 GHz), radio frequency plasma (commonly 13.56 MHz), and direct current plasma. In addition, substrate-free synthesis of graphene has been reported by Albert Dato et al. [62] using a microwave plasma reactor. However, aerosol-type graphene growth is still controversial. Generally, the quality of graphene produced in PECVD is lower than thermal CVD.

### 2.2.3 Graphene applications

The exceptional physical and chemical properties of graphene enable a broad range of applications in fields such as biomedical devices, electronics, light processing, energy, sensors, environmental applications, etc. Many graphene industrial manufacturers like Applied Graphene Materials have sprung up in the last decade. One of the first graphene-based commercial products, a flexible graphene touch-screen for smartphone unveiled in 2016.

#### *2.2.3.1 Electronics*

High carrier mobility makes graphene one of the most promising materials for the semiconductor industry in the post-silicon era. However, the main hurdle for graphene application in transistors is the absence of an energy gap separating the valence and conduction bands of graphene. A widely tunable bandgap observed in bilayer graphene

enables its application in field-effect transistors (FETs) [63], [64]. Besides bilayer graphene, hetero-atom doping is another promising approach to tailoring the electronic properties of graphene for semiconductor applications. Both n- and p-type doped graphene have been achieved by substitutional doping of nitrogen (N) and boron (B) atoms, respectively, in the graphene structure [65], [66]. N- and B-doped graphene can be directly synthesized using vapor precursor like  $\text{NH}_3$  and  $\text{B}_2\text{H}_6$  in gas-phase synthesis processes. In addition, chemical modification of graphene by adsorbing atoms (e.g., Bi, Sb, Au, etc.) and/or molecules (e.g.,  $\text{N}_2\text{O}_4$ , AuPt,  $\text{Au}_3\text{Pt}_3$ , etc.) on the graphene surface can create n- and p-doping [67]. A group of researchers from IBM reported a wafer-scale graphene integrated circuit operating as a broadband radio-frequency mixer at frequencies up to 10 GHz in 2011 [68].

High electrical conductivity and optical transparency make graphene a candidate for transparent conducting electrodes in solar cells [35] and display screens [14]. Moreover, graphene's extraordinary mechanical property enables the application of graphene-based flexible touch screens. Stretchable and bendable transparent electrodes have rapidly increasing market demand for touch screens for next-generation smartphones and wearable devices, where graphene is considered as a viable solution. The first prototype graphene-based flexible display was unveiled in 2014 by a UK group from the University of Cambridge and Plastic Logic. Other electronic applications of graphene include quantum dots, organic light emitting diodes (OLEDs), and Hall Effect sensors.

### 2.2.3.2 Energy

Graphene has received great research attention for its application in energy devices because of its exceptional electrical and chemical properties. Next generation rechargeable batteries and supercapacitors are two main directions being pursued in the rising demand for electric vehicles and energy storage, where graphene can play important roles.

Graphene is considered as a light, flexible, and affordable building material for future batteries. Lithium-sulfur batteries using highly crumpled nitrogen-doped porous graphene as both sulfur host and interlayer material can achieve a high capacity of 1000 mAh/g, with exceptional cycle stability [69]. At the end of 2016, Huawei announced the world's first long-lifespan graphene-based Li-ion battery that can retain over 70% battery's capacity after being recharged 2000 times at a temperature of 60 °C (roughly 10 °C higher than the current upper limit).

Unlike batteries, supercapacitors can instantaneously provide higher power density, which is required for many energy storage applications. A graphene-based supercapacitor device using graphene/MnO<sub>2</sub> and ACN as electrodes can retain ~97% specific capacitance (max. 113.5 F g<sup>-1</sup>) after 1000 cycles with a measured energy density of 51.1 Wh kg<sup>-1</sup> [70]. Well-dispersed MnO<sub>2</sub> nanoparticles are deposited on the surface of graphene using microwave irradiation. Compared with pure graphene and MnO<sub>2</sub>, graphene/MnO<sub>2</sub> exhibits reduced diffusion length of electrolyte ions during the charge/discharge process, improved electrochemical utilization of MnO<sub>2</sub>, and fast electron transport through the graphene base.

### *2.2.3.3 Membranes*

Significant progress has been made in the fabrication, transport mechanism and application of graphene-based membranes in the past few years. A pristine monolayer graphene is a one-atom-thick impermeable barrier to all the atoms and molecules under ambient environment because of the dense electron cloud within the graphene lattice [71]. Graphene sheets with nano-scale pores, called nanoporous graphene (NPG), is a promising material for next-generation ultrafiltration and separation membranes. The history of graphene oxide (GO) membrane application can be traced back to the 1960s [17]. Graphene and its derivatives including NPG and GO have great potential in applications such as filtration, water desalination, energy storage and generation, separation, and ion selective mass transport. (see Fig. 2.15).

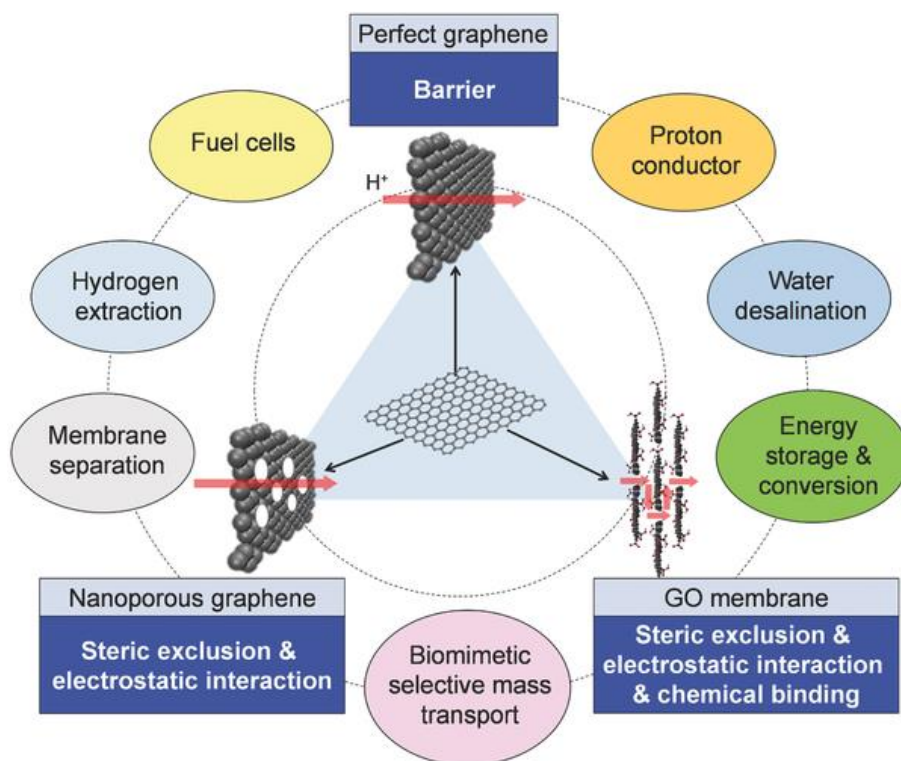


Figure 2.15 Schematic diagram illustrating the structure of graphene, NG and GO membrane, the mechanism for selective mass transmembrane transport and possible uses (reproduced with caption from [17])

Water desalination membrane using single-layer NPG has achieved a salt rejection rate of nearly 100% and rapid water transport [29]. Nano-scale pores in a graphene sheet are created by exposing pristine CVD graphene in an oxygen plasma for a few seconds. Aberration-corrected STEM is employed to characterize the morphology of the post-etched NPG, where 0.5-1 nm pores with a pore density on the order of 1 pore/100 nm<sup>2</sup> are observed. NPG membranes with tunable subnanometer pores exhibit selective ionic transport, which is an ideal candidate for nanofiltration [72]. Gas separation is another important application of NPG. The separation of hydrogen and nitrogen gases by controlling the



pore size and shape of NPG have been reported [73]. DNA sequencing is a rapidly developing area attracting considerable research attention. Many different approaches using graphene-based nanodevices involving DNA passing through graphene nanopores (see Fig. 2.16a, c) and nanogaps (see Fig. 2.16b), along with the physisorption of DNA on graphene (see Fig. 2.16d), have been reported [18].

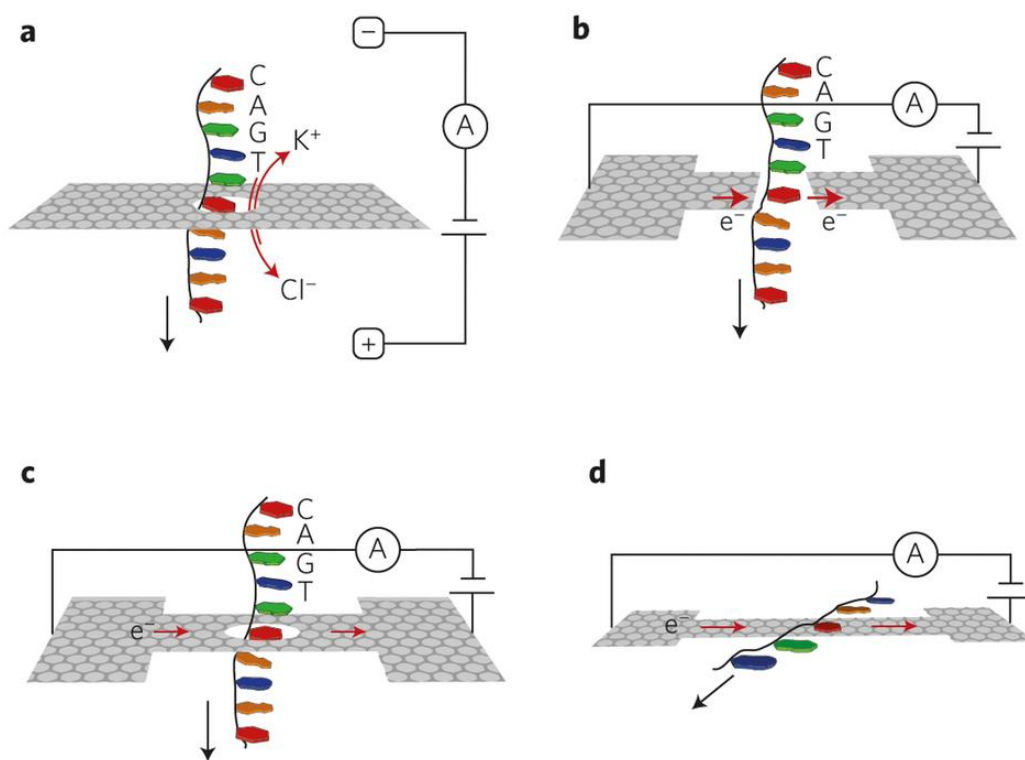


Figure 2.16 a, Detection of changes in the ionic current through a nanopore in a graphene membrane due to the passage of a DNA molecule. b, Modulations of a tunnelling current through a nanogap between two graphene electrodes due to the presence of a DNA molecule. c, Variations in the in-plane current through a graphene nanoribbon due to traversal of a DNA molecule. d, Changes in a graphene current due to the physisorption of DNA bases onto the graphene (reproduced with caption from [18])

## 2.3 Carbon Nanotube Background

### 2.3.1 Carbon Nanotube Fundamentals

Carbon filaments in the tubular form were first observed using electron microscopes in the 1950s[74]. A Japanese scientist, Sumio Iijima from NEC first described carbon nanotubes (CNTs) in 1991 [75]. His discovery soon initiated a flurry of excitement and inspired extensive research in the fundamentals and applications of CNTs. CNTs can be viewed as sheets of graphene rolled into tubular forms. Therefore, a single-wall nanotube (SWNT) consists of a single rolled sheet of graphene, while a multi-wall nanotube (MWNT) consists of multiple rolled sheets (concentric tubes) of graphene [20]. SWNTs normally have a diameter close to 1 nanometer while MWNTs can have a wide range of diameters from a few nanometers to hundreds of nanometers. The length of CNTs can be millions of times longer than the diameter. The spacing between each rolled layer of MWNT is 0.34nm, same as the spacing between graphene layers. Due to the unique structure with a significantly large aspect ratio (length-to-diameter ratio), CNTs are considered one-dimensional nanomaterials.

#### *2.3.1.1 CNT properties*

CNTs exhibit outstanding thermal conductivity along the axial direction of the tubes but is thermally insulating along the radial direction. The room-temperature thermal conductivity of a SWNT can be 1750-5800 W/m-K, comparable to that of diamond or in-plane graphite (~6000 W/m-K at peak and 2000 W/m-K at room temperature) [76].

Because of the covalent  $sp^2$  bonds formed between carbon atoms, CNTs are one of the strongest and stiffest materials in terms of tensile strength and elastic modulus, respectively. For individual MWNTs, the tensile strength is from 11 to 63 GPa, and the Young's modulus of the outermost layer varies from 270 to 950 GPa [77]. The manner in how the graphene sheets are wrapped into CNTs is described by a pair of indices (m,n), called chirality (see Fig. 2.17). The (m,m) nanotubes are called "arm-chair" (see Fig. 2.18a), and the (m,0) nanotubes are called "zigzag" (see Fig. 2.18b and 2.18c), while the other types are classified as "chiral" [19]. CNTs are either metallic or semiconducting parallel to the tubes depending on the chirality. All "armchair" CNTs are metallic. Most "zigzag" CNTs are semiconducting except when  $m-n=3i$  (i is an integer); the nanotubes are semimetals with very small band gap [19]. For metallic SWNT, the carrier mobility can be  $\sim 10,000 \text{ cm}^2/\text{V-s}$ , which is better than that of silicon; and the electric current density can be  $\sim 4 \times 10^9 \text{ A/cm}^2$ , which is 1000 times greater than normal metals like copper or aluminum [78].

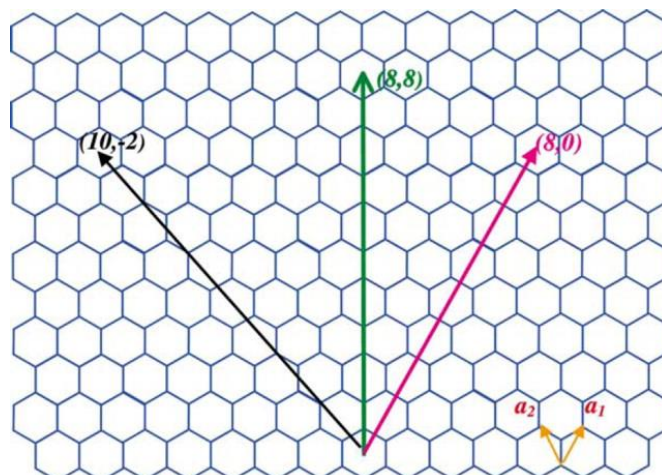


Figure 2.17. Schematic honeycomb structure of a graphene sheet, Carbon atoms are at the vertices. SWNTs can be formed by folding the sheet along lattice vectors. The two basis vectors  $a_1$  and  $a_2$ , and several examples of the lattice vectors are shown (reproduced with caption from [19]).

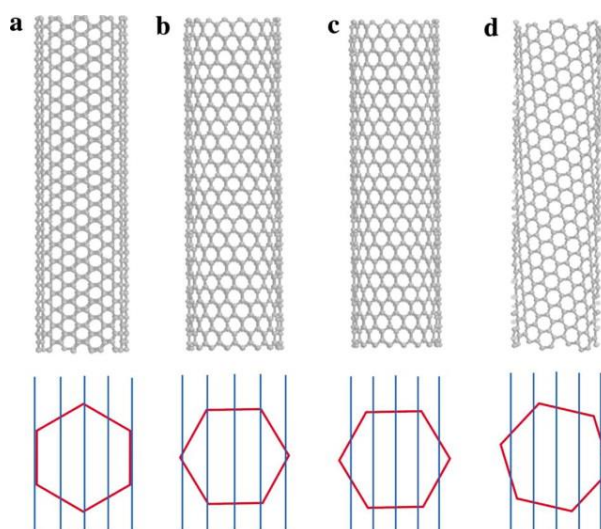


Figure 2.18 Schematic structures of SWNTs. (a) A (10,10) arm-chair nanotube (metallic nanotube). (b) A (12, 0) zigzag nanotube (a small band gap can develop due to the curvature of the nanotube). (c) The (14, 0) zigzag tube (semiconducting nanotube). (d) A (7, 16) tube is semiconducting. This figure illustrates the extreme sensitivity of nanotube electronic structures to the diameter and chirality of nanotubes (reproduced with caption from [19]).

### 2.3.2 CNT Synthesis

Iijima discovered CNTs using an arc-discharge method [75]. A variety of techniques has been developed for the production of CNTs in past decades. Current preparation methods include chemical vapor deposition (CVD), flame synthesis, pulse-laser deposition (PLD). Gas-phase techniques have advantages in large-scale manufacturing and quality. Transition metal catalyst is normally needed for gas-phase growth of CNTs. Both single-walled and multi-walled carbon nanotubes have been produced with or without a substrate.

#### *2.3.2.1 Arc-discharge*

The arc-discharge method utilizes two high-purity graphite rods as the anode and cathode in a low-pressure chamber filled with noble gases such as argon or helium (see Fig. 2.19A). Voltage is maintained between electrodes to form a stable arc that causes the vaporization of the electrode material. Nanotubes then deposit on the cathode where a build-up containing a shell of fused material and a fibrous core consisting of CNTs and other carbon particles is formed [20]. Single-wall carbon nanotubes (SWNTs) can be achieved by doping the electrodes with a small amount of metal catalyst [79]. However, such technique has limitations in scale-up and continuous production. A subsequent purification is necessary to remove undesirable by-products.

### 2.3.2.2 Laser ablation

Laser ablation technique is initially used in the synthesis of fullerenes and developed to produce CNTs. Such approach using a pulse-laser as the energy source is called pulse-laser deposition (PLD). A graphite target is placed in a controlled atmosphere heated by a furnace (see Fig. 2.19B). The laser beam is used to vaporize the graphite target, and CNTs are then collected on a water-cooled target. SWNTs have been produced by using graphite target doped with metal catalyst [80]. Similar to the arc-discharge approach, laser ablation technique is not feasible for large-scale continuous production of high-purity CNTs.

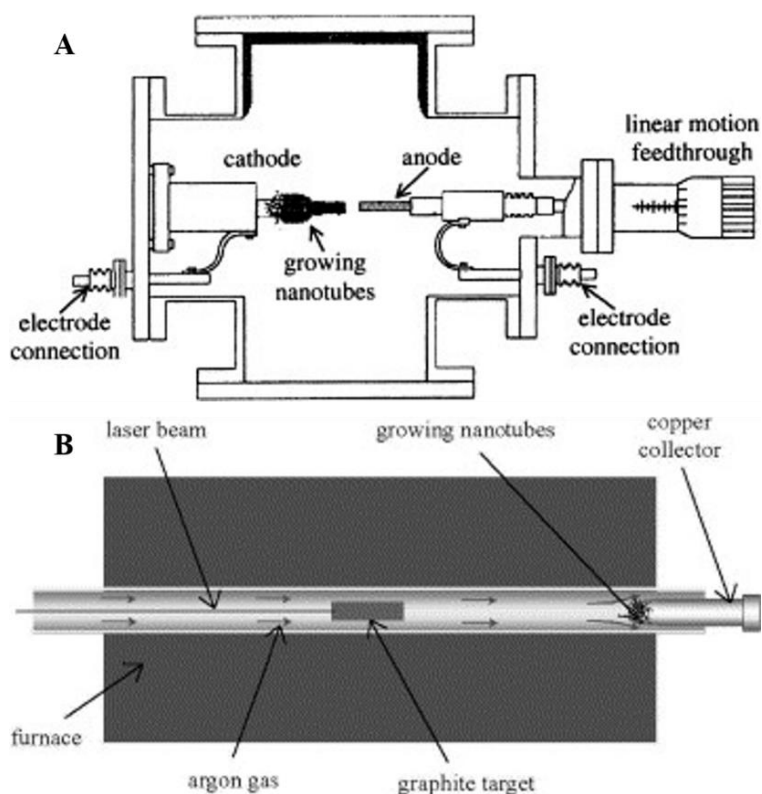


Figure 2.19 (A) Schematic illustration of the arc-discharge method for CNT synthesis. (B) Schematic of the laser ablation process for CNT synthesis (reproduced with caption form [20])

### 2.3.2.3 Chemical vapor deposition (CVD)

Chemical vapor deposition (CVD) has emerged as a viable method for the synthesis of a variety of CNTs, including aligned or entangled on preferred substrates, in powder form, thin or thick films, and straight or coiled [3]. A number of CVD configurations have been tested including horizontal furnace, fluidized bed reactor, vertical furnace, and plasma-enhanced CVD [81]. CNTs have been reported to form in a wide range of temperatures from 600 °C to 1200 °C [3]. Carbon monoxide and light hydrocarbons, such as methane, ethylene, and acetylene are common precursors used in the gas-phase synthesis of CNTs. The metal catalysts used for CNTs growth strongly affect the quality and morphology of CNTs via CVD method. The growth of both SWNTs and MWNTs are reported on iron-based, cobalt-based, and nickel-based catalysts [82]. Alloys of transition metals (Fe, Co, Ni) are found to be more efficient for CNT production than one metal alone. Molybdenum is reported as the most important cocatalyst added to iron or cobalt-based catalysts for the growth of SWNTs [82]. The metal catalyst can be introduced to a CVD process by two means: a) by depositing catalytic seeds on the substrate before synthesis; b) by seeding the precursor gas with metalorganic vapor or catalytic particles.

Gas-phase methods have great potential for large-scale CNT production. Smalley and his co-workers [20] at Rice University refined a high-pressure conversion of carbon monoxide process for the large-quantity production of high-purity SWNTs, which has been commercialized by Carbon Nanotechnologies Inc (Houston, TX). A key advantage of the CVD technique is that it enables the manufacturing of well-aligned arrays of CNTs directly

on metals or insulators for applications. Vertically well-aligned SWNTs have been grown on quartz substrates using Co-Mo catalyst and alcohol precursor [83]. The straightness and diameter of CNTs are controlled by the density and size of the catalytic particles. The alignment of CNT arrays can also be accomplished by the use of an electric field or plasma-enhanced CVD.

### 2.3.3 Carbon Nanotubes Applications

As carbon cylinders rolled from one or more sheets of graphene, CNTs exhibit some exceptional properties similar to graphene, but also have uniqueness their great length-to-diameter ratio. Owing to its remarkable mechanical strength, thermal conductivity, and electrical properties, CNTs afford a large variety of applications including both in devices and as additives to composites.

#### 2.3.3.1 Transistors

Unlike graphene, which is a zero-bandgap semiconductor, CNTs can be metallic or semiconducting depending on the chirality. The statistical analysis suggests 1/3 of total CNTs are metallic. Therefore, the purification of semiconducting CNTs is crucial for transistor application. Jin et al. [84] have demonstrated a technique for creating arrays of pure semiconducting SWNTs using nanoscale thermocapillary flows. Such approach can remove metallic SWNTs from heterogeneous arrays without damaging the semiconducting SWNTs. A significant amount of work has been done on the fabrication of high-



performance CNT transistors since the early 2000s since CNTs are considered as a promising alternative to silicon in much faster and more energy-efficient circuits. IBM, as a leader in CNT transistor research, has achieved effective interface with metal contacts less than 10 nm, outperforming the state-of-the-art silicon chips at 14 nm in 2015. Such a breakthrough is a big step towards the commercial implementation of CNT transistors.

#### *2.3.3.2 Composites*

Because of the extraordinary electrical, thermal, and mechanical properties, along with high aspect ratio, CNTs are good additives or building materials for many functional composites. CNT reinforced polymers exhibit excellent elastic modulus, easily surpassing the limit of carbon fiber (CF) reinforcement at 167 GPa (see Table 2.2). However, adding CNTs into polymers, like epoxy, is much more expensive than adding CFs. Therefore, using both CNTs and CFs as additives to achieve optimal cost-benefit is a viable solution.

Besides additives to composites, CNTs are used as building materials in many advanced nanostructures. Zheng et al. [85] reported a CuO-CNT nanomicrospheres for electrode materials in high-performance lithium-ion batteries. By introducing three-dimensional CNT networks into CuO spheres, the electronic conductivity of the composite material is significantly enhanced. A variety of CNT-based composites has been studied for electrodes of superior batteries. For example, core-shell-structured  $\text{Ru}_2\text{O}$ -CNT composites are used as cathodes in rechargeable lithium- $\text{O}_2$  batteries [86]. Moreover, the

performance of many catalysts can be enhanced when CNTs are incorporated in the structures. By embedding molybdenum sulfide particles on CNT forests, a high-performance catalyst for hydrogen evolution reaction has been obtained[87].

Table 2.2 Elastic modulus, specific modulus and cost of various CNT and CF reinforced composites (reproduced with caption from [2])

	$E_c$ (GPa)	Specific modulus (GPa)/(g/cc)	Cost $C_c$ (\$/kg)
Epoxy+5%CNT	130.4	70.75421	2152.357
Epoxy+20%CNT	425.6	229.8056	8579.429
Epoxy+30%CNT	622.4	334.9839	12864.14
Epoxy+50%CF	136	72.72727	92.5
Epoxy+55%CF	146.4	78.16337	100.75
Epoxy+60%CF	156.8	83.58209	109
Epoxy+65%CF	167.2	88.9835	117.25
Epoxy+1%CNT+64%CF	184.8	98.35019	544.0714
Epoxy+3%CNT+62%CF	220	117.0836	1397.714
Epoxy+5%CNT+60%CF	255.2	135.8169	2251.357
Epoxy+10%CNT+55%CF	343.2	182.6503	4385.464
Epoxy+15%CNT+50%CF	431.2	229.4838	6519.571

## 2.4 Flame Synthesis Background

Flame synthesis, often employed in the flame aerosol mode, is a widely-used technique in commodity particles industry because of its scalability, fast processing time, and low cost. Flame aerosol synthesis has two main categories according to the precursor feeding condition: vapor-fed aerosol flames synthesis, and liquid-fed aerosol flame synthesis (often called flame spray synthesis). The wide availability of liquid precursors enables the rapid

expansion of flame synthesis in complex functional nanoparticles consisting two or more metal elements, such as doped metal oxides, decoration of metal deposits on oxide supports, surface encapsulation, mixed oxides, and heterojunctions [32]. In recent years, hydrocarbon precursors have been used to grow carbon-metal oxide nanocomposites using flame aerosol processes to meet the increasing demand for energy storage devices [21]. Moreover, the growth of CNTs has been extensively studied using the flame aerosol synthesis route.

CVD-type flame synthesis has attracted much research attention in producing thin-film materials such as graphene and CNTs, which exhibit great potential in a wide range of applications. Even though flame synthesis is on the early-developing stage compared with the well-established CVD for thin-film production, some remarkable progress has been made, including the synthesis of FLG and CNT arrays. Flame synthesis is a well-suited technology for the production of nanostructured carbon materials because hydrocarbon fuels can serve as both cheap energy source and reagent needed for synthesis.

#### 2.4.1 Flame Synthesis of Nanostructured Metal Oxides

Flame aerosol synthesis is applied in industry for the large-scale manufacture of ceramic commodities (e.g., pigmentary  $\text{TiO}_2$ , fumed  $\text{SiO}_2$  and  $\text{Al}_2\text{O}_3$ ) and carbon black. Moreover, synthesis of metal oxide nanoparticles (e.g.,  $\text{TiO}_2$ ,  $\text{ZnO}$ ,  $\text{MgO}$ ,  $\text{Al}_2\text{O}_3$ ) and well-defined spinel structures (e.g.,  $\text{ZnAl}_2\text{O}_4$ ,  $\text{MgAl}_2\text{O}_4$ ) with high specific area using gas-phase flame processes have been extensively studied [31], [88]. Compared with the wet-phase-

chemistry process, flame synthesis offers many advantages in producing inorganic particles, such as cost-effectiveness, scalability, and self-purification with respect to the final product. Our current understanding of particle dynamics in the flame flow field and particle diagnostics techniques mostly comes from soot formation, which has been studied for a long time [89]. Besides directly-formed nanoparticles in flames, various morphologies of metal oxides nanostructured films, such as ZnO nanowires, WO<sub>2.9</sub> nanofibers, Fe<sub>3</sub>O<sub>4</sub> nanowires,  $\alpha$ -Fe<sub>2</sub>O<sub>3</sub> nanoflakes, CuO nanowires, and WO<sub>3</sub> nanowires and nanotubes have been synthesized on substrates directly using flame synthesis [90], [91]. A number of flame configurations have been used for nanomaterials synthesis, including premixed, diffusion, counterflow, etc. (see Fig. 2.20).

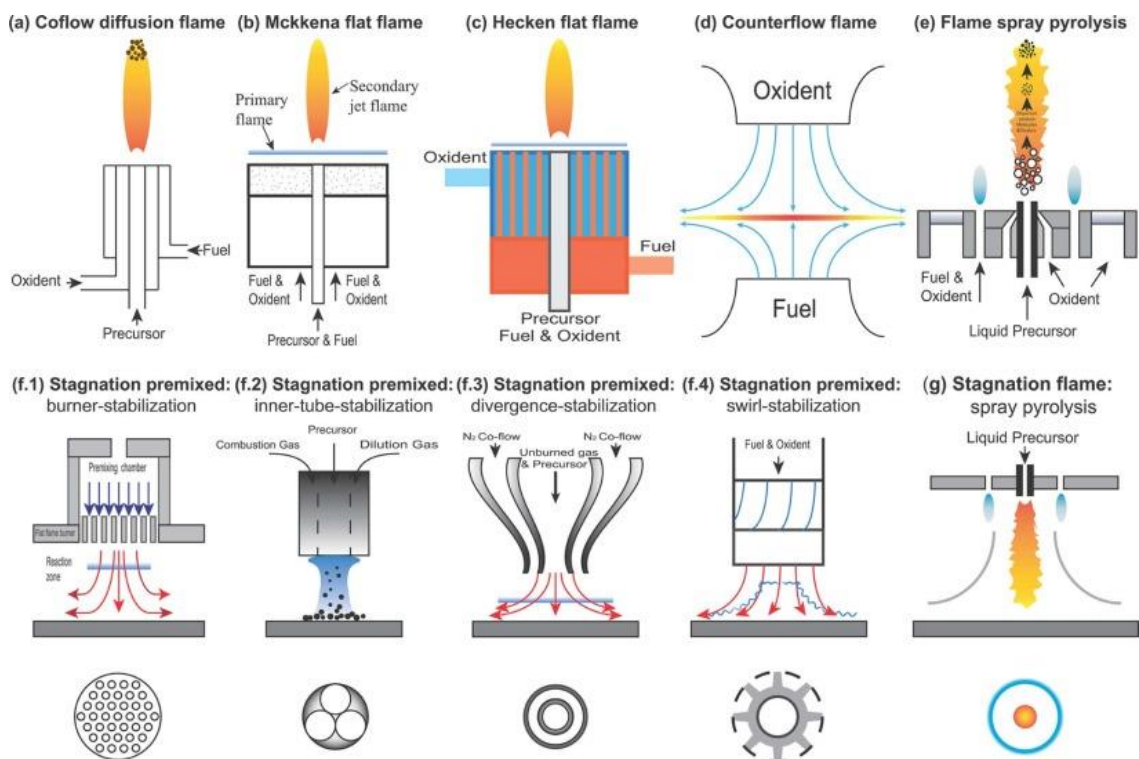


Figure 2.20 Schematic of various typical flame configurations used for nanomaterials synthesis (reproduced with caption from [21]).

#### 2.4.2 Flame Synthesis of Nanostructured Carbon

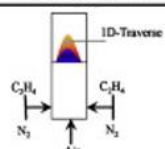


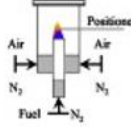

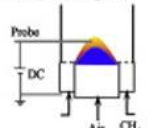
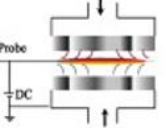
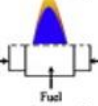
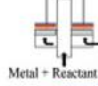

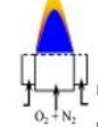
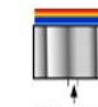

In 1991, Howard and co-workers found fullerenes ( $C_{60}$  and  $C_{70}$ ) in sooty flames [92]. Hydrocarbon flames naturally providing both reactive carbon species and elevated temperatures have great potential for synthesis of carbon nanomaterials at high energy utilization rate and low cost. Since the early 2000s, a lot of work has demonstrated the use of the flame process for CNTs synthesis. Few-layer graphene has been synthesized on copper and nickel using flame synthesis in 2011 [4], [22]. However, the development of flame synthesis for carbon nanomaterials is still in its early stage compared with chemical vapor deposition (CVD) method.

#### *2.4.2.1 Flame synthesis of carbon nanotubes (CNTs)*

Various flame types have been used to synthesize CNTs, such as normal diffusion, inverse diffusion, counterflow, and premixed flames. Both well-aligned and entangled multi-walled carbon nanotubes (MWNTs) have been produced using conventional diffusion flame [93], inverse diffusion flame [94], counterflow diffusion flame [95], premixed flame [96]. Vertical well-aligned MWNTs grown on substrates have been achieved by either applying external electric fields that can control the growth direction of CNTs, or properly adjusting the loading of catalytic particle on substrate to promote a dense growth of CNTs arrays where individual nanotubes attract each other through Van der Waals forces, leading to parallel growing [3].

The flame aerosol method can grow substrate-free CNTs by seeding metal catalyst nanoparticles into sooting flames. The formation of single-walled carbon nanotubes (SWNTs) have been observed in a premixed acetylene flame doped with iron pentacarbonyl [97], and an oxy-ethylene inverse diffusion flame doped with ferrocene[98]. Both processes use a quartz probe to sample SWNTs from aerosol gases. The general mechanism is that carbon precursors decompose on metal catalytic nanoparticles and precipitate out to form CNTs. However, the flame condition is critical for this catalytic process because transition metal nanoparticles can be deactivated under improper flame conditions [21]. A summary of different types of flames used for CNT synthesis with corresponding CNT types is shown in Table 2.3.

Table 2.3 Summary of various types of flame used for CNT synthesis (reproduced with caption from [3])

Author	Burner Configuration	Flame Type	Fuel/Oxidizer	Catalytic Material	Catalyst Delivery	CNT Type
Lee et al. [62]		Inverse diffusion	C <sub>2</sub> H <sub>2</sub> /Air	Stainless steel and Ni(NO <sub>3</sub> ) <sub>2</sub>	Solid support (Stainless steel plate coated with Ni(NO <sub>3</sub> ) <sub>2</sub> )	MWCNT & CNF
Howard et al. [58]		Premixed	C <sub>2</sub> H <sub>2</sub> , C <sub>2</sub> H <sub>4</sub> , C <sub>2</sub> H <sub>6</sub> / O <sub>2</sub> +diluent	None	None	
Yuan et al. [60,61]		Co-flow diffusion	CH <sub>4</sub> [54] & C <sub>2</sub> H <sub>6</sub> [61]/Air	Stainless steel and Ni-Cr-Fe	Solid support (stainless steel grid held by a Ni-Cr-Fe wire-(i)-(60,61) and electroplated with cobalt-(ii)-(61)	Entangle [60,61], straight & bamboo-like (i), and aligned MWCNT (ii) [61]
Vander Wal et al. [94]		Pyrolysis flame encircled by a premixed	C <sub>2</sub> H <sub>2</sub> /Air	Nebulizer (Ni-nitrate solution)	Reactant gases	CNF
Xu et al. [66]		Co-flow diffusion	CH <sub>4</sub> /Air	Transition metal alloy probes with various compositions (e.g. Fe, Ni/Cu, and Ni/Cr/Fe)	Solid support (transition metal alloy wires with various compositions, e.g. Fe, Ni/Cu, and Ni/Cr/Fe)	MWCNTs & WACNTs
Merchan-Merchan et al. [69]		Counter-flow diffusion	CH <sub>4</sub> +C <sub>2</sub> H <sub>2</sub> +N <sub>2</sub> +O <sub>2</sub>	Ni based alloy (73% Ni+17%Cu+10%Fe)	Solid support (Ni based alloy wire)	Aligned, densely, branching & + AL, N12 CNTs
Arana et al. [82]		Co-flow diffusion	C <sub>2</sub> H <sub>2</sub> /Air	Fe (as stainless steel), Ni and Pt	Solid support (stainless steel, Ni and Pt wires)	CNTs, aligned CNTs and CNFs
Vander Wal et al. [110,111]		Pyrolysis flame encircled by a premixed flame	C <sub>2</sub> H <sub>2</sub> /Air	Nebulizer (Fe-Nitrate-salt-solution) [110]; & Nebulizer (Ni-nitrate solution) [111]	Reactant gases	SWCNT
Height et al. [121,122]		Premixed	C <sub>2</sub> H <sub>2</sub> /O <sub>2</sub> -Ar	Iron pentacarbonyl - Fe(CO) <sub>5</sub>	Argon gas	SWCNT
Unrau et al. [134]		Inverse diffusion	C <sub>2</sub> H <sub>2</sub> /O <sub>2</sub>	Ferrocene	Fuel + Nitrogen gases mixture	SWCNT
Diener et al. [118]		Premixed	C <sub>2</sub> H <sub>2</sub> , C <sub>2</sub> H <sub>4</sub> & C <sub>2</sub> H <sub>6</sub> / O <sub>2</sub>	Fe, Ni (Ferrocene & nickelocene)	Argon gas	SWCNT
Richter et al. [133]		Premixed	Natural gas or CH <sub>4</sub> /O <sub>2</sub>	Fe(CO) <sub>5</sub>	Premixed gas mixture	Highly purified SWCNT

Vertically well-aligned SWNTs have been deposited on insulators (e.g., Si) in CVD using different catalytic seeding processes. However, well-aligned CNT arrays or SWNTs directly growing on insulators have not been reported. Compared with the CVD process, the control of gas-phase species is more difficult in flames because of the active chemical reactions at high temperature. The interactions between catalytic particles on the substrate and gaseous species in flame flow fields make the growth of SWNTs or well-aligned CNTs very challenging.

#### *2.4.2.2 Flame synthesis of graphene*

The amount of literature on flame synthesis of graphene is very limited because of the isolated graphene layer was only discovered in 2004 and the difficulty of graphene growth compared with CNTs. In 2011, few-layer graphene (FLG) films were first synthesized on metal substrates using a dual-flame and a multiple inverse-diffusion flame setup (see Fig. 2.21). An alcohol burner and a butane-fueled Bunsen burner are placed perpendicularly to form an overlapped inner flame region where graphene films are deposited on nickel (Ni) foil based on a non-equilibrium surface segregation process similar to CVD [22]. In the dual flame system, the protection flame surrounded the Ni substrate for the whole time of synthesis provides the carbon source and prevents oxidizer diffusion from the ambient. The other burner is basically used to maintain the high temperature ( $>800^{\circ}\text{C}$ ) for carburization. Such approach is an adaptation of the technique used for amorphous carbon



thin film, so amorphous carbon impurities are reported to form along with the graphene [22].

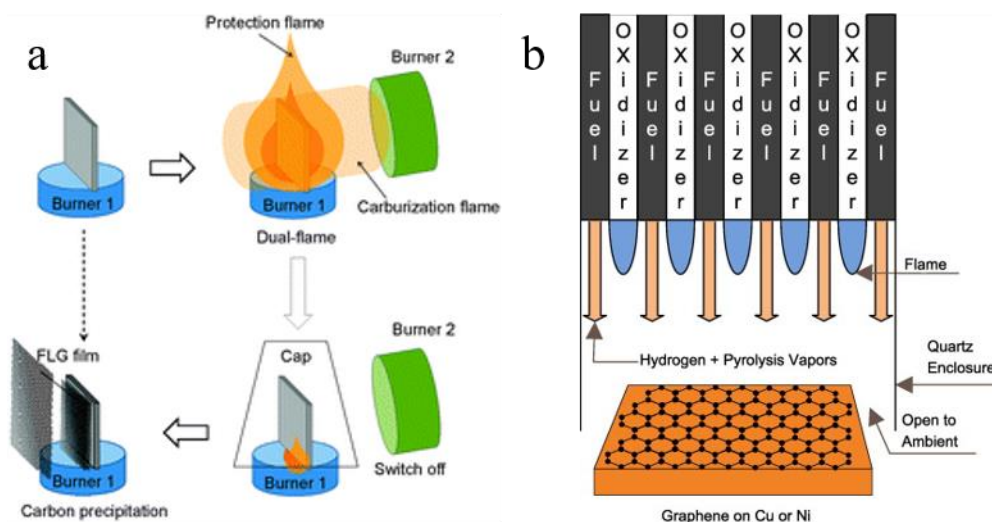


Figure 2.21 Schematic of the flame synthesis of FLG film using a) dual flame method, b) multiple inverse-diffusion flame method (reproduced with captions from [4], [22])

The multiple inverse-diffusion flame burner consists of hundreds of tiny diffusion flames running in under-ventilated condition, where oxidizer in the center is fully consumed (oxygen mole fraction  $\sim 10^{-8}$  in the post-flame gases) to elevate temperature, and excess hydrocarbon in the surrounding fuel provides the carbon source for graphene growth on the substrate [4]. By utilizing multiple inverse-diffusion flames, FLG films have been grown on Cu, Ni, Co, Cu-Ni alloy and  $\text{CuFe}_2\text{O}_4$  substrates [99], [100]. The overall radially-uniform profiles of temperature and chemical species downstream of the flames enable the study on the role of substrate temperature, precursor, and hydrogen. FLG films are observed on Ni and Co at substrate temperatures from 600 °C to 750 °C, while graphene

growing on Cu starts at 750 °C [99]. Moreover, a transition from FLG films growth to CNTs growth on nickel alloy by decreasing substrate temperature from 800 °C to 500 °C has been demonstrated [101]. Multiple inverse-diffusion flame burner exhibits an advantage in the fundamental study of graphene growth condition by flames and has no problem with scale-up. Nevertheless, monolayer graphene growth has not been previously reported via any open-atmosphere flame synthesis method.

## 2.5 Summary

Nanostructured carbon materials, specifically graphene and CNTs, exhibit remarkable physical and chemical properties, which are needed by many advanced applications such as post-silicon transistors, next-generation electronics, and energy storage. The growing level of environmental awareness leads to an increasing demand for clean energy technology where carbon nanomaterials can play a vital role. Hence, some material scientists call graphene and CNTs “the Materials of this Century.” Scalable production methods for graphene and CNTs are urgently required. Flame synthesis, in readily providing essential high temperatures and active carbon species, has the potential for large-scale manufacturing of nanostructured carbon materials.

## Chapter 3

### 3. Experimental Setup

#### 3.1 Modified Multi-Element Inverse-Diffusion Flame Burner

A schematic of the modified multi-element inverse-diffusion flame setup is shown in Fig.

3.1. Each distinct flame in the planar array of the burner surface runs in an inverse mode (“under-ventilated”). Distinct precursor delivery tubes are staged above the burner surface at a fixed height of 5 mm in order to deliver hydrocarbon precursor (e.g., methane, ethylene, acetylene, etc.) to the post-flame region directly. This design prevents hydrocarbon precursor from fully oxidizing/decomposing by bypassing the multiple flames. At the burner base, oxidizer (e.g., air or oxygen) is delivered through small individual oxidizer tubes. Both precursor and oxidizer tubes are made of stainless steel and mounted through a stainless steel honeycomb fixture. Fuel (e.g., hydrogen, methane, ethylene, acetylene, etc.) is delivered through the empty channels of the honeycomb fixture. Water cooling is achieved by use of copper coil wrapped around the burner. A quartz cylinder encompassing the flame and post-flame regions, preventing air permeation from the ambient and reduces convection heat losses. The quartz cylinder is open at the downstream end, after a certain length, exhausting to a hood. Therefore, the setup is open to atmospheric condition.

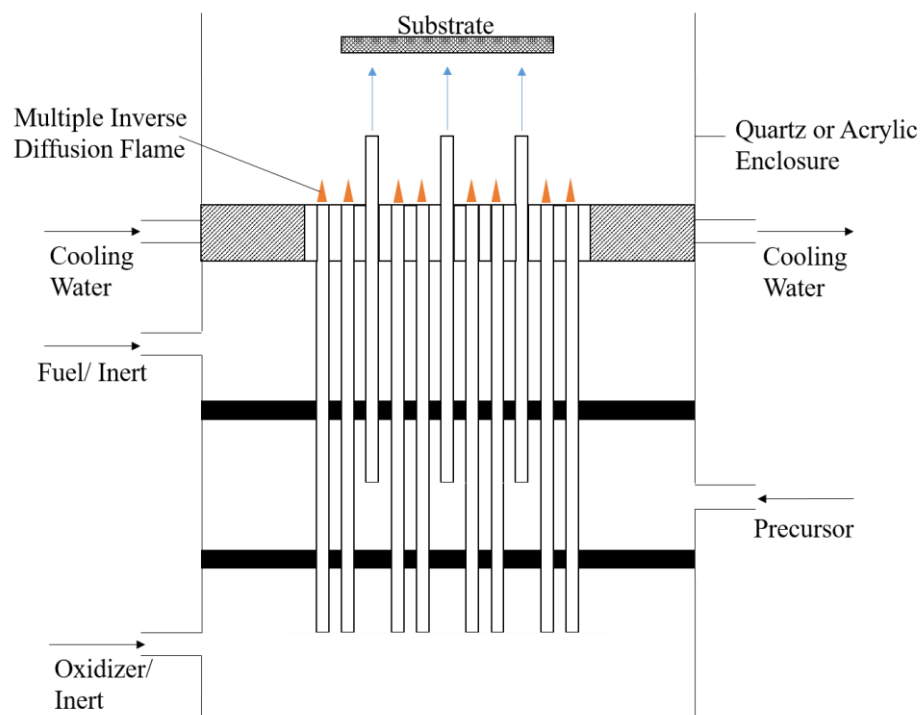


Figure 3.1 Schematic diagram of a modified m-IDF setup modified with uniform-distributed precursor tubes staged above the burner surface at a fixed height.

All the gas flow rates are regulated by mass flow controllers (MFCs, Emcore). A custom LabVIEW program on a PC is used to control the MFCs for convenient and precise flow delivery of multiple gases (see Fig. 3.2). It reduces the experimental error from the control side, which ensures the reproducibility of the results. Excess fuel and precursor are consumed in an after-burner mounted downstream of the open end of the quartz cylinder before exhausting into a hood. The substrate is mounted to a rod and inserted into the post-flame flow field from the open end of the quartz cylinder. The rod has threads that enable adjustment of the substrate height with respect to the burner base. A

sidewall slot is machined into the quartz cylinder to allow access for an igniter and thermocouple.

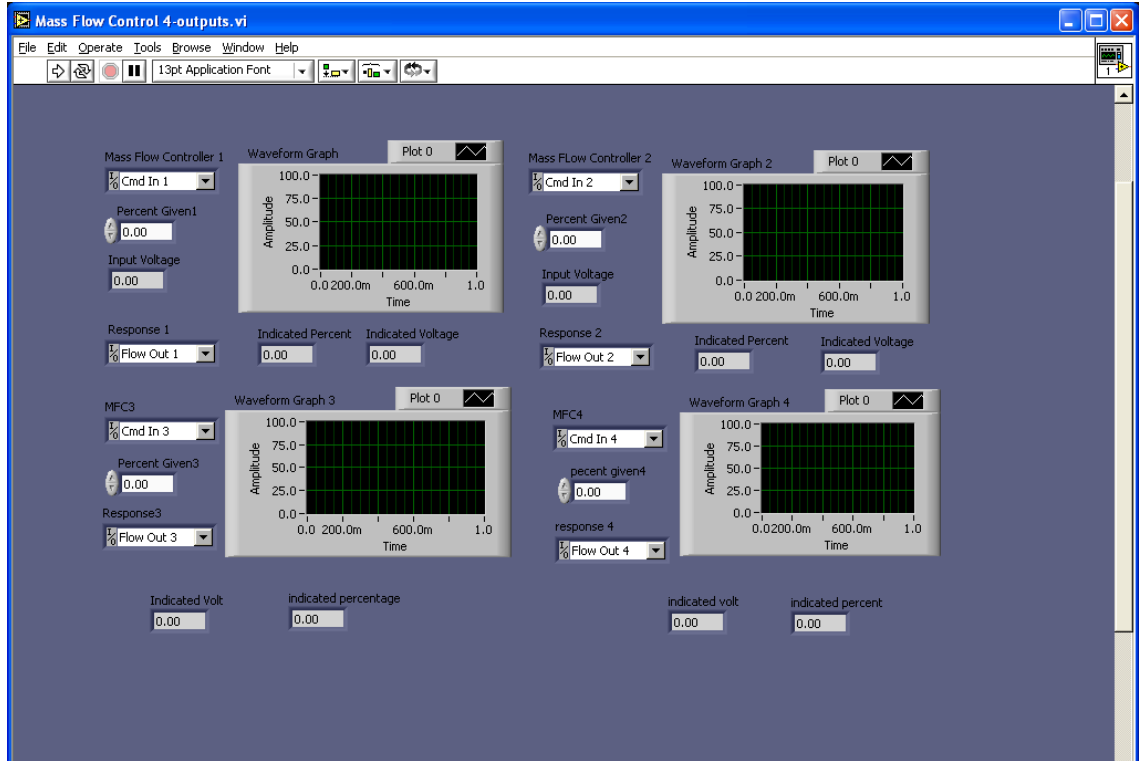


Figure 3.2 Screenshot of LabVIEW program for controlling MFCs.

### 3.2 Numerical Simulation

A flame simulation is conducted using ANSYS Fluent to determine the height of precursor tubes prior to modifying the m-IDF burner. Gambit is used to define the geometry and mesh, which comprises four individual flames. Both two-step laminar reaction for methane/air based on Arrhenius kinetics and GRI-Mech 1.2 are used to model the flames and guide construction of the final burner. Our previous experimental data serve as flow rate inputs in the simulation. Employing adiabatic radial boundary conditions, the results

of using the two-step laminar reaction mechanism is shown in Fig. 3.3a. As can be seen, the temperatures from the individual flames merge at  $\sim 5$  mm above the tubing exits (the length of the tubes is 10 mm), and the radial boundary has a constant temperature  $\sim 1600$  K after flames merge. A simulation of constant temperature radial boundary condition at 1600 K using detailed chemical kinetics, i.e., GRI-Mech 1.2 mechanism, is then performed (see Fig. 3.3b). The individual flame temperatures merge in a shorter distance than in they do using the two-step mechanism. Based on the simulation results, we modify the m-IDF burner design with distinct precursor tubes elevated above the burner surface at a fixed height of 5 mm.

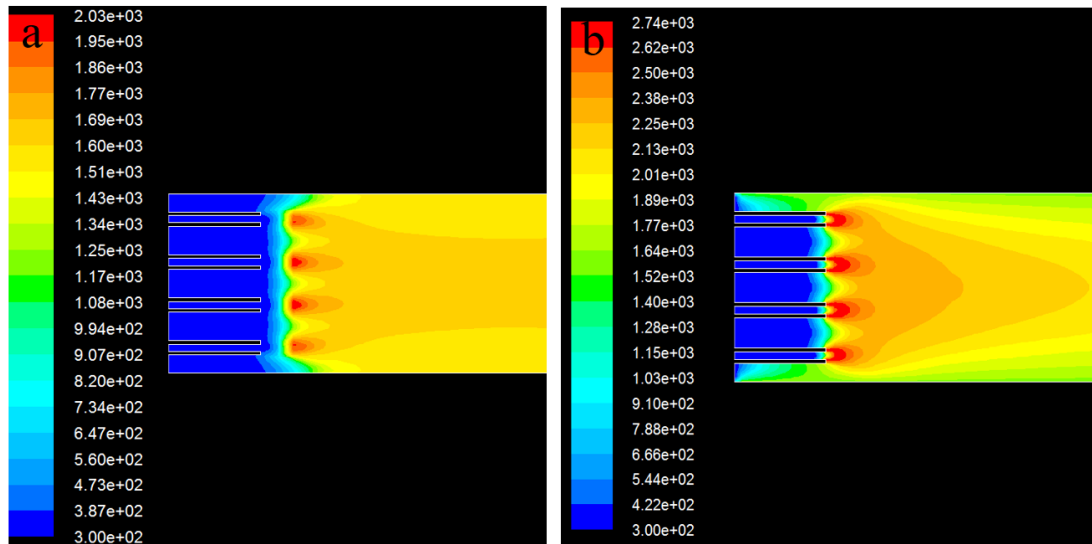


Figure 3.3 Fluent Computation Fluid Dynamics (CFD) simulation results of the m-IDF burner at adiabatic boundary condition using two-step laminar reaction mechanism (a), constant temperature boundary condition (1600 K) using GRI-Mech 1.2 mechanism (b).

### 3.3 Temperature Measurement

Gas-phase temperatures are measured using a 125  $\mu\text{m}$  Pt/Pt - 10% Rh thermocouple (S-type, OMEGA, Model: P10R-005). A silica coating is applied to the thermocouple junction to prevent catalytic oxidation on the Pt-based thermocouple. The coating is performed using a small co-flow burner, where silicone oil is injected using a syringe pump. The coating uniformity ( $3 \pm 0.5 \mu\text{m}$ ) is confirmed under a microscope. The thermocouple is held for 2 seconds within the flame, and the procedure is repeated multiple times to minimize error.

### 3.4 Experimental Procedures

Please find detailed steps of the experiment in the appendix.

### 3.5 Sample Preparation

Substrates used for these experiments consist of various metals and non-metals including copper foil and plate, nickel foil, stainless steel foil, silicon wafer and several others. All substrates are cut into 1.5 cm x 1.5 cm squares and placed above the burner, but within the encompassing quartz cylinder. The substrate can be positioned parallel to the flame flow, or perpendicular to the flow, or tilted an angle with the flow. In all cases, no prior substrate preparation is performed. A list of the substrate materials is shown in Table 3.1.

Table 3.1 List of substrate investigated

Material	Purity	Thickness	Company	Part #
Copper Foil	99.8%	0.025 mm	Alfa Aesar	13382
Puratronic Copper Foil	99.9999%	0.25 mm	Alfa Aesar	42974
Puratronic Copper Foil	99.9999%	0.1 mm	Alfa Aesar	42973
Nickel Foil	99%	0.025mm	Alfa Aesar	12722
Silicon Wafer (1 0 0)	*N-Phosphorus	381 microns	El-Cat	30
Silicon Wafer (1 0 0)	*P-Boron	500 microns + 300nm oxide	University Wafer	43
Stainless Steel 304 Foil	N/A	0.025 mm	Alfa Aesar	41580
Stainless Steel 304L Foil	N/A	0.15 mm	Goodfellow	FA140230
Stainless Steel 316L Foil	N/A	0.05 mm	Goodfellow	FF210250

### 3.6 In-situ Raman Spectroscopy

The second harmonic (532 nm) of an injection-seeded Nd:YAG laser (Quanta-Ray LAB 170) operating at 10 Hz (~9 ns FWHM) is utilized for in-situ Raman measurement of gas-phase species as shown in Fig. 3.4. The laser beam is focused by a 500-mm focal-length plano-convex fused-silica lens to a probe volume with a waist diameter of approximately 200  $\mu\text{m}$ . A spectrometer (Acton SpectraPro-500i) with a 600 groove/mm grating and an ICCD camera (Princeton Instruments, PIMAX 1300HQ-25-FO) are used for imaging. The slit of the spectrometer is 200  $\mu\text{m}$ . An oscilloscope (Agilent Infiniium 54845A, 1.5 GHz sampling rate) is employed to monitor the timing of the laser pulse and camera gating. The camera gate width time is set to 20ns to reduce interference and background.



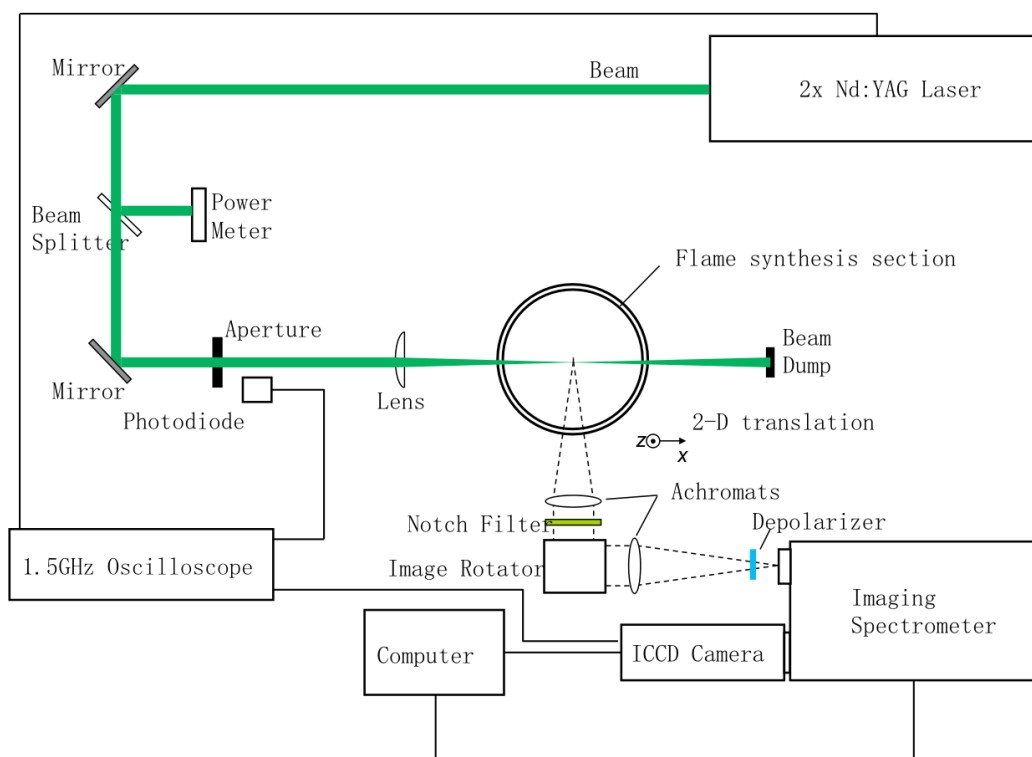


Figure 3.4 Schematic diagram of the in-situ Raman measurement setup. The burner is located on a 2-D translator in order to move in x and z directions. The emissions are collected at  $90^\circ$  by a 400-mm focal-length achromatic lens, passed through a Raman holographic notch filter (Kaiser HSPF-532.0-2.0), focused by a 300-mm focal-length achromatic lens onto the slit of a 0.5m imaging spectrometer.

### 3.7 Ex-situ Characterization Techniques

Equipment used to characterize the growth of graphene, CNTs, and iron oxide is summarized in Table 3.2.

Table 3.2 List of characterization techniques

Technique	Equipment
Raman Spectroscopy	Renishaw 1000, laser excitation 514.5 nm
Scanning Electron Microscopy	Zeiss Sigma 8100
Transmission Electron Microscopy	JEOL 2010F
Scanning/Transmission Electron Microscopy	FEI Talos F200X S/TEM
UV-Vis Spectroscopy	ThermoFisher Evolution 300 UV-Vis Spectrometer
Atomic Force Microscopy	Bruker Dimension FastScan
X-ray Photoelectron Spectroscopy	Thermo Scientific K-Alpha

### 3.7.1 Raman Spectroscopy

Raman scattering is the inelastic scattering of an incident photon upon interaction with an atom or molecule. When incident photons are scattered from matter, most of them are elastically scattered (Rayleigh scattering) at the same frequency as the incident photons. If the scattered photons have lower frequencies than that of incident photons, the scattering is called Stokes scattering, giving the Stokes lines in the Raman scattering spectrum. To the contrary, if the scattered photons have higher frequencies, the scattering is called Anti-Stokes scattering, giving the Anti-Stokes lines. An illustration of energy transitions leading to Rayleigh, Stokes, and Anti-Stokes spectra is shown in Fig. 3.5A with the corresponding Rayleigh, Stokes, and Anti-Stokes lines shown in Raman scattering spectrum (see Fig. 3.5B).

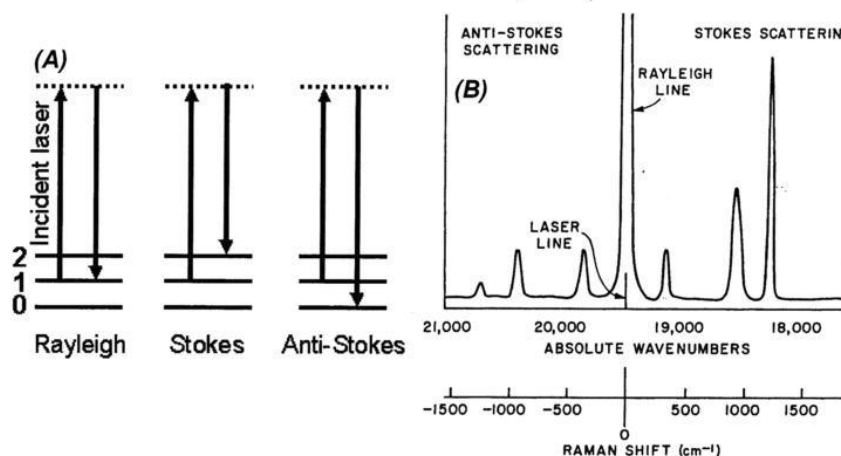


Figure 3.5 A) Illustration of energy transitions leading to Rayleigh, Stokes and Anti-Stokes spectra. B) Schematic Raman scattering spectrum showing Rayleigh line, Stokes and Anti-Stokes Raman lines (reproduced with caption from [23], [24]).

Raman spectroscopy is a widespread spectroscopic technique used to observe vibrational and rotational modes within a system. It has been extensively used in characterizing various carbon systems (e.g., amorphous carbon, metallic and semiconducting SWNTs, graphite, etc.) with only a few prominent features including a couple of very intense bands in the 1000-2000  $\text{cm}^{-1}$  range and few other second-order modulations (See Fig. 3.6). In the Raman spectra of carbon, the main bands are called G and D peaks, which are located at around 1560 and 1360  $\text{cm}^{-1}$ , respectively, for visible excitation. The G peak is related to the bond stretching of all pairs of  $\text{sp}^2$  atoms in both rings and chains, and the D peak is related to the breathing modes of  $\text{sp}^2$  atoms in rings [25]. All  $\text{sp}^2$  carbon materials normally present a strong peak called G' (or 2D) peak in the range 2500-2800  $\text{cm}^{-1}$ . For monolayer graphene, the G peak appears at 1582  $\text{cm}^{-1}$ ,

and the G' peak at about  $2700\text{ cm}^{-1}$ , using  $514\text{ nm}$  excitation (see Fig. 3.7). At the edge of a graphene sample or in the case of a disordered sample, a disordered-induced D peak manifests at around  $1350\text{ cm}^{-1}$  [26]. In defective graphite, there is a so-called D' peak (at  $\sim 1620\text{ cm}^{-1}$ ) resulting from the double resonance process [26]. The ratio between G and G' peaks can be used to estimate the number of graphene layers (see Fig. 3.8). and the ratio between D and G peaks can be used to measure the disorder induced from edges, impurities, domain boundaries, wrinkles, etc.

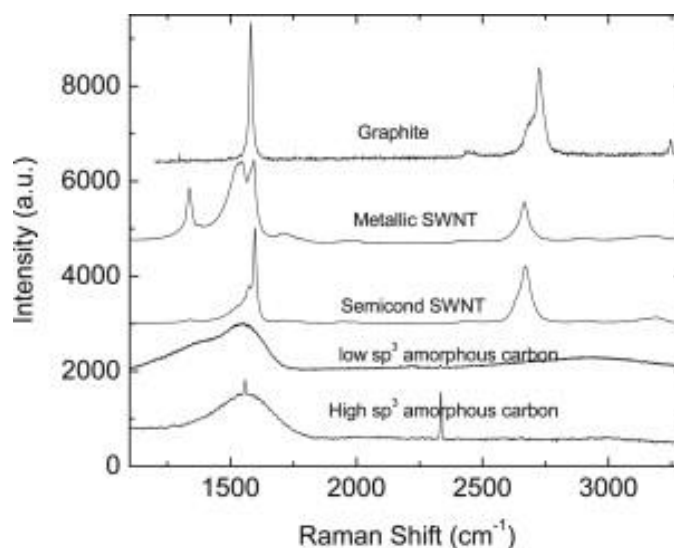


Figure 3.6 Raman spectra of graphite, metallic and semiconducting CNTs, low and high  $\text{sp}^3$  amorphous carbons (reproduced with caption from [25]).

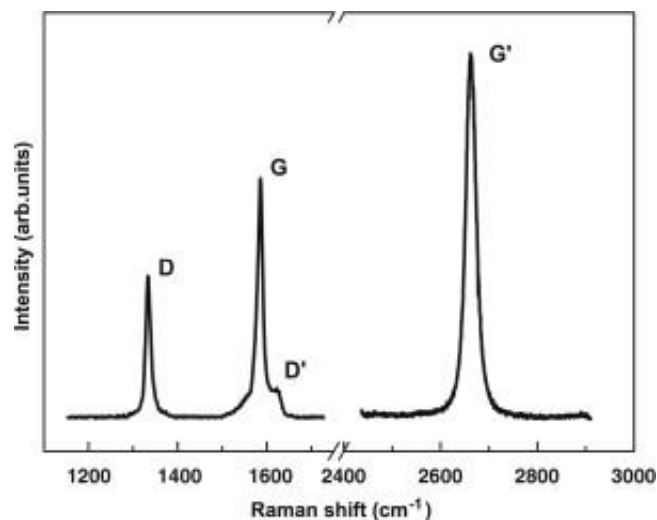


Figure 3.7 Raman spectrum of a graphene edge using 514 nm excitation (reproduced with caption from [26]).

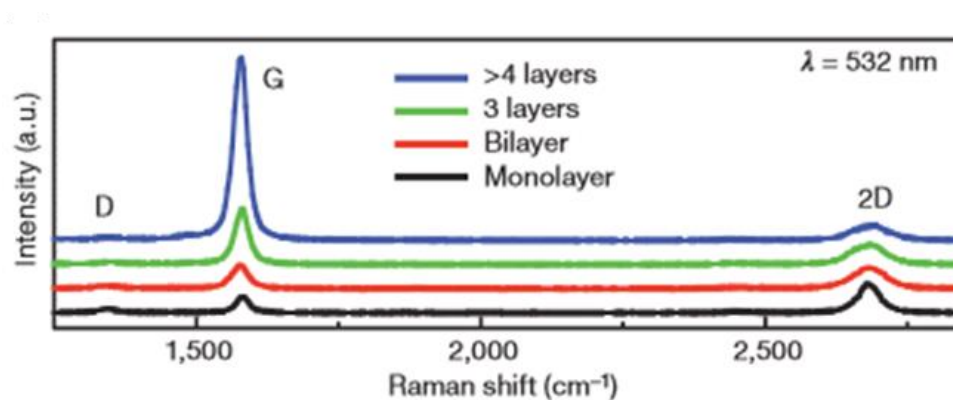


Figure 3.8 Raman spectra of graphene with various numbers of layers (reproduced with caption from [27]).

### 3.7.2 Scanning Electron Microscopy

Scanning electron microscope (SEM) is an advanced analytical microscope used for imaging a sample's surface topography by scanning it with a focused beam of electrons. The Zeiss Sigma 8100 setup employed in this work is a field-emission SEM (FE-SEM),

which can produce high-resolution images at low accelerating voltages. SEM is commonly used to determine the morphology and composition of nanostructured material. In this work, CNTs and iron-oxide nanoparticles are characterized by SEM.

### 3.7.3 Transmission Electron Microscopy

A beam of accelerated electrons is transmitted through an ultra-thin specimen in a transmission electron microscope (TEM). The wave interactions of the electrons transmitted through the specimen give significantly higher-resolution information compared with optical microscopes since the De Broglie wavelength of electrons is many orders of magnitude smaller than that for visible light. TEM is widely used for imaging crystal structures of nanomaterials. Another main function of TEM is selected area electron diffraction (SAED) that can be used to determine the crystallinity of samples. A high-resolution TEM (HRTEM) is used to characterize graphene sample in this work.

### 3.7.4 Atomic-Force Microscopy

Atomic-force microscopy (AFM) is a type of scanning probe microscopy with nano-scale resolution. A cantilever with a sharp probe at its end is used to scan the surface depth profile of the samples. The AFM can be operated in either static (contact) mode or dynamic (tapping or non-contact) mode for a number of applications. In static mode, where the probe tip is dragged across the specimen surface, a firm contact with the solid surface is required. In tapping modes, short-range forces are detected by oscillating the

cantilever probe tip close enough to the sample surface without contact. Tapping mode that prevents the tip from sticking to or damaging the surface is more suitable for thin-layer materials like graphene. AFM is employed to determine the morphology and uniformity of graphene samples on a silicon wafer (surface roughness  $\sim 1$  nm). All AFM tests are conducted in collaboration with Jiangbo Liu from Prof. Zou's group.

### 3.7.5 X-ray Photoelectron Microscopy

X-ray photoelectron spectroscopy (XPS) is a quantitative technique for measuring the elemental composition and chemical state of a material surface. The sample is irradiated with a beam of X-rays in high vacuum or ultra-high vacuum while the kinetic energy and number of electrons escaping from the top 0 to 10 nm of the material are measured and analyzed. The chemical state, specifically bonding environment of iron oxide samples are determined by XPS.

### 3.7.6 X-ray Diffraction

X-ray diffraction (XRD) is an X-ray crystallography technique used to characterize the atomic and molecular structures of crystalline materials. The beam of incident X-ray waves is elastically scattered by the arrays of atoms in a crystal, producing a diffraction pattern of regularly spaced spots. By converting the diffraction patterns to the density of electrons within the crystal using Fourier transformation, the atomic structure, chemical

bonds, and other information can be determined. The crystal phases of iron oxide samples are identified by XRD.



## Chapter 4

### 4. Fundamental Study of Graphene Growth Conditions Using Unconfined Flame

#### Synthesis

##### 4.1 Introduction

The exceptional physical and chemical properties of graphene afford a wide range of applications from next-generation electronics to novel biomedical devices. To enable the practical applications of graphene, an affordable manufacturing method suitable for large-scale production is sought. A number of different synthesis methods have been studied over the past decade. Mechanical exfoliation is the method used to isolate the first monolayer graphene, discovering its excellent electrical and photonic properties [6]. However, such approach lacks scalability. Liquid-phase exfoliation has demonstrated great potential in the large-amount production of defect-free few-layer graphene [12], but as-produced graphene flakes are not feasible for many electronic and optical applications. Gas-phase bottom-up methods are considered more viable in large-scale production of high-quality graphene for electronic, photonic, or optical use. Epitaxial growth of graphene on silicon carbide (SiC) provides graphene product directly synthesized on an insulator and ready for many electronic applications, but the high cost of SiC substrates prevents it from commercial feasibility. Chemical vapor deposition (CVD), often used in semiconductor industry to produce thin films, has achieved high-quality graphene

deposition on transition metals such as nickel (Ni) and copper (Cu) through two main catalytic growth mechanisms: a) carbon bulk diffusion and segregation in transition metals, b) self-limiting surface growth on Cu (see Fig. 4.1) [28]. Nevertheless, CVD process has a limitation in growing graphene film over large areas, along with disadvantage in cost because of the need for a vacuum chamber and electrical heating. Flame synthesis, a widely used method in the pigment industry, offers an alternative gas-phase method for graphene production at large-scale and reduced cost. The growth process of graphene on transition metals in flames should be similar to a CVD process because similar gas species and substrate temperatures can be achieved in a well-controlled flame environment.

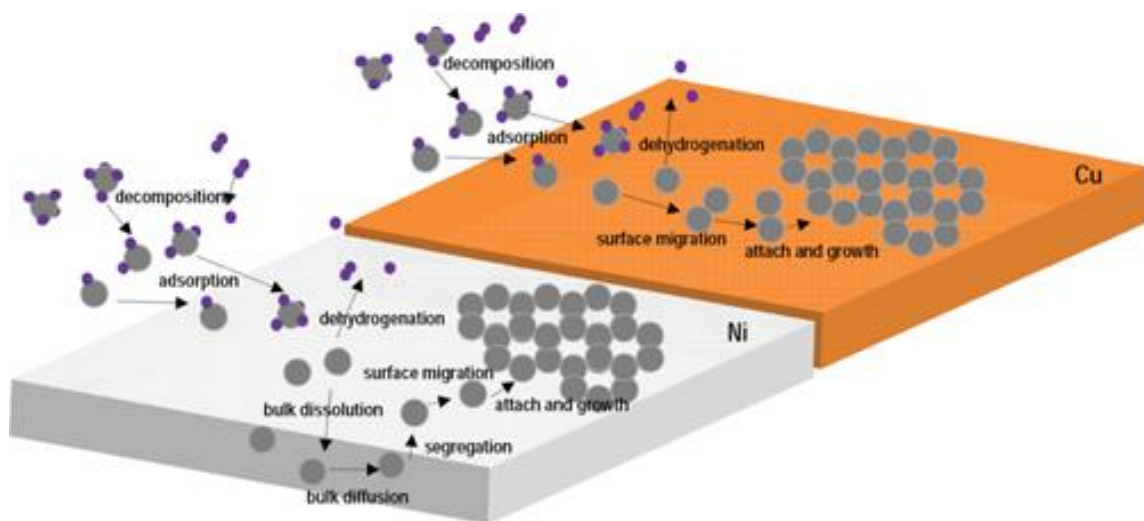


Figure 4.1 Growth kinetics on CVD-produced graphene on various catalysts: Case of CH<sub>4</sub> on Ni and Cu (reproduced with caption from [28]).

Flame synthesis has demonstrated its viability in growing few-layer graphene (FLG) using a dual flame setup or a multiple inverse-diffusion flame burner. However, the

growth of mono- and bilayer graphene using an open-atmosphere flame process remains challenging because of the breakdown of self-limiting growth on copper as pressure is raised to atmospheric pressure. The synthesis configuration employed in this work is based on a modified multi-element inverse-diffusion flame (m-IDF) setup (see Fig. 4.2). The pyrolysis vapors and post-flame species are directed at a substrate to grow graphene. Each of the tiny individual flames operates in the inverse mode (“under-ventilated), where for each flame, the oxidizer (e.g., oxygen diluted with inert) is in the center and fuel (e.g., hydrogen diluted with inert) surrounds it. Far downstream, multiple diffusion flames create a one-dimensional post-flame profile with radially uniform profiles of temperature and chemical species. Such one-dimensional flame in net effect is suitable for the fundamental study of graphene growth in flame. The precursor tubes inject precursor gases (e.g., methane, ethylene) downstream of the flame. This design ensures that hydrocarbon precursor does not pass through or near the multiple flames, avoiding oxidation and dissociation of hydrocarbon species. Since carbon formation process and fuel oxidation process are effectively separated, no soot is observed in the modified m-IDF setup for all experimental conditions. Modified m-IDF has no scaling problem since all flow velocity can be independent of the burner diameter. Such technique affords large-area deposition of nanostructured carbon in open-atmosphere by shielding the setup with an inert co-flow or encompassing tube preventing diffusion from the ambient.

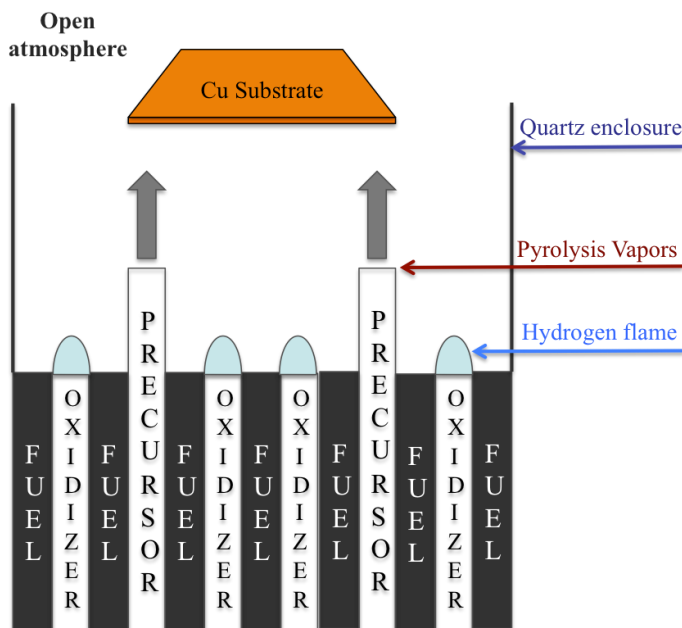


Figure 4.2 The modified m-IDF setup provides fuel-rich hydrogen flame and active carbon species leading to graphene growth on Cu substrate in open-atmosphere.

## 4.2 Experiment

Copper (Cu) and nickel (Ni) foils from Alfa Aesar are used as substrates for graphene growth. The metal foils are placed downstream of the m-IDFs in the post-flame gases at a certain distance (8-12 mm). Prior to graphene growth, the copper substrate is first reduced by running the m-IDFs with only hydrogen as fuel, such that the downstream gases are rich in hydrogen at  $\sim 1000$  °C, for 10 min to remove any oxide layer and to enlarge the grain size on the metal foils. No hydrocarbon species is introduced into the system during this period. To initiate graphene growth, methane, as a precursor, is then introduced into the post-flame region through the precursor tubes directed at the substrate. Bi- and few-layer graphene are grown on copper and nickel substrates for different methane-to-

hydrogen flow rate ratios ( $J_{CH_4}:J_{H_2}$ ), growth temperatures, and durations. An S-type thermocouple (125  $\mu$ m Pt/Pt-10%Rh) coated with silica is utilized to measure the substrate temperature, which ranges from 800 °C to 1000 °C. When the precursor injection period is done, the m-IDFs are extinguished by turning off the oxygen supply. Hydrogen and inert gases continue to flow until the substrate is cooled to room temperature.

As-synthesized graphene can be transferred onto Si/SiO<sub>2</sub> substrates from a Cu substrate by following these steps: i) spin-coat one side of the graphene/Cu/graphene sample with 300 nm-thick polymethyl-methacrylate (PMMA) film and heat in furnace at 150 °C for 5 min to cure the PMMA protection film; ii) immerse PMMA/graphene/Cu/graphene stack in 10% HNO<sub>3</sub> solution for 2 min to remove graphene on the unprotected side and rinse in DI-water for multiple times; iii) float PMMA/graphene/Cu foil in 1 mole/L FeCl<sub>3</sub> solution to etch away all copper substrate; iv) rinse the PMMA/graphene film in DI-water for multiple times and then transfer it onto Si/SiO<sub>2</sub>; v) remove PMMA layer by rinsing in hot acetone and dry at room temperature overnight. Micro-Raman spectroscopy (Renishaw 1000, 514 nm laser wavelength, 50 $\times$  magnitude) is utilized to characterize the quality of graphene on Cu and Si/Si O<sub>2</sub> substrates, post experiment.

#### 4.3 Results and Discussion

Flame synthesis of FLG has been demonstrated on different transition metals, but monolayer graphene (MLG) and bilayer graphene (BLG) have not been achieved using any open-atmosphere flame process. Although the thermodynamics of graphene grown on a

Cu catalyst surface should be the same for both atmospheric- and low-pressure chemical vapor deposition (CVD) processes, the appearance of bi- and few-layer graphene in atmospheric-pressure CVD process reveals that the kinetics (cooling rate, synthesis pressure, methane concentration) impact significantly on the thickness uniformity and quality of graphene growth [13]. Therefore, in this work, a parametric study is performed to optimize flame conditions for graphene growth. Raman spectroscopy enables ex-situ characterization of the quality of graphene, including the number of layers and defective level [26]. For 514 nm laser excitation, the typical Raman spectra of graphene have three prominent peaks, the D peak at  $\sim 1350 \text{ cm}^{-1}$ , which corresponds to the disorders present in graphene layer, the G peak at  $\sim 1580 \text{ cm}^{-1}$ , and the 2D peak at  $\sim 2700 \text{ cm}^{-1}$ . The intensity ratio of G-peak-to-2D-peak ( $I_G/I_{2D}$ ) can be used as a qualitative indicator to estimate the number of graphene layers. For monolayer graphene, the  $I_G/I_{2D}$  ratio is usually around or above 2. The ratios are around 1 and smaller than 1 for bi- and few-layer graphene respectively.

#### 4.3.1 Effect of Substrate Temperature

The formation of amorphous carbon films on Cu has been reported in the temperature range between  $500^\circ\text{C}$  and  $750^\circ\text{C}$  using multiple inverse-diffusion flames [99]. The 2D peak of graphene, which indicates the presence of graphitic carbon structure, starts to appear on Cu at the temperature of  $700^\circ\text{C}$  [4]. Typical Raman spectra of graphitic carbon structures grown on Cu at low-temperature range from  $700^\circ\text{C}$  to  $850^\circ\text{C}$  is shown in Fig.3. The

high  $I_G/I_{2D}$  ratio and the merging of D and G bands imply the growth of amorphous carbon and nanocrystalline graphite at low-temperature [102].

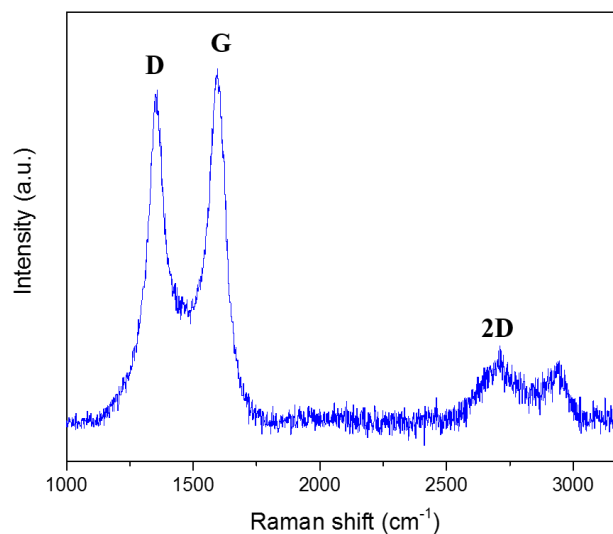


Figure 4.3 Raman spectra of graphitic carbon structure grown on Cu at low-temperature range from 700 °C to 850 °C. Substrate background signals are all subtracted. The spectra are normalized with the G band.

The effective synthesis of FLG is observed at increasing temperatures starting at 850 °C. Raman spectra of graphene grown at different temperatures for a fixed growth duration and  $J_{CH_4}:J_{H_2}$  rate are shown in Fig. 4.4. By increasing synthesis temperatures from 850 °C to 1000 °C, a significant decrease in  $I_G/I_{2D}$  ratio is observed from 2 to 1.2, which implies the number of graphene layers decreases as temperature increases. Graphene with  $I_G/I_{2D}$  ratio of 1.3 has been reported as a tri-layer film [103], and 5 to 10 layers of graphene has been reported  $I_G/I_{2D}$  ratio from 1.8 to 2.4 [59]. A lower intensity of D peak indicates less disorder within the film. This result agrees with the consensus

of CVD processes mostly using  $\sim 1000$  °C [54], [58], [104], which is right below the melting point of copper ( $\sim 1085$  °C), as an optimum growth temperature.

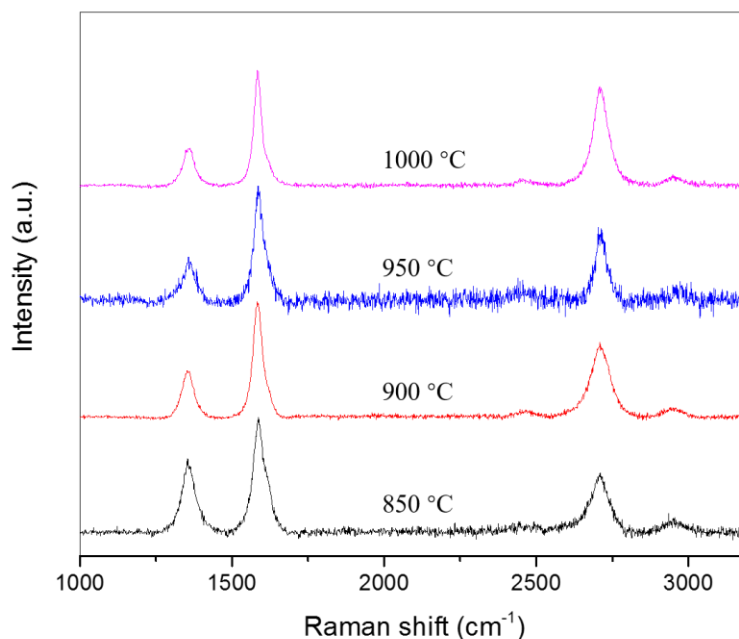


Figure 4.4 Raman spectra of graphene grown on Cu at different temperatures. Substrate background signals are all subtracted. The spectra are normalized with the G band.

#### 4.3.2 Effect of Methane-to-Hydrogen Flow Rate ( $J_{\text{CH}_4}:J_{\text{H}_2}$ ) Ratio

In atmospheric-pressure CVD (APCVD), though not open environment, monolayer graphene growth has been reported at very low  $J_{\text{CH}_4}:J_{\text{H}_2}$  ratios ( $<1:1000$ ) [13]. However, the termination of FLG growth was observed when the methane-to-hydrogen flow rate ratio ( $J_{\text{CH}_4}:J_{\text{H}_2}$ ) is below 1:40, using the multiple inverse-diffusion flames burner [4]. In that flame synthesis experiment,  $\text{CH}_4$  was delivered through the fuel tubes, along with hydrogen, of the m-IDFs burner (and not by separate precursor tubes). Thus, the effect of  $J_{\text{CH}_4}:J_{\text{H}_2}$



ratio is coupled with the flame condition because only excess hydrocarbon species can serve as the active carbon source for graphene growth. Therefore, the concentration of active carbon species in the post-flame region cannot afford graphene growth if the  $J_{CH_4}:J_{H_2}$  ratio is lower than a critical value. Since  $J_{CH_4}:J_{H_2}$  ratio plays a major role in the kinetics of graphene growth, a parametric study of its effect is necessary to optimize the flame synthesis condition.

Taking advantage of the modified m-IDF setup (where extended precursor tubes are utilized), the study of graphene growth is in a wide range of  $J_{CH_4}:J_{H_2}$  ratios because the  $CH_4$  flow rate is now independent of the flame condition. When  $J_{CH_4}:J_{H_2}$  ratio is larger than 1:20, uniform FLG is grown on Cu, which agrees with previously reported results of FLG growth at  $J_{CH_4}:J_{H_2}$  ratios from 1:5 to 1:20 in flame synthesis [4]. A wide range of  $J_{CH_4}:J_{H_2}$  ratios from 1:25 to 1:1000 is studied at a fixed substrate temperature of 1000 °C and growth duration. Raman spectra of graphene grown on Cu with  $J_{CH_4}:J_{H_2}$  ratio varied from 1:25 to 1:100 is shown in Fig. 5. The  $I_G/I_{2D}$  ratio decreases from 1.5 to 1.1 as the  $J_{CH_4}:J_{H_2}$  ratio drops. With decreasing methane flow rate, the density of graphene nucleation sites reduces because of the lessening of the degree of supersaturation of active carbon species on the copper surface to promote graphene nucleation. The reduction in nucleation density often leads to a higher quality growth of graphene with larger domain size and fewer imperfections. However, by further lowering methane concentration to the condition of APCVD, it only leads to a longer time needed for graphene to cover the substrate surface and MLG was not observed in any of the cases. The case of graphene

growth with  $J_{\text{CH}_4}:J_{\text{H}_2}$  ratio at 1:350 for 20 min is nearly identical to the case with  $J_{\text{CH}_4}:J_{\text{H}_2}$  ratio at 1:100 for 10 min. The high flow flux and large numbers of combustion products (e.g.,  $\text{H}_2\text{O}$ ,  $\text{OH}$ ,  $\text{CO}$ ,  $\text{CO}_2$ ) make a flame synthesis configuration different than CVD results. Such open-atmosphere flame process seems to be limited in reducing graphene nucleation sites.

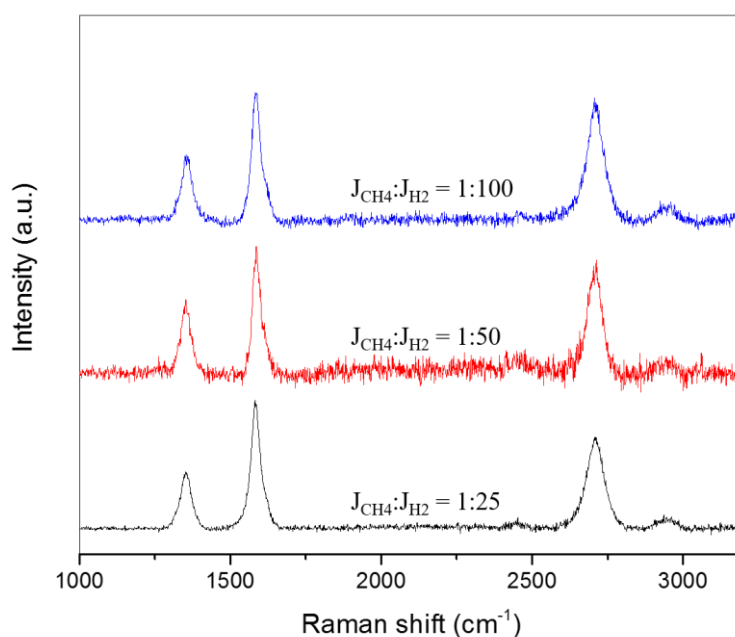


Figure 4.5 Raman spectra of graphene grown on Cu at different  $J_{\text{CH}_4}:J_{\text{H}_2}$  ratios. Substrate background signals are all subtracted. The spectra are normalized with the G band.

#### 4.3.3 Effect of Growth Time

Growth time is another critical parameter for the gas-phase synthesis of graphene at atmospheric pressure since the self-limiting mechanism is not valid in the case. A Larger

number of graphene layers is expected for longer growth time because adlayers are formed simultaneously between the first layers and the Cu surface [105]. At a graphene nucleation site, all adlayers share the same nucleation center and have the same edge termination. In our experiment, the growth time varies from 30 seconds to 30 min, while growth temperature is fixed at 1000 °C, and  $J_{CH_4}:J_{H_2}$  ratio at 1:100. However, when growth time is reduced below 5 min, the graphene film cannot fully cover the Cu substrate (15 mm by 15 mm). Raman spectra in Fig. 4.6 shows the number of graphene layers decreasing significantly based on  $I_G/I_{2D}$  ratio when the growth time decreases from 20 min to 5 min. For a 5-min growth at optimal temperature (1000 °C) and  $J_{CH_4}:J_{H_2}$  ratio (1:100), the  $I_G/I_{2D}$  ratio is less than 1, which suggests the growth of BLG, being achieved for the first time in an open-atmosphere open-environment flame process. Nevertheless, no monolayer graphene growth is observed in the growth time between 30 second and 5 min. An explanation of this result is that a relatively high carbon flux still reaches the substrate, leading to small graphene domain size [4], where the time scale of adlayer growth is on the order of graphene nucleation.

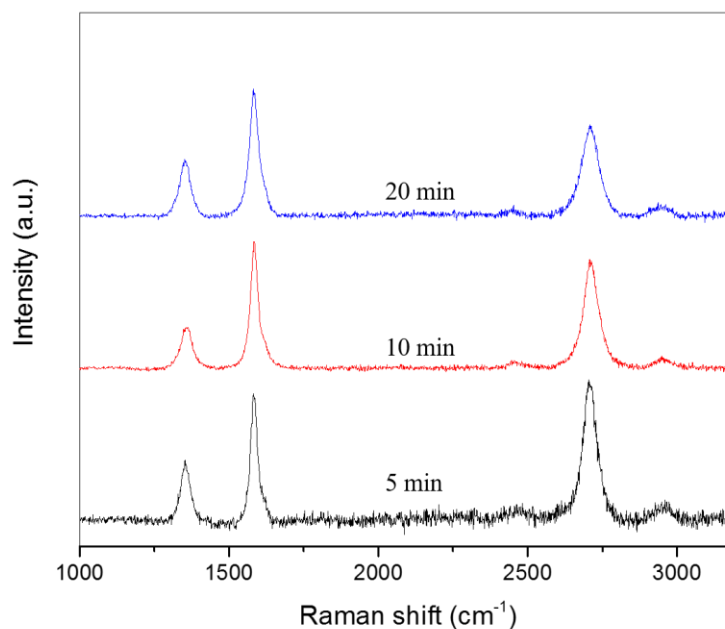


Figure 4.6 Raman spectra of graphene grown on Cu at different growth time. Substrate background signals are all subtracted. The spectra are normalized with the G band.

#### 4.3.4 Effect of Substrate Material

In the gas-phase synthesis of graphene, the growth mechanism strongly depends on substrates materials. The solubility of carbon at high temperature dominates the growth process. Graphene growth on transition metals has been demonstrated in various synthesis methods. However, metal-catalyst-free synthesis of graphene has very limited progress because of the weak adsorption of hydrocarbons on non-metals. Polycrystalline graphene on SiO<sub>2</sub> has been achieved using an oxygen-aided CVD process performed at 1100 °C for 3 to 8 hours [106]. Such technique demonstrates the possibility of directly growing graphene on Si/SiO<sub>2</sub> via CVD, but the graphene film quality is not comparable to

that of conventional CVD. Moreover, this oxygen-aided CVD method is not feasible for graphene manufacturing because of the high energy consumption rate and low production rate.

A number of substrate materials have been studied in this research. Raman spectra of graphene synthesized on nickel (99% Ni, 25  $\mu\text{m}$ ), copper (99.8% Cu, 25  $\mu\text{m}$ ), and ultrapure copper (99.9999% Cu, 0.1 mm and 0.25 mm) substrates undergoing exactly the same experimental process are displayed in Fig.4.7. All metal substrate materials are purchased from Alfa Aesar. Both 0.1-mm and 0.25-mm thick ultrapure copper substrates give identical results, suggesting graphene growth on Cu is a surface process mostly independent of substrate thickness. BLG on ultrapure Cu has noticeably better quality with higher  $I_G/I_{2D}$  ratio and lower D peak intensity. Because of the segregation mechanism, graphene grown on Ni is a uniform few-layer film with fewer defects than that grown on Cu, for our process.

Flame synthesis of graphene on non-metals has been investigated using a Si wafer (381  $\mu\text{m}$  from El-Cat) and a Si/SiO<sub>2</sub> wafer (500  $\mu\text{m}$  with 300 nm oxide layer, from University Wafer). No carbon material was observed on either wafer after 30 min growth time using CH<sub>4</sub> at 1100 °C. Compared with the oxygen-aided CVD process, our flame system running under-ventilated does not provide O<sub>2</sub> species, which can enhance the adsorption of hydrocarbon on SiO<sub>2</sub> [106], [107]. A Si/SiO<sub>2</sub> wafer with graphene film pre-prepared using pulse laser deposition (William Mozet's PLD setup) is put into the flame synthesis setup. Raman spectra before and after flame synthesis using the PLD sample

shows no improvement in  $I_G/I_{2D}$  ratio and a higher D peak, which means more defects or smaller domain size (see Fig. 4.8). The metal-free growth of graphene is still a challenge in our flame synthesis process.

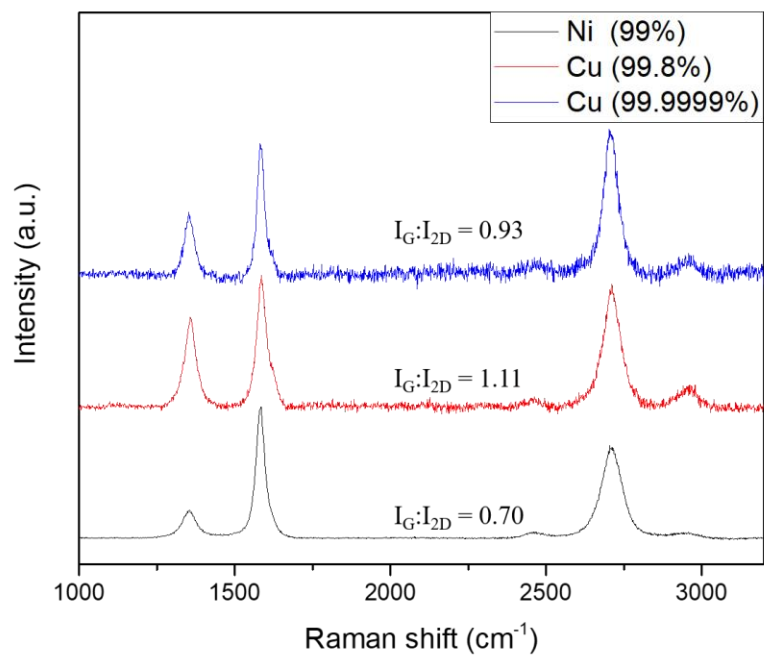


Figure 4.7 Raman spectra of graphene grown on different substrates. Substrate background signals are all subtracted. The spectra are normalized with the G band.

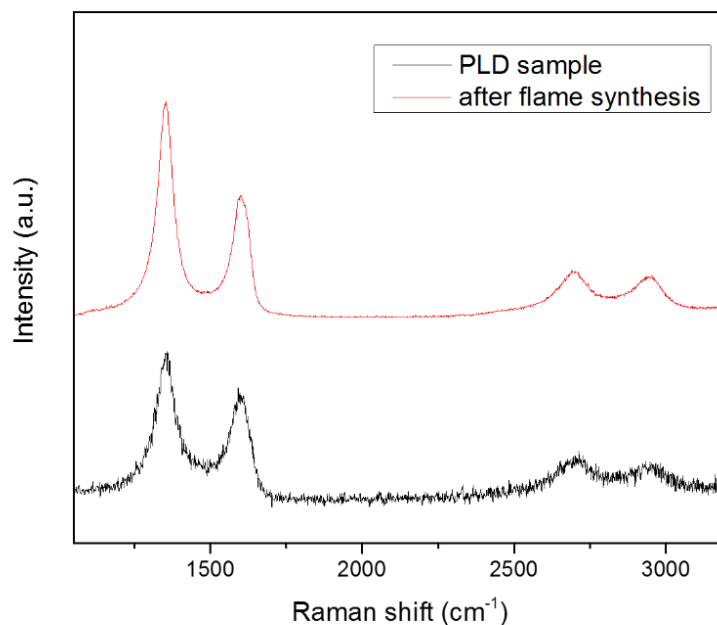


Figure 4.8 Raman spectra of graphene grown on different substrates. Substrate background signals are all subtracted. The spectra are normalized with the G band.

#### 4.3.5 Effect of Hydrocarbon Precursor

Methane ( $\text{CH}_4$ ) is the most used hydrocarbon precursor in the gas-phase synthesis of graphene because of its low pyrolysis rate [108]. However, ethylene ( $\text{C}_2\text{H}_4$ ) and acetylene ( $\text{C}_2\text{H}_2$ ) have also been investigated for growing graphene in CVD [108]–[110]. Wang et al. [111] reported that  $\text{C}_2\text{H}_4$  and  $\text{C}_2\text{H}_2$  have a healing mechanism of divacancy defect in graphene using density functional theory (DFT) calculations. Moreover,  $\text{C}_2\text{H}_4$  has been employed in CVD for reduction of graphene oxide [112] and graphene doping [109]. The effect of  $\text{C}_2\text{H}_4$  and  $\text{C}_2\text{H}_2$  on the flame synthesis of graphene is investigated using the modified m-IDF burner.

Ultrapure Cu is used as a substrate for  $C_2H_4$  and  $C_2H_2$  experiments. In both experiments, the flow rate ratio between carbon precursor and  $H_2$  ( $C/H_2$ ) is maintained at 1:50, which is equivalent to the case  $J_{CH_4}:J_{H_2}=1:100$  with respect to the total amount of carbon input. Raman spectra show BLG in  $C_2H_4$  and  $C_2H_2$  cases for a 5-min growth time at 1000 °C (see Fig 4.9). Such results are identical to a previous  $CH_4$  case under the same growth condition. However, a lower growth rate has been observed in both cases. This result may be because the carbon flux is halved to maintain the same  $C/H_2$  input rate as the  $CH_4$  case. The D peak to G peak ratio for both cases lies in between 0.3 and 0.4, which is similar to that of the  $CH_4$  case. The healing effect of  $C_2H_4$  and  $C_2H_2$  is not observed clearly.

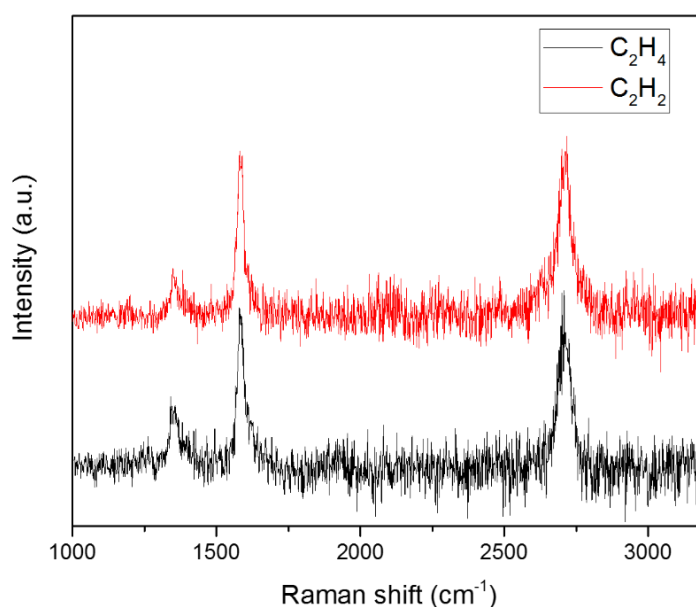


Figure 4.9 Raman spectra of graphene grown on Cu using  $C_2H_4$  and  $C_2H_2$ . Substrate background signals are all subtracted. The spectra are normalized with the G band.



#### 4.3.6 Effect of Flow Field Profile

Flow field profile affects the diffusion of active carbon species from the post-flame gases to the substrate. Uniform graphene with grain sizes up to 10  $\mu\text{m}$  has been grown on Cu foil tilted at an angle against the gaseous flow in a CVD process [113]. Here, substrates are placed in different orientations in order to create different flow field profiles for graphene growth (see Fig. 4.10a). Raman spectra of graphene grown on Cu with perpendicular, tilted (45°), and parallel orientations with respect to the post-flame flow are shown in Fig. 4.10b. The  $I_G/I_{2D}$  ratios are  $\sim 1$ , for all three orientations at optimal growth condition. Perpendicular orientation creates a stagnation flow profile, leading to a result with slightly lower  $I_G/I_{2D}$  ratio than do tilted and parallel orientations. The slight difference in graphene quality can be due to the difference in mass transport of the different boundary layer flows.

To understand better the mass transport in these flow profiles, basic fluid mechanics analysis has been performed. The overall post-flame flow speed ( $u$ ) is 0.276 m/s. The density and kinematic viscosity ( $\nu$ ) of the gas mixture are estimated as 0.3 kg/m<sup>3</sup> and 2.07 cm<sup>2</sup>/s respectively. By assuming the characteristic length  $L_c=1$  cm and the temperature difference  $\Delta T = T_{gas} - T_{substrate}$  is 100K, the Reynolds number (Re) is 13.8 and the Grashof number (Gr) is 21.8. The  $\frac{Gr}{Re^2}$  ratio is 0.11 smaller than 1, which implies that the forced convection is dominant. By performing a scale analysis on the mass, momentum, and energy balance of a vertical plate, three forces are scaled as  $\left(\frac{L_c}{\delta_T}\right)^4 Ra^{-1} Pr^{-1}$  (inertial),

$\left(\frac{L_c}{\delta_T}\right)^4 Ra^{-1}$  (friction), and 1 (buoyancy), where  $\delta_T$  is the thermal boundary layer thickness,  $Pr$  is the Prandtl number, and  $Ra$  is the Rayleigh number that equals to  $(Gr Pr)$ . Since the combustion gas is a low- $Pr$  fluid, the inertia and buoyancy in the thermal boundary layer region is on the same order, which yields,

$$\delta_T \sim L_c(Ra Pr)^{-\frac{1}{4}}, \quad Nu \sim (Ra Pr)^{\frac{1}{4}} \quad (1)$$

where  $Nu$  is the Nusselt number,  $h$  is the convective heat transfer coefficient, and  $k$  is the thermal conductivity. The derivation of Eq. (1) comes from *Convection Heat Transfer* by Adrian Bejan. The correlation between the Nusselt number and thermal boundary layer thickness can be derived as,

$$Nu \sim \frac{L_c}{\delta_T}$$

so the thermal boundary layer thickness is on the order of  $\frac{L_c}{Nu}$ . The average Nusselt number for laminar flow over a flat plate is estimated using

$$Nu = 0.664Re^{1/2}Pr^{1/3} \quad (Pr > 0.6)$$

and equals to 2.47. Therefore, for the parallel orientation, the boundary layer thickness is on the order of  $\sim 4$  mm. For the stagnation flow, the boundary layer thickness is estimated by the Hiemenz solution:

$$\delta \approx 2.4\sqrt{\frac{\nu}{B}}, \quad B = \frac{\alpha u}{L_c}, \quad \text{where } \alpha - \text{constant (assumed 1)}$$

The stagnation flow has a boundary layer thickness  $\sim 6$  mm. With the help from Christopher Stout, a computational fluid dynamics (CFD) simulation has been performed for the stagnation flow case by assuming an argon gas flow at 1250 K (see Fig. 4.11). The velocities start to diverge from one another as the axial position gets down to around 0.01

m (zero is the substrate position), which is the boundary layer thickness. This result confirms the boundary layer thickness for parallel and perpendicular cases are on the same order. The thinner boundary layer can slightly improve flame-synthesized graphene quality by affecting the diffusion of active carbon species by mass transport.

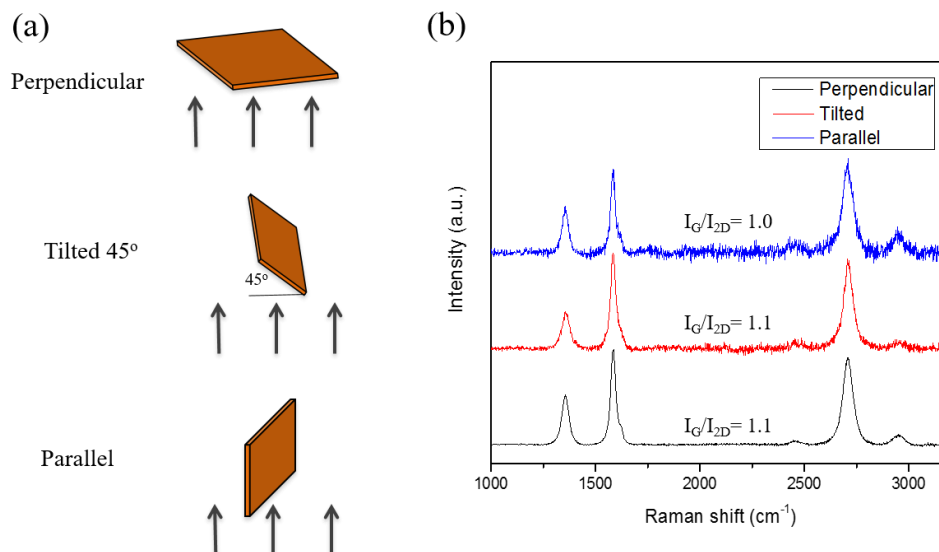


Figure 4.10 a) Schematic of the substrate placed perpendicular, tilted and parallel against the flow. b) Raman spectra of graphene grown on Cu with different orientations. Substrate background signals are all subtracted. The spectra are normalized with the G band.

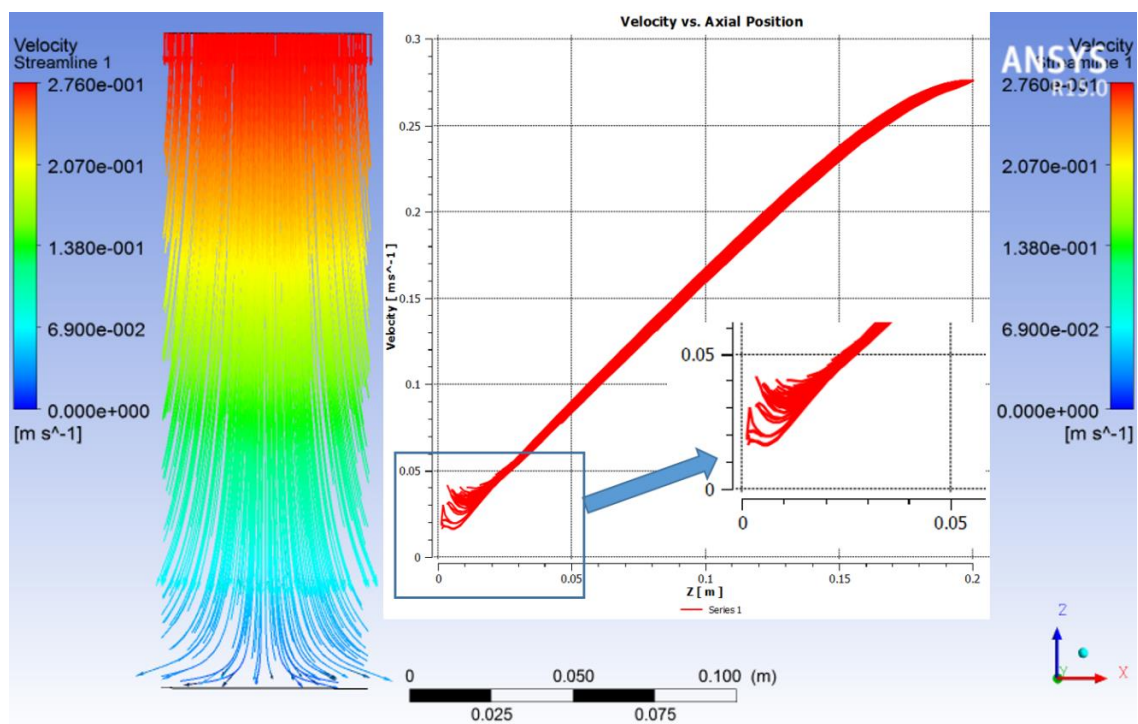


Figure 4.11 Streamline of the velocities in a CFD simulation of stagnation flow. The inset chart shows the velocity versus axial position with a zoom-in around the zero point.

#### 4.3.7 Effect of Transfer Process

Raman spectroscopy is employed on a bilayer graphene (BLG) before and after a transfer to evaluate the transferability of flame-synthesized graphene. Raman spectra show equal  $I_G/I_{2D}$  ratio after transfer (see Fig. 4.12), which means the graphene film is successfully transferred from the Cu to Si/SiO<sub>2</sub> substrate using the wet-chemistry process described in the previous section. The D peak intensity is weaker on Si/SiO<sub>2</sub> substrate than on the original Cu substrate, which implies a reduction in graphene defects induced by copper surface imperfections such as grooves and grain boundaries. The  $I_D/I_G$  ratio on Si/SiO<sub>2</sub> is  $\sim 0.4$ , which agrees with FLG growth using flame synthesis and other methods [4], [13].

The G and 2D bands get sharper and narrower as the full width at half maximum decreases after transfer, which also implies that some copper surface effects are eliminated.

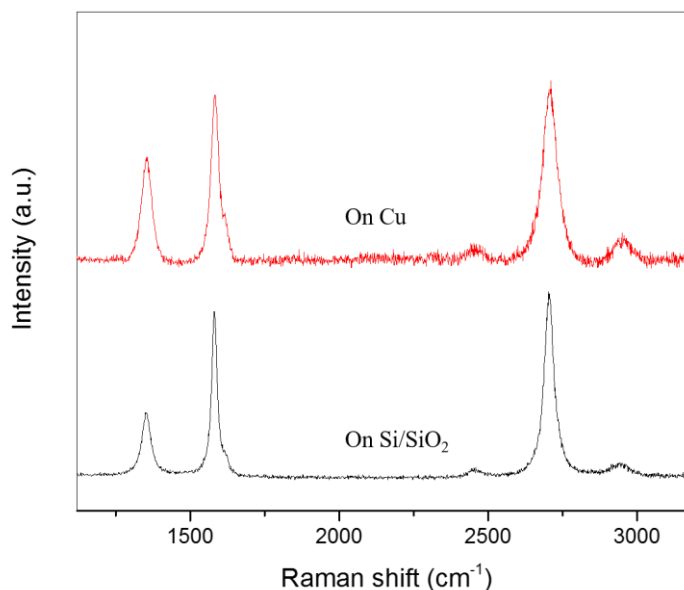


Figure 4.12 Raman spectra of a BLG sample sitting on Cu and Si/SiO<sub>2</sub> before and after the transfer process. Substrate background signals are all subtracted. The spectra are normalized with the G band.

#### 4.3.8 In-situ Raman Spectroscopy of Gas-phase Species Profile

In-situ Raman spectroscopy has been used in characterizing the gas-phase species of the synthesis flow field, as well as monitoring the evolution of the as-formed nanoparticles themselves [114]. Here, on-line laser-based diagnostics are utilized to characterize the precursor species profile along the axial centerline of the flame flow. It is a challenging work to obtain Raman signals from the precursor species with high signal-to-noise ratio because of the low concentrations of all the carbon species in the gaseous flow at high

temperature, and the much weaker Raman signal intensities of gases compared to solids in general. The laser energy is set at 40mJ/pulse to avoid the breakdown on the window. 3000 shots are taken (200 shots on the chip and 15 times by software accumulation) to increase the signal-to-noise ratio.

Raman spectra of gas-phase carbon species along the flow axis between the precursor tube exit and substrate at  $J_{CH_4}:J_{H_2} = 1:100$  and temperature of 1000 °C are plotted in Fig. 4.13(a). There are five distinguishable peaks at  $\sim 1033\text{ cm}^{-1}$ ,  $\sim 1245\text{ cm}^{-1}$ ,  $\sim 1447\text{ cm}^{-1}$ ,  $\sim 1822\text{ cm}^{-1}$  and  $\sim 2909\text{ cm}^{-1}$ . For gas-phase methane, two Raman-active modes lie at  $2914\text{ cm}^{-1}$  and  $3017\text{ cm}^{-1}$ , which match very well with the broad and strong band at  $\sim 2909\text{ cm}^{-1}$  with a small peak split at  $\sim 3009\text{ cm}^{-1}$  observed at the 1 mm height that corresponds to the level just above the exit of the methane precursor tubes. This methane signal decreases sharply as the end of the substrate is approached, suggesting that the concentration of methane drops rapidly because of the spatial diffusion and conversion to other hydrocarbon species at high temperature. Peaks at  $\sim 1447\text{ cm}^{-1}$  and  $\sim 1822\text{ cm}^{-1}$  can be identified as  $C_3H_8$  at  $1451\text{ cm}^{-1}$  and  $C_2$  at  $1832\text{ cm}^{-1}$ , respectively. The peak at  $\sim 1033\text{ cm}^{-1}$  can be from wagging of the  $CH_2$  group which also would give rise to a bending vibration at  $1440\text{ cm}^{-1}$ . The peak at  $\sim 1245\text{ cm}^{-1}$  can be the bending vibrations of CH and OH groups. Peak intensities of hydrocarbon species are nearly constant along the axisymmetric flow axis, suggesting a stable and uniform profile of precursor in the post-flame region.

The measurement results of hydrogen and water vapor are plotted in Figure 4.13 (b). Water vapor band at  $3652\text{ cm}^{-1}$  and hydrogen band around  $4160\text{ cm}^{-1}$  have steady intensities which imply that the concentration of water vapor and hydrogen are independent of position. The concentration of methane reduces to the lowest level near the substrate from decomposition in the high-temperature gaseous flow. Therefore, the main source of active carbon to promote the graphene growth can be a series of hydrocarbons, including  $\text{CH}_4$ ,  $\text{C}_3\text{H}_8$ ,  $\text{C}_2$ , and  $\text{CH}_2$ . More work is needed to understand the mechanism of graphene growth in the flame synthesis process.

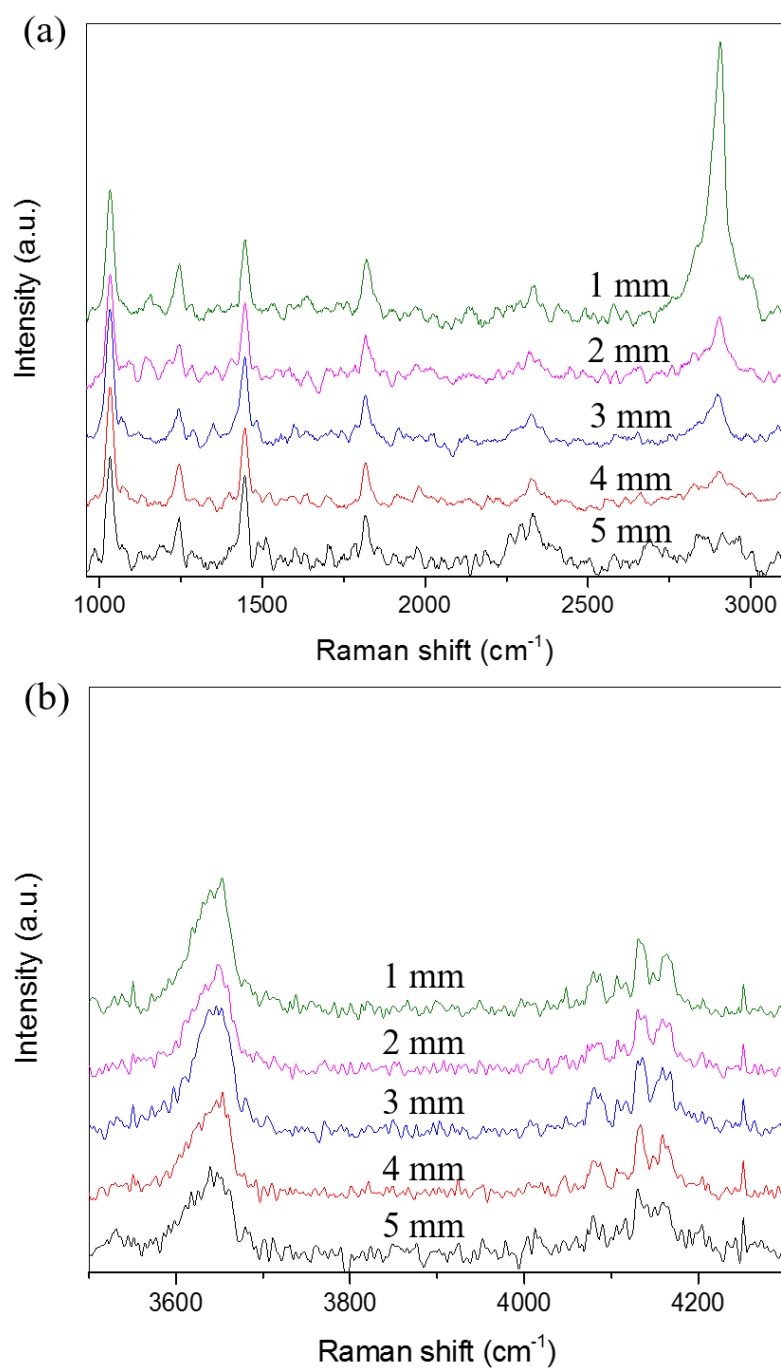


Figure 4.13 In-situ Raman signals of hydrocarbon species (a) as well as hydrogen and water vapor (b) evolved along the flow axis from the exits of precursor tubes to substrate. The position 0 mm corresponds to the exits of precursor tubes, while 5 mm corresponds to the lower edge of the substrate.



#### 4.4 Concluding Remarks

By employing the modified multi-element inverse-diffusion flames setup, the influence of various parameters, including substrate material, precursor, temperature, and growth time on graphene synthesis is demonstrated in this chapter. Under optimized condition, the synthesis of bi-layer graphene is reported for the first time using an open-atmosphere flame synthesis method. The transition growth from few-layer graphene to bilayer is observed by varying substrate temperature and methane-to-hydrogen flow rate ratio. Graphene films are grown on different substrates. Bilayer graphene films exhibit different levels of defect on Cu substrates with different purities. The higher the Cu purity; the fewer defects or disorders are induced by the substrate. Because of a different growth mechanism, Ni substrate gives thicker graphene growth (few-layer), but with fewer defects. The effects from different precursors and flow field are examined. Moreover, an in-situ Raman spectroscopy measurement is performed on the experimental setup to understand the evolution of carbon species in the flame flow. The dominant carbon species observed near the substrate are  $\text{CH}_4$ ,  $\text{C}_3\text{H}_8$ ,  $\text{C}_2$ , and  $\text{CH}_2$ , which can be the main carbon species transported to the substrate promoting graphene growth. Flame-synthesized graphene can be transferred onto arbitrary substrates for applications. Therefore, such method is capable of continuously producing bi- and few-layer graphene over large areas, for example by rasterizing, in an open-atmosphere environment. Compared with conventional CVD, flame synthesis also has advantages in processing time and cost.

## Chapter 5

### 5. Hydrogen-Post-Treated Flame Synthesis of Monolayer Graphene in Open- Atmosphere

#### 5.1 Introduction

The breakdown of the self-limiting mechanism makes it difficult to deposit monolayer graphene (MLG) on Cu at atmospheric pressure. However, by reducing the methane concentration in the gas mixture, MLG has been achieved in APCVD [13]. Li et al. [55] studied the effect of methane flow rate and methane partial pressure on graphene growth rate and domain size. Lower flow rate and partial pressure of methane lead to lower growth rate and less nucleation density of graphene, which are essential for the growth of large-crystal monolayer films. Graphene crystals grown from different nucleation sites with different orientations can only coalesce into polycrystalline films [115]. In flame synthesis, the total flow rate and carbon flux are much higher than that in APCVD and LPCVD, in order to stabilize the flames, which can lead to smaller graphene domains and adlayers. That is why few-layer graphene (FLG) grown in open-atmosphere flame synthesis exhibits a higher D-peak to G-peak ratio ( $I_D/I_G$ ) ratio and sheet resistance than that for CVD-grown graphene [4]. Moreover, the activation energy of graphene

nucleation in atmospheric pressure (9 eV) is substantially higher than that in low pressure (4 eV) [116].

In the previous chapter, various parameters have been studied for flame synthesis of graphene. After optimization of synthesis conditions, including substrate material, temperature, flow rate, and growth time, bilayer graphene (BLG) was produced for the first time using our open-atmosphere flame synthesis method. However, by further lowering methane concentration to the condition of APCVD, MLG was not observed for the cases examined. The high flow flux and large numbers of combustion products (e.g.,  $\text{H}_2\text{O}$ ,  $\text{OH}$ ,  $\text{CO}$ ,  $\text{CO}_2$ ) seem to make it difficult to directly translate conditions for CVD to that for flame synthesis.

Hydrogen has been reported to play a vital role in graphene growth as an activator of surface-bound carbon and an etching reagent for the “weak” carbon-carbon bonds that controls the graphene domains [117]. Ivan Vlassiouk et al. [117] also verified that the minimum temperature for effective hydrogen etching is 850 °C. For the flame synthesis of graphene, the role of hydrogen has been mainly investigated for the substrate pretreatment stage and the growth stage [99]. Yagang Yao et al. [118] performed a post-growth hydrogen thermal etching on APCVD-synthesized graphene at 1000 °C for 1.5 min to obtain MLG. Moreover, a high-temperature thermal annealing process was found to be effective for curing the defects in graphene, calling it a “self-healing” mechanism [119]. Thus, in this work, hydrogen annealing is employed to improve the quality of flame-synthesized graphene.

## 5.2 Experiment

The synthesis setup used in this work is a modified multi-element inverse-diffusion flames (m-IDFs) burner. The experimental process consists of two operations during a single experiment using the same modified m-IDFs burner: 1) flame synthesis of graphene, 2) hydrogen annealing of flame-synthesized graphene (see Fig 5.1). Hydrogen annealing is performed on flame-synthesized BLG on Cu. Prior to synthesis, the Cu substrate is reduced in the hydrogen environment at 1000 °C for 10 min, using the modified m-IDFs burner running only hydrogen as fuel with no flow through the precursor tubes, to remove any oxide layer and enlarge the grain size. Then methane is introduced into post-flame gases via the precursor delivery tubes to initiate graphene growth on Cu. The growth temperature is maintained at 1000 °C, and the input ratio between CH<sub>4</sub> and H<sub>2</sub> is 1:100, where hydrogen serves as the fuel emanating from the base of the modified m-IDFs burner. After 5-min growth, methane supply through the precursor tubes is turned off, but hydrogen continues to flow sustaining the m-IDFs at the base of the burner. As such, the substrate experiences annealing in a hydrogen (and argon inert) environment at 1000 °C for 10 min. After annealing in the hydrogen-rich environment produced by the underventilated multiple flames at the base of the burner, the m-IDFs are extinguished simply by shutting down the oxidizer flow. Finally, the substrate is cooled down to room temperature with a continuous flux of inert argon gases.

As-synthesized graphene is characterized by Raman spectroscopy (Renishaw 1000, 514 nm laser wavelength, 50 $\times$  magnitude). Transmission electron microscopy (TEM, JOEL 2010F, 200kV) is employed to study the crystal structure and morphology of graphene samples. TEM sample is prepared by transferring graphene to a lacey TEM grid by following the wet-chemistry process described in the previous chapter. Atomic-force microscopy (Dimension FastScan, Bruker Nano) with probes (Fastscan A, 5 nm tip radius) is used for tapping mode scanning and imaging of the graphene samples on Si/SiO<sub>2</sub>.

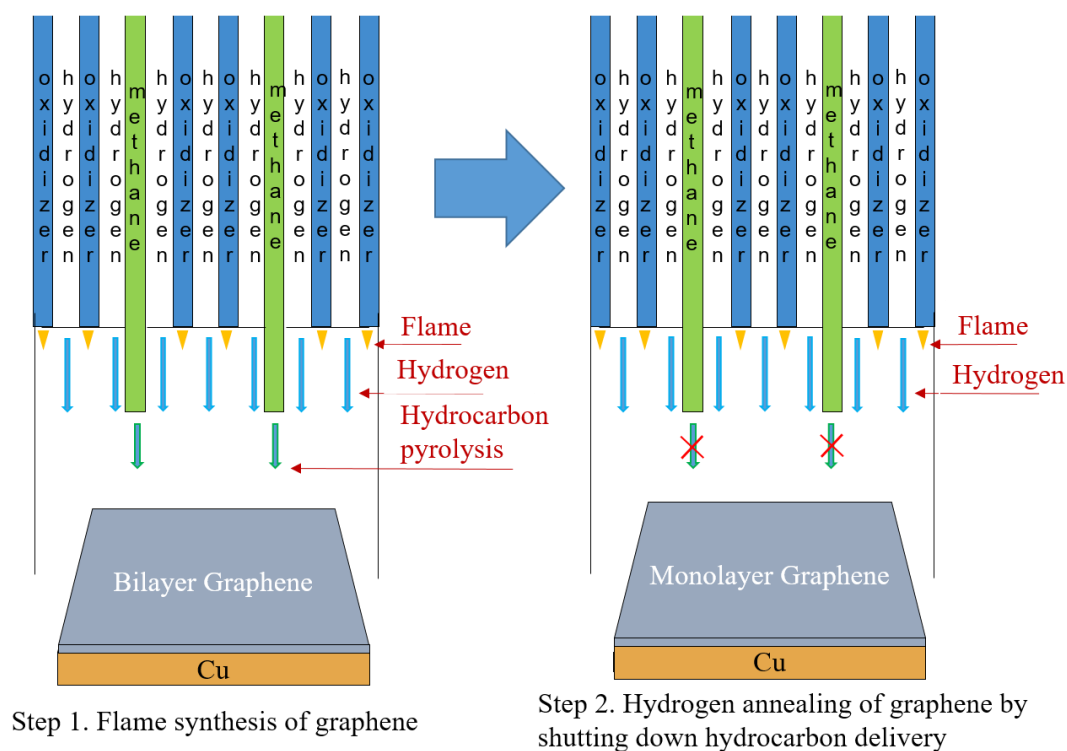


Figure 5.1 Schematic of two-step flame synthesis of monolayer graphene using modified m-IDF setup.

### 5.3 Results and Discussion

Typical Raman spectra of graphene sample before and after hydrogen annealing are shown in Fig. 5.2a. For a 10-min post-growth treatment at 1000 °C, the overall  $I_G/I_{2D}$  ratio is significantly reduced from  $\sim 1$  to  $\sim 0.5$ , which means a BLG is tailored to a MLG. This result demonstrates that hydrogen plays a vital role in reducing the number of graphene layers by effectively etching additional layers and growth fronts through hydrogen's interactions with "weak" carbon-carbon bonds and dangling bonds. The D-peak to G-peak intensity ( $I_D/I_G$ ) ratio is nearly constant before and after annealing. The "self-healing effect" has not been observed in this case. J Chen et al. [119] observed the self-healing of defective graphene with nano-scale vacancies induced by an argon plasma when thermal annealing samples in an argon atmosphere. The curing of the vacancies can be due to the mobility and rearrangement of carbon atoms on the Cu surface at high temperature. There are two possible reasons why the D peak intensity is not reduced after hydrogen annealing. First, the D peak in flame-synthesized graphene is mainly due to the submicron domain size [4]. Since the  $I_D/I_G$  ratio is inversely proportional to the domain size of graphene [120], [121], the ratio should stay the same if the domain size is unchanged. Second, the "self-healing" effect is offset by the hydrogen etching effect. Based on the Raman spectra, the inference may be drawn that by using hydrogen annealing, the adlayer graphene can be effectively etched away without introducing new defects or reducing domain size in flame-synthesized graphene.

Typical Raman spectra of flame-synthesized MLG features a D peak located at  $1346\text{ cm}^{-1}$ , a G peak at  $1585\text{ cm}^{-1}$ , and a 2D peak centered at  $2695\text{ cm}^{-1}$  (see Fig. 5.2b). All peaks can be fitted by the Lorentzian profile. The symmetric 2D peak has a narrow full width at half maximum (FWHM) of  $\sim 35\text{ cm}^{-1}$ . For high-quality MLG synthesized in CVD, the  $I_G/I_{2D}$  ratio is reported in the range from  $\sim 0.4$  to  $\sim 0.5$ , and the FWHM of the 2D peak is between  $30$  and  $40\text{ cm}^{-1}$  [58], [122]. The presence of a defect-induced D peak suggests the existence of subdomain boundaries and multi-layer graphene formation [103], [122]. The  $I_D/I_G$  ratio is usually lower than  $0.05$  for CVD-synthesized graphene. However, Reina et al. [4] reported the  $I_D/I_G$  ratio of large-area FLG to be between  $0.05$  and  $0.3$ . Our flame-synthesized graphene exhibits a  $I_D/I_G$  ratio of  $0.4$  agreeing with the previous work. From the enlarged TEM image, the hexagonal arrangement of carbon atoms in graphene can be observed (see Fig. 5.3a). The selected area electron diffraction (SAED) pattern indicates that the MLG is not a perfect single crystal and probably has adlayers. The TEM images at different resolutions show a polycrystalline graphene film with clear grain boundaries (see Fig. 5.3a, b). Considering both the Raman spectra and TEM results, the MLG sample possesses additional layers, submicron domains, and other types of defects like vacancies and nanopores. AFM image of MLG on Si/SiO<sub>2</sub> confirms the uniformity of the film at the micrometer scale. The highlighted spots in the image are the residues stuck in the film during the wet-chemistry transfer process. A depth-profile scanning has been performed at different edges, but there is no conclusive result for the film thickness. The theoretic thickness of MLG is  $\sim 0.34\text{ nm}$ , but the surface roughness

of Si/SiO<sub>2</sub> is measured to be ~1 nm, which creates significant variance in the thickness measurement.

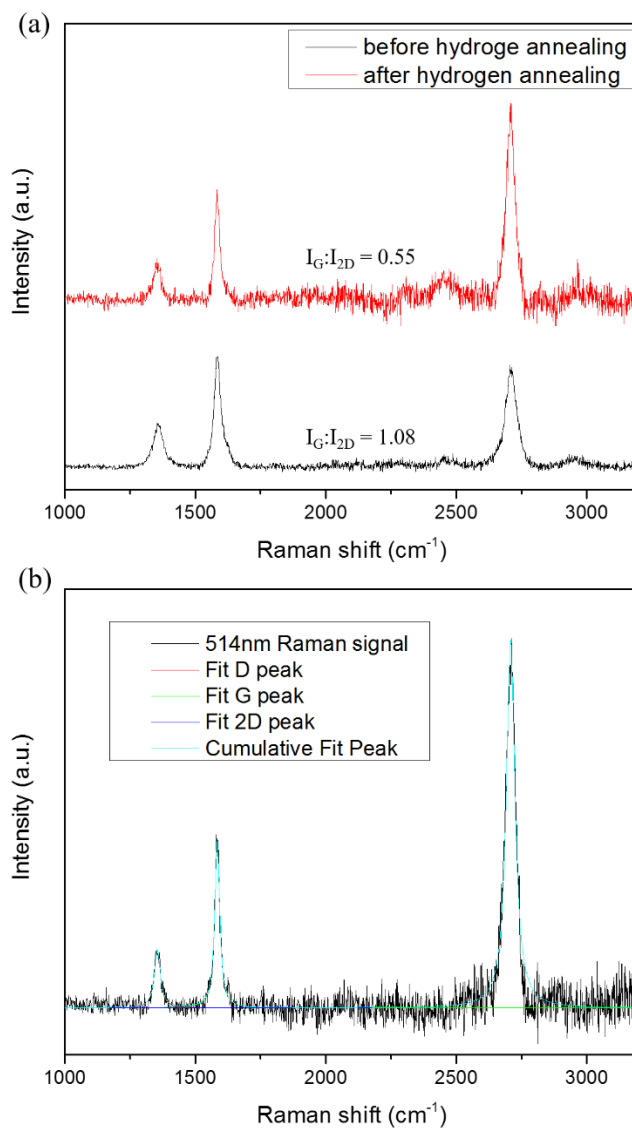


Figure 5.2 a) Typical Raman spectra of graphene sample before and after post-growth hydrogen annealing treatment. b) Single Lorentzian fitting of a Raman spectra from monolayer graphene sample. Substrate background signals are subtracted. The spectra are normalized with the G band.



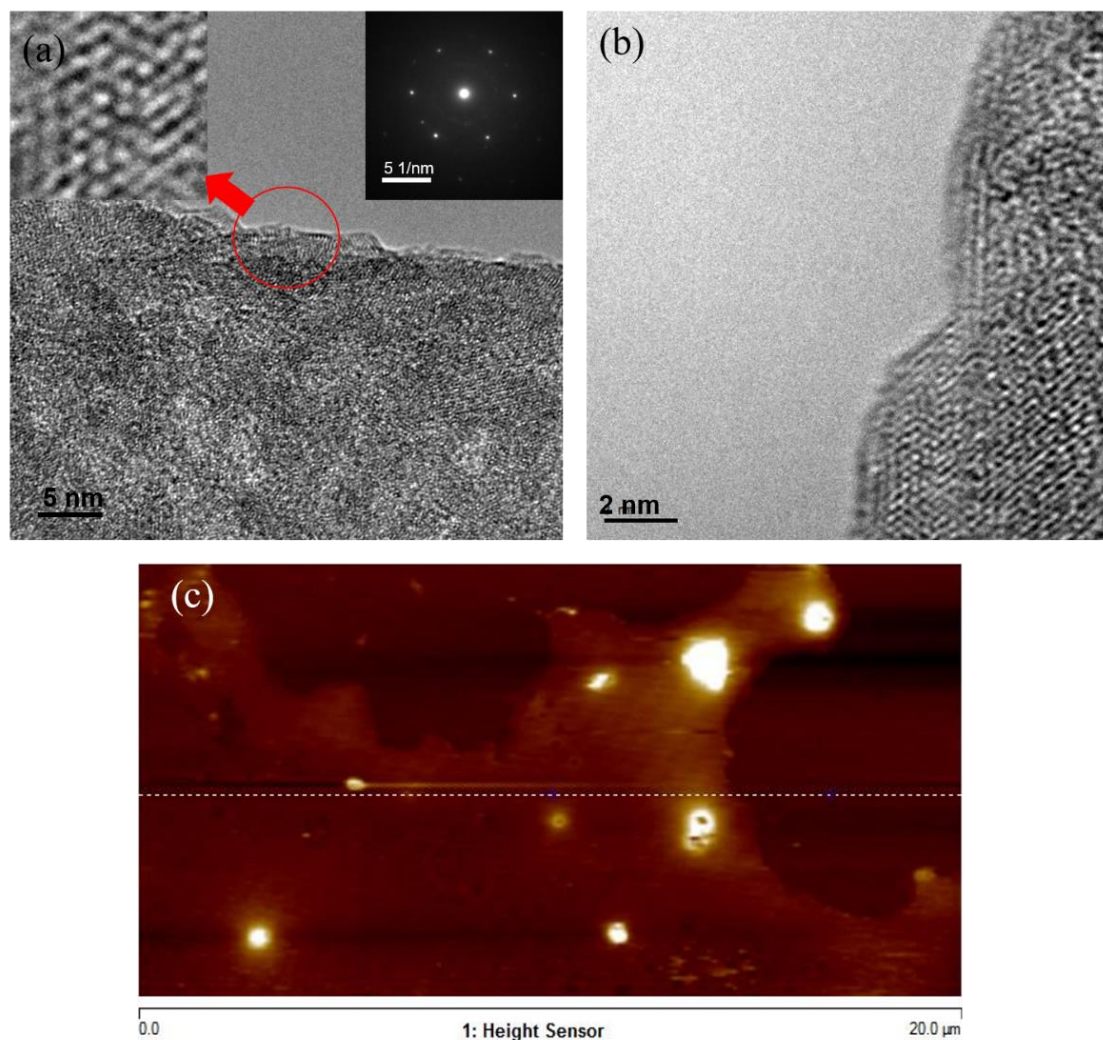


Figure 5.3 TEM images of monolayer graphene with different resolutions (a) (b). The top right inset shows the SAED pattern, and the top left inset shows magnified image of the hexagonal lattice in the circled edge (a). AFM image of monolayer graphene with highlight spots of residuals from transfer process (c).

Single-crystal MLG displays remarkable electro mobility at room temperature. However, the absence of a bandgap in perfect MLG prevents it from semiconductor applications. A tunable bandgap has been observed in BLG, and the gap can be tuned by an external electrostatic potential [41], [63], [64], [123]. Graphene defects such as

vacancies and heteroatoms can open up a bandgap in MLG [65], [124], [125]. Flame-synthesized MLG naturally exhibits a higher defective level, implying the existence of a small-percentage of BLG, vacancies, nano-scaled pores, and submicron domains. These imperfections may possibly induce a bandgap in flame-synthesized MLG for various applications.

#### 5.4 Concluding Remarks

A hydrogen etching effect on flame-synthesized graphene is discovered during a post-graphene-growth hydrogen annealing process. With this process, high-quality (meaning minimal defects) bilayer graphene can be tailored towards monolayer graphene (MLG). Such technique enables the synthesis of MLG using open-atmosphere flame synthesis for the first time. The production of MLG at atmospheric pressure is considered a challenge because the “self-limiting” mechanism of Cu no longer holds at elevated pressure. Even though MLG has been achieved in atmospheric-pressure (confined) CVD by carefully controlling the partial pressure and flow rate of the precursor, it is still very challenging to grow MLG using any gas-phase synthesis method in an *open unconfined* environment.

Hydrogen atoms are found to be effective etching agents for weak carbon bonds and dangling bonds in adlayers of graphene. Such etching process does not damage the fine crystals of graphene, and no obvious shrinkage in graphene domain size is observed based on Raman spectra. Unlike CVD processes, this method is unconfined and more

suitable for the continuous large-scale production of MLG over large surfaces at reduced costs.

## Chapter 6

### 6. Effect of Hydrogen Annealing on Flame-Synthesized Graphene and Direct Synthesis of Highly Defective Graphene

#### 6.1 Introduction

Graphene's defects can be categorized based on the scale. Atomic-scale defects include vacancy-type defects (reconstructed point defects), hetero-atoms and Stone-Wales defects. The vacancy-type defects can be created by electron irradiation in graphene, where foreign species can be trapped [124]. By purposefully introducing such defects, it is possible to open up a bandgap in graphene for semiconductors. Submicron-scale defects in graphene such as pores and grain boundaries afford many potential applications in membranes and sensors.

Nanoporous graphene (NPG) has been extensively studied in recent years. Through the formation of nano-scale pores in a large area graphene sheet, it is possible to open an energy band gap for application in field effect transistors (FETs) [125]. Creating pores within graphene can also increase the amount of edges that act as adsorbing sites for gas molecules sensing. Moreover, NPG can be fabricated to be effective separation membranes for ion selection and water desalination [29]. Various methods have been employed to create nano-scale pores in graphene films, including focused electron beam

irradiation, nanoimprint lithography, photocatalytic oxidation, and catalytic hydrogenation [125]. For the fabrication of ion-selective graphene membranes, pristine graphene can be exposed to ion bombardment and oxidative etching (see Fig. 6.1a). The pore size can then be tuned by controlling the exposure time (see Fig. 6.1b). Raman spectra are used to measure the defects. The  $I_D/I_G$  ratio can conveniently indicate the defective level in the graphene film. However, Raman spectra cannot provide comprehensive information about what types of defects exist. Further TEM analysis is then needed. For a graphene sample with  $I_D/I_G$  ratio  $\sim 1$ , the pore density is on the order of 1 pore/100 nm<sup>2</sup> (see Fig. 6.2).

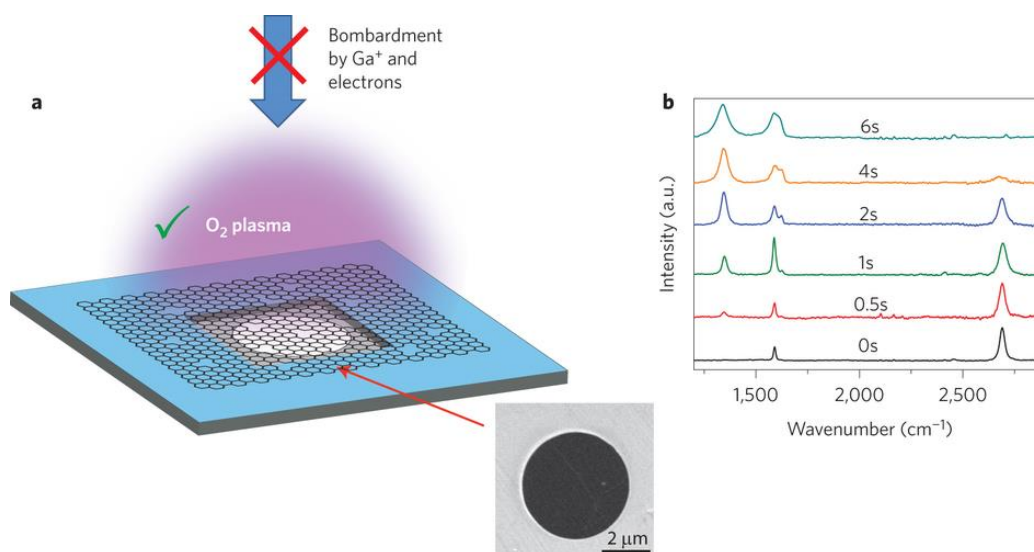


Figure 6.1 Schematic and SEM image of single-layer graphene suspended on a 5-μm-diameter hole. For nanoporous graphene fabrication, several approaches have been utilized: bombardment by ions, by electrons and via O<sub>2</sub> plasma treatment. b, Raman spectra (514 nm excitation) of suspended graphene after different exposure times to oxygen plasma (reproduced with caption form [29]).

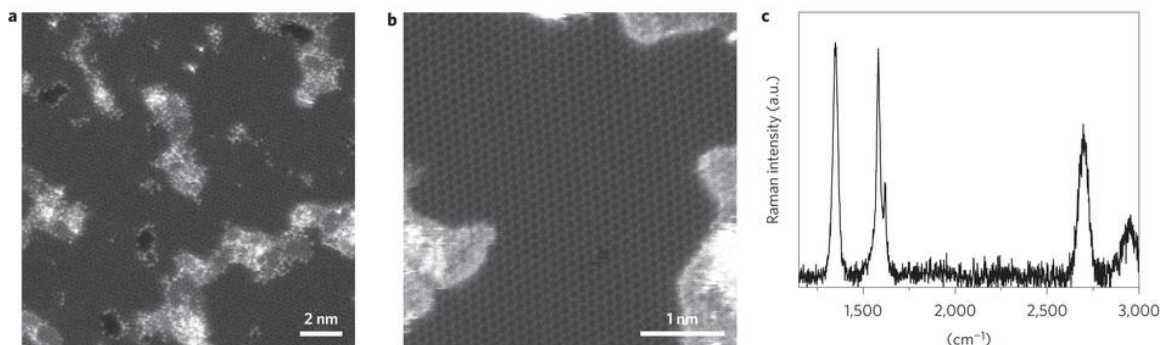


Figure 6.2 a, b, Aberration-corrected STEM images of graphene after 1.5 s exposure to oxygen plasma. Pores with characteristic dimensions of  $\sim 1$  nm are clearly seen. c, Raman spectra of graphene sample used for STEM imaging in a, b, which shows  $I_D/I_G \approx 1$  (reproduced with caption form [29]).

In general, the current technique for creating defects (e.g., vacancies, pores) in graphene is by damaging CVD-grown graphene films using electron or ion beam, which requires an additional setup for graphene modification after synthesis. A direct synthesis method for defective graphene would be favorable for many applications. In the previous chapter, the etching effect of hydrogen annealing was demonstrated, being able to tailor the number of graphene layers down to 2 or 1. In this chapter, the influence of hydrogen annealing on graphene samples with different original conditions and substrate materials are studied using our modified multi-element inverse-diffusion flame setup. A direct synthesis method to produce highly-defective graphene is demonstrated. Furthermore, properties of as-synthesized highly-defective graphene are investigated.

## 6.2 Experiment

Hydrogen annealing is examined on substrates including commercial Ni and Cu foils (Alfa Aesar), ultrasmooth Cu provided by Army Research Laboratory, and Si/SiO<sub>2</sub> wafer (University Wafer). Ultrasmooth Cu substrate is electropolished on the desired area with the rest of the Cu surface roughness similar to commercial Cu [126]. Such electropolishing process can reduce the Cu (Alfa Aesar, 25  $\mu\text{m}$ , 99.8%) surface roughness by over 90%. Griep et al. [126] reported an enhancement in graphene mechanical properties by using ultrasmooth Cu as a substrate in CVD. Graphene films are synthesized on metal substrates using our modified m-IDF setup, but graphene samples on Si/SiO<sub>2</sub> wafers are prepared by two other approaches. One is using PLD to put graphene on Si/SiO<sub>2</sub>, prepared by William Mozet [127]. The PLD system uses a Nd-YAG Q-switched laser (532 nm and 266 nm) as the energy source and pyrolytic graphite as a target to deposit FLG on Si/SiO<sub>2</sub> at 900 °C in a high vacuum chamber ( $10^{-6}$  torr). Another approach is transferring flame-synthesized graphene from Cu to Si/SiO<sub>2</sub> using the wet-chemistry method mentioned in previous chapters. Hydrogen annealing temperature is maintained at 1000 °C for all cases.

Raman spectroscopy (Renishaw 1000, 514 nm laser wavelength, 50 $\times$  magnitude) is employed as the main tool to characterize the quality change of graphene before and after hydrogen annealing. The  $I_G/I_{2D}$  ratio is used to identify the change in the number of layers of graphene. The  $I_D/I_G$  ratio gives a qualitative indication of graphene domain size and number of defects. Room temperature Scanning/Transmission Electron Microscope

(FEI Talos F200X S/TEM, 200 kV) is used to investigate the morphology of the nanoscale defects within defective graphene films. UV-Vis Spectroscopy measurements and band gap analysis are conducted by Daryll Munoz and Ashley Pennington from Celik Catalysis Laboratory, Rutgers CBE. To analyze the band gap energy (BGE) of the defective graphene, the samples supported on a given substrate are loaded into an Evolution 300 UV-Vis Spectrometer (ThermoFisher) equipped with a Praying Mantis Diffuse Reflectance Accessory (Harrick Scientific) to measure the absolute diffuse reflectance ( $R_\infty$ ), with a Spectralon® disk as a reference. The sample beam is diffusely reflected off the sample, and the beam size is roughly 1 mm<sup>2</sup>. The absolute reflectance measured in the range from 190 nm to 1100 nm is converted to Kubelka Munk units,  $F(R_\infty) = KMU = \frac{(1-R_\infty)^2}{2R_\infty}$ , which is analogous to absorbance for diffusely reflected samples. After measuring diffuse reflectance, the BGE of the samples is calculated through derivative peak fitting (DPR). Fityk software [128] is used to analyze the first derivatives of the absolute reflectance with respect to wavelength. Each differential diffuse reflectance function is fit with Gaussian peaks, where each peak represents an independent BGE. The centers of each peak present in the differential plot correspond to potential band gap energies of the sample.

To assess the applicability of high-defective graphene for use as filters, highly-defective graphene samples are fabricated into membranes for ion selection property measurements. After hydrogen annealing, flame-synthesized graphene is transferred to a pinhole substrate and suspended on the hole using the wet-chemistry method (see Fig 6.3a).



Pinhole substrates used here are standard precision 5- $\mu\text{m}$  round apertures purchased from National Aperture. The permeability and conductance of defective graphene membranes are measured with the help from Semih Cetindag from Prof. Shan Group, Rutgers MAE. For the conductance measurements, an electrochemical workstation using two Ag/AgCl electrodes (0.8 in diameter and 8 mm in length) and potassium chloride aqueous solution (1 Mole/L KCl) is employed (see Fig. 6.3b). Defective graphene membranes are attached to plastic holders with an inner diameter of 5 mm and sealed with non-reactive epoxy for experimentation (see top-right inset of Fig. 6.3b). The methodology used in the measurements is to apply voltages and record the corresponding current values using a 3 electrode configuration (WE, CE and RE). The conductance of the tested membrane is calculated based on the I-V curve.

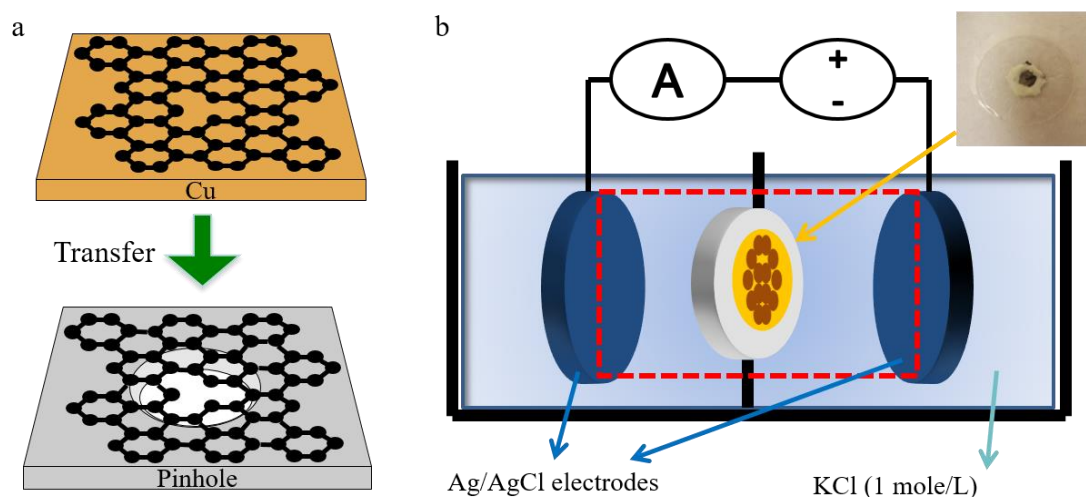


Figure 6.3 a) Schematic of transferring defective graphene from Cu to pinhole substrate. b) Schematic of an electrochemical workstation for conductance measurements of defective graphene membranes. The top-right inset of (b) is a photo of the testing membrane.

### 6.3 Results and Discussion

In order to understand the mechanism of hydrogen annealing, graphene samples on different substrate materials are first investigated. The etching effect of hydrogen annealing makes it possible to create defects in graphene film directly and tailor properties. Thus, hydrogen annealing conditions are varied to induce graphene defects. The structure and property of the as-grown defective graphene are characterized. Lastly, the potential applications of highly-defective graphene are explored.

#### 6.3.1 Effect of Hydrogen Annealing on Graphene with Different Substrates

How hydrogen annealing affects the quality of graphene prepared on different substrates is investigated in this work. Flame synthesis of FLG on nickel substrate is produced at a wide range of temperature from 850 °C to 1000 °C, consistent with previous studies. A typical Raman spectrum of FLG grown on 25  $\mu\text{m}$  thick Ni foil is shown in Fig. 6.4a. Unlike graphene grown on Cu, graphene quality on Ni is not affected much by the  $J_{\text{CH}_4}:J_{\text{H}_2}$  ratio or temperature. Graphene growth on Ni is subject to a segregation mechanism because of the higher carbon solubility in Ni than in Cu. After post-growth hydrogen annealing, flame-synthesized FLG is fully etched away on Ni. There are two possible mechanisms that can explain this phenomenon. One is similar to hydrogen annealing on Cu such that hydrogen can etch away weak carbon bonds at edges and growth fronts. If that is the case, Ni should have a better catalytic performance assisting hydrogen etching than does Cu because the general defective level of graphene is lower on Ni. Another

possibility is the carbon dissolution-precipitation mechanism where carbon atoms dissolve back into Ni, with precipitation of nickel carbides (NiC) occurring simultaneously [129]. Leong et al. [129] have verified that the dissolution of carbon requires imperfection sites like defects and dangling bonds in graphene. In our case, the result can be a combination of both effects, perhaps explaining why a controllable improvement in the number of graphene layers has not been observed on Ni substrates after hydrogen annealing.

Typical Raman spectrum of PLD-grown FLG (provided by William Mozet) exhibits a large  $I_D/I_G$  ratio and low  $I_G/I_{2D}$  ratio (see 6.4b). The presence of the 2D peak indicates the existence of graphene or graphitic structure. However, such spectrum also suggests the film consists of amorphous carbon and small domain graphene with defects because of the large  $I_D/I_G$  ratio and slight merging of D and G peaks. After hydrogen annealing, this highly defective FLG is etched away with no carbon signals detected by Raman spectroscopy. It has been demonstrated that at high temperature, hydrogen can react with carbon dangling bonds and effectively etch away adlayers of graphene without noticeable damage to the film. The removal of PLD-grown graphene on Si/SiO<sub>2</sub> reveals that hydrogen etching is not only effective on adlayers but also dangling bonds at edges and defects. If the defects of the graphene film reach to a certain level, then hydrogen annealing can affect the film by inducing even more defects.

To verify that the wipeout phenomenon is not due to the use of a nonmetal substrate, typical flame-synthesized BLG ( $I_D/I_G/I_{2D} \sim 0.4:1:1$ ) films are transferred from Cu to Si/SiO<sub>2</sub> for subsequent hydrogen annealing experiments. Interestingly, the BLG film is

retained without clear improvement or reduction in quality after hydrogen annealing. No observational change in  $I_G/I_{2D}$  ratio indicates that the hydrogen annealing converting BLG to MLG on Cu reported in the previous chapter is likely a metal-substrate-assisted process, which seems to agree with the results in the literature [118]. The BLG film is not observed with any noticeable damage after annealing, meaning that such flame-synthesized graphene does not contain considerable amounts of defect sites like PLD-grown graphene does to initiate the wipeout process. Therefore, hydrogen annealing can improve graphene quality on Cu, by etching away adlayers through a metal-assisted mechanism, but it can also wipe out graphene films that containing vast amounts of defects. Thus, the interaction mechanisms among hydrogen, graphene, and substrate materials at high temperature can be complicated.

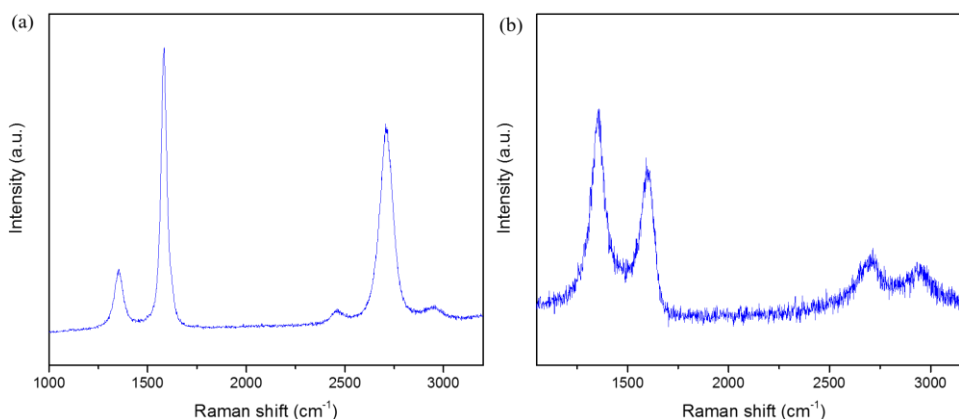


Figure 6.4 (a) Typical Raman spectra of few-layer graphene grown on nickel at 1000 °C. (b) Raman spectra of few-layer graphene on Si/SiO<sub>2</sub> using Pulse Laser Deposition at 900 °C in vacuum (provided by William Mozet). Substrate background signals are subtracted. The spectra are normalized with the G band.

### 6.3.2 Direct Synthesis of Highly Defective Graphene

The strong etching effect of hydrogen annealing on low-quality graphene (high  $I_D/I_G$  ratio) suggests that direct synthesis of highly-defective graphene with tunable defects may be possible by controlling the raw (starting) graphene quality and annealing conditions. To examine this potential, graphene with high  $I_D/I_G$  ratio ( $>0.4$ ) is first *intentionally* synthesized with our m-IDFs burner. Although a key motivation of this thesis is to develop a viable flame method for fabricating high-quality graphene (mono- and bi-layer graphene with minimum defects), the work in this chapter goes the opposite direction and pursues the synthesis of highly-defective graphene. In Chapter 4, a parametric study on graphene growth conditions was performed to optimize parameters to obtain BLG growth, which was achieved for the first time using open-atmosphere flame synthesis. In Chapter 5, flame-based fabrication of MLG was demonstrated by adding a post-growth hydrogen etching step. Here, we explore how to create more defects in graphene, which holds great potential for many applications, such as gas separation and water desalination, via a controllable flame method.

For a typical graphene sample (mono-, bi- or few-layer) synthesized in our flame system, the  $I_D/I_G$  ratio is  $\sim 0.4$ , which agrees with previous flame synthesis results [4]. In the previous section, it was confirmed that hydrogen annealing does not observably damage flame-synthesized graphene with an  $I_D/I_G$  ratio of  $\sim 0.4$ . The reason is that the D peak in flame-synthesized graphene is mainly caused by submicron domain boundaries, not structural defects like vacancies. The formation of the grain boundary is due to the

termination of graphene growth when two neighboring grains meet. Compared with conventional CVD processes, flame synthesis utilizes much higher flow fluxes so that the flames can be stabilized, which results in more prolific nucleation of carbon atoms, with a higher density of nucleation sites, on the substrate surface. Graphene grown from domains with different orientations normally do not merge to a single larger crystal, instead generating a polycrystalline film. The  $I_D/I_G$  ratio of flame-synthesized graphene indicates the small grain size where the grain boundaries create defective sites. The adlayers of graphene at growth fronts contains more edges and dangling bonds that can be effectively etched away in hydrogen annealing, which, viewed in another way, enables the tailoring of the number of graphene layers.

From our study in Chapter 4, two parameters can significantly increase  $I_D/I_G$  ratio in graphene: substrate temperature and materials. By lowering substrate temperature, the number of disorder increases in graphene crystals, and amorphous carbon growth occurs. Of course, amorphous carbon is not desired in this work since graphene structure needs to be maintained for many applications. By switching substrate from ultrapure Cu (99.9999%) to Cu (99.8%), the  $I_D/I_G$  ratio increase from  $\sim 0.4$  to  $\sim 0.6$ , which means the impurity of Cu can increase the disorder in graphene grown from scratch. For this reason, high-purity Cu is generally favored for growing high-quality graphene in conventional CVD [130]. Defective graphene films ( $I_D/I_G$  ratio  $\sim 0.6$ ) are synthesized purposefully using Cu (99.8%) in our modified IDF burner, and then a post-growth hydrogen annealing is performed in-situ at 1000°C in the same experiment using the same setup. All graphene

samples are grown at 1000°C with a  $J_{CH4}/J_{H2}$  of 1:100 for 5 min. Typical Raman spectra of the defective graphene after treating with hydrogen annealing are shown in Fig 6.5. Interestingly, after 5 min treatment, the  $I_D/I_G$  ratio increases significantly from  $\sim 0.6$  to  $\sim 1$ . The ratio is 1.2 after 10-min annealing. However, if the annealing time is extended to 12-15 min, the  $I_D/I_G$  ratio slightly decreases in some cases. Ratios over 1.2 are not observed for any cases studied. The rising of  $I_D/I_G$  ratio confirms that more defects *can be* induced in graphene through hydrogen annealing, especially when the starting film is already quite defective. One thing to notice is that the  $I_G/I_{2D}$  ratio is very steady with respect to annealing time. The  $I_G/I_{2D}$  ratio is an indicator of the number of layers within graphene. However, in a recent study of NPG, the Raman spectra of a suspended MLG can dramatically change after different exposure time to oxygen plasma (see Fig. 6.1b). The number of layers does not change in the suspended MLG, but the chemical structure can change significantly after the plasma damage. The shape, wavenumber, and intensity of the graphene 2D band are strongly impacted by not only the number of graphene layers but also the perfection of the graphitic chemical structure. The vacancy, divacancy, or even nanoscale pores can create many kinds of structural defects and disorders in graphene. A high-resolution TEM image shows the chemical structure of flame-synthesized defective graphene (see Fig. 6.6a). Many kinds of graphene structural defects like vacancy, double vacancy, and Stone-Wales defect can be clearly observed by comparing the enlarged TEM image of defective graphene and pristine flame-synthesized MLG at the same magnitude (see Fig. 6.6b, c). The exact defect types exhibited in as-synthesized defective graphene

is difficult to be identified clearly because of the limitation in the image resolution; nevertheless, an abundant variety of defects exist. However, such subnanometer defects, in general, afford some unique properties that have great potential in a wide range of applications. The Raman spectra provide a qualitative assessment of the density and size of graphene defects. The steady  $I_G/I_{2D}$  ratio with growth time indicates that the carbon graphitic structure is retained in general during hydrogen annealing. Thus, by utilizing the hydrogen annealing treatment, the annealing condition can be used to tune the defects in flame-synthesized graphene films. Unlike the other approaches, such as ion irradiation and oxygen plasma bombardment, our approach offers a direct way to produce highly defective graphene with tunable defects.

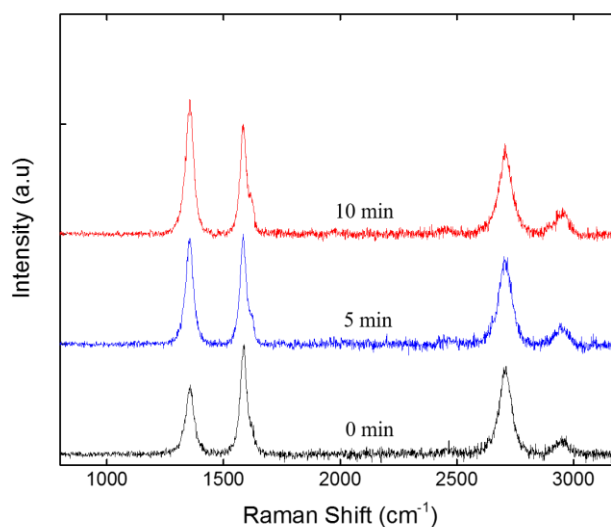


Figure 6.5 Raman spectra of defective graphene with different hydrogen annealing time. Substrate background signal is subtracted. The spectra are normalized with the G band.



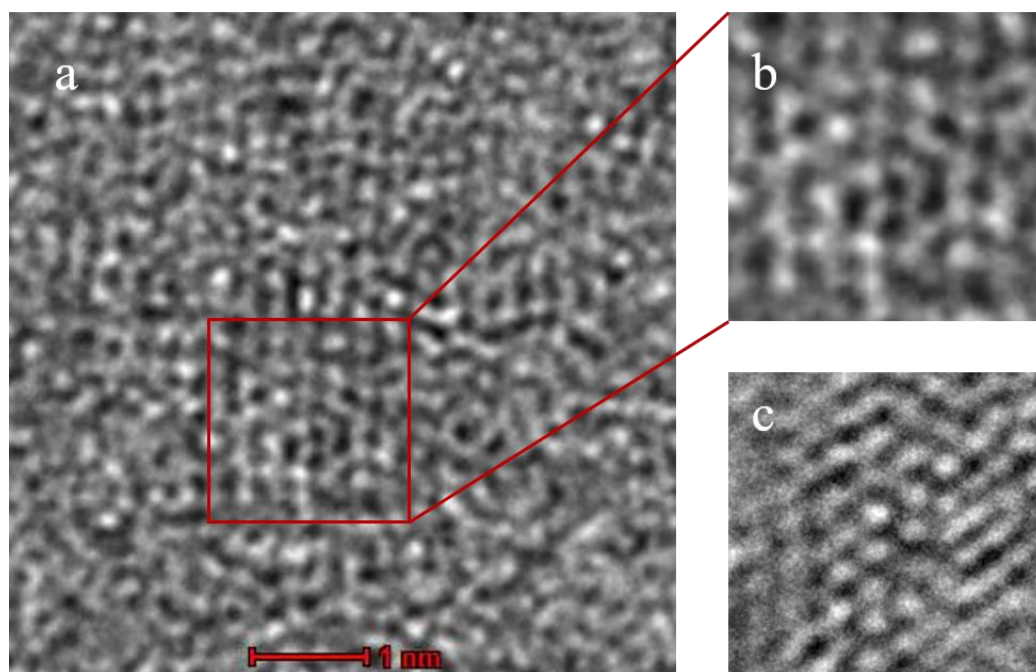


Figure 6.6 a) High-resolution TEM image of flame-synthesized defective graphene captured by Room Temperature Scanning/Transmission Electron Microscope (FEI Talos F200X S/TEM, 200 kV). b) Enlarged image of the selected area (red circled) of (a). c) Enlarged TEM image of Fig. 5.3a.

Besides the direct observation of graphene defects, the properties of as-grown defective graphene are investigated. UV-Visible Spectroscopy is used to determine the band gap structure of graphene in the presence of defects. Band gaps in defective graphene samples are of interest because of the absence of a bandgap in perfect MLG, which cannot provide the on-off switching needed in transistor applications. Nonzero bandgap can be created and tuned in BLG by applying an electric field or uniaxial strain [41], [63], [64], [123], [131]. Doping is another promising way to open and engineer the bandgap in graphene. Either substitutional doping of nitrogen and boron atoms in graphene structure or adsorption of groups and molecules (e.g.,  $\text{H}_2\text{SO}_4$ ,  $\text{N}_2\text{O}_4$ , AuPt,  $\text{Au}_3\text{Pt}_3$ ,

etc.) can open the band gap of graphene [67], [131]. Perhaps highly-defective graphene can be another avenue to give band gap properties.

Firstly, UV-Visible spectroscopy is performed on as-synthesized defective graphene still attached to its Cu substrate. The band gap energies are measured via the Diffuse Reflectance Derivative Peak Fitting (DPR) method, where the center of each Gaussian peak fit to the first derivative,  $dR_{\infty}/d\lambda$ , spectra corresponds to a band gap [132]. Prior to band gap analysis, the background signal from the Cu substrate is subtracted from the absolute reflectance of the sample. The band energies of defective graphene in the low-energy range (800 nm to 1000 nm) are shown in Fig. 6.7. In the mid-energy range, Cu exhibits a strong plasmonic resonance around 580 nm. Four individual band energies are determined after Gaussian peak fitting (see Table 6.1). The overall band gap observed is  $\sim 1.4$  eV, which is higher than that of NPG ( $< 1$  eV) made by other approaches. It is noted that with increasing defects, the area of the Gaussian peaks in the low-energy BGE region increases indicating that by creating more defects, band gaps can be opened in graphene. The concentration of these gaps seems to be correlated to the number of defects in the graphene.

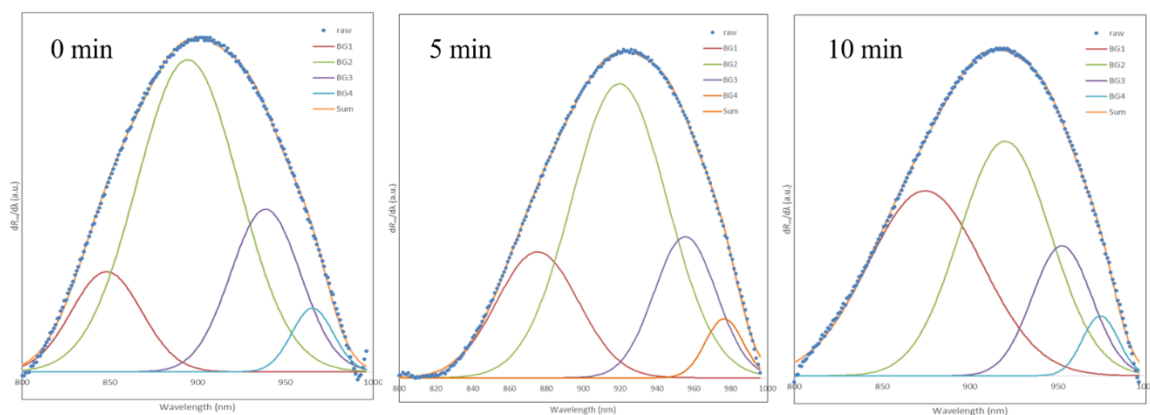


Figure 6.7 Band energies of flame-synthesized defective graphene with Cu substrate at different post-growth hydrogen annealing time. The background from Cu Plasmonic resonance (580 nm) is subtracted for all the samples.

Table 6.1 Band energies of defective graphene with different ID/IG ratio

Case	Band A	Band B	Band C	Band D
0 min ( $I_D/I_G \sim 0.6$ )	1.46 eV	1.39 eV	1.32 eV	1.28 eV
5 min ( $I_D/I_G \sim 1.0$ )	1.42 eV	1.35 eV	1.30 eV	1.27 eV
10 min ( $I_D/I_G \sim 1.2$ )	1.4 eV	1.34 eV	1.30 eV	1.27 eV

In order to get better isolated diffuse reflectance spectra, as-grown defective graphene samples are transferred from Cu substrate to quartz or fused silica substrates, thus eliminating the strong signal at  $\sim 580$  nm due to the plasmonic resonance of Cu. Analysis of the Kubelka Munk of these samples (Figure 6.8) shows that the maximum absorption at  $\sim 270$  nm (4.6 eV), which corresponds to the  $\pi-\pi^*$  transition of the aromatic C=C bond in graphene [133], [134]. The shift in the peak position has been previously determined to correspond to the area of the aromatic system [133], [135]. The result indicates that the

redshift of the maxima could be used to monitor the increasing amount of defects in the sample.

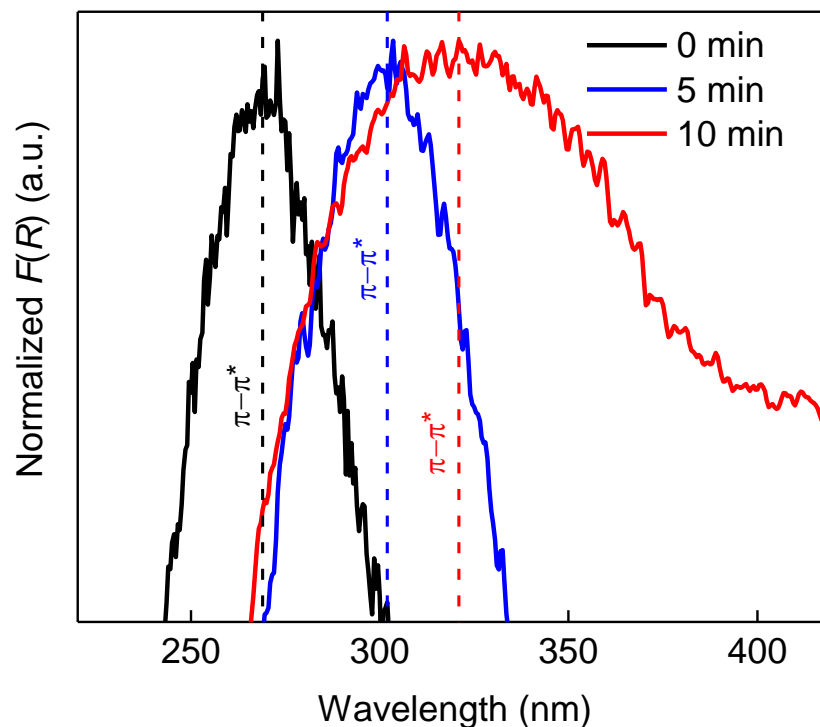


Figure 6.8 Normalized Kubelka Munk of Graphene samples, increasing time and increasing defects leads to a red-shift in the  $\pi-\pi^*$  transition of the aromatic C=C bond in graphene.

An exception is observed on ultrasmooth Cu (99.8%) provided by Army Research Lab in Aberdeen. By performing the same flame synthesis process, graphene grown on ultrasmooth Cu surface exhibits a remarkably large D peak with an  $I_D/I_G$  ratio  $\sim 1.2$ , which was never observed on commercial Cu (99.8%) substrates (see Fig. 6.9). The electropolished surface may contain residuals from electrolytes, which induces more defects in graphene growth. Another possibility is that the nucleation density of graphene

is higher on a smoother surface. After hydrogen annealing for 10 min, the  $I_D/I_G$  ratio is reduced to  $\sim 1$ , and  $I_G/I_{2D}$  rate is slightly increased. At some locations,  $I_G/I_{2D}$  rate can be smaller than 0.7, indicating MLG. Therefore, hydrogen annealing cures some defects and reduces the number of layers in this highly defective graphene originally grown on ultrasmooth Cu.

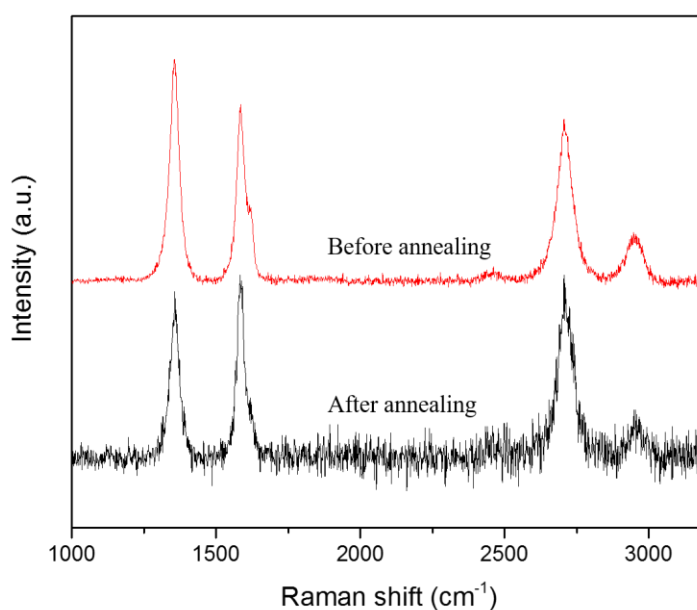


Figure 6.9 Raman spectra of ultrasmooth Cu sample before and after hydrogen annealing. Ssubstrate background signal is subtracted. The spectra are normalized with the G band.

The outcome of hydrogen annealing is a combination of several effects, including the interaction between hydrogen and carbon dangling bonds, the catalytic mechanism of the substrate, and the rearrangement of carbon atoms at high temperature. Based on our studies, such outcome is highly depending on the original graphene chemical structure and

substrate materials. Both MLG and highly defective graphene can be achieved by utilizing this treatment.

### 6.3.3 Potential Applications of Highly Defective Graphene

One of the main potential applications of highly-defective graphene is ultrafiltration, such as ion selection, gas separation, water desalination, and even DNA sequencing. Recent studies suggested that porous graphene membranes exhibit orders of magnitude higher flow rates than commercial reverse osmosis membranes, as well as have excellent salt rejection properties [136]. To study the ion rejection property of flame-synthesized defective graphene, a conductance measurement is performed in collaboration with the Shan research group, Rutgers MAE. As-grown defective graphene films are transferred to round pinholes with 5  $\mu\text{m}$  aperture. In the measurements, conductance comes from three parts: a) the open area; b) the access resistance (effective for very thin pores/membranes like graphene); and c) surface charge. The general formulation, taking into account the contribution of the surface charge ( $\Sigma$ ) is:

$$G = \kappa_b \left[ \frac{4L}{\pi d^2} \times \frac{1}{1 + 4 \frac{l_{du}}{d}} + \frac{2}{\alpha d + \beta l_{du}} \right]^{-1}$$

where  $\kappa_b$  is the bulk conductivity,  $L$  is the pore length,  $d$  is the pore diameter;  $l_{du}$  is the Dukhin length (which can be approximated by  $\frac{|\Sigma|/e}{2c_s}$ , where  $e$  is the elementary charge and  $c_s$  is the salt concentration);  $\alpha$  is a geometrical prefactor that depends on the model used; and  $\beta$  can be approximated to be 2 to obtain the best fitting agreement [137]. To eliminate

the surface charge effect, the molarity of the KCl solution is increased to 1 Mole/L, for the graphene membranes tests. In this case, the formulation becomes:

$$G = \kappa_b \left( \frac{4L}{\pi d^2} + \frac{1}{d} \right)^{-1}$$

for the estimation of the pore size based on the measured conductance of the membrane [136]. Here, the first term is the bulk conductance, and the second term is the access resistance. From the I-V curve slope, the conductance can be obtained; and from the conductance, the effective open-area diameter,  $d$ , can be estimated for a known membrane thickness value. In the estimation, the thickness of 1 nm for graphene is used. For the control template, 14.7 microns (thickness of the 5- $\mu$ m pinhole) is used. Only the effective diameter of the total open area can be estimated since the value of individual pore diameters and density of defects are unknown. The conductance results of the control sample (bare 5- $\mu$ m pinhole) and defective graphene membranes with different  $I_{D/G}$  ratio are listed in Table 6.2. The estimated effective diameter of the control sample calculated using the formula above is 4.93  $\mu$ m, whose error is around 1%. Since the testing area is the same (i.e., 5  $\mu$ m) for all the samples, the estimated open-area percentage is calculated by  $\left(\frac{d}{d_c}\right)^2$ , where  $d_c$  is the effective diameter of the control sample. For the case of  $I_{D/G} \sim 0.6$ , the estimated open-area percentage is 0.000023%, which implies the membrane is nearly impermeable to the ions. As the  $I_{D/G}$  ratio increasing, the estimated open-area percentage also increases. For the most defective case  $I_{D/G} \sim 1.2$ , the estimated open-area percentage is 0.8%. If the pore diameter is known and the pore sizes are uniform, the pore number can be estimated by this approach.

Table 6.2 Results of conductance measurements and estimated open-area diameter and percentage respect to different  $I_D/I_G$  ratios

Case	Conductance G (S)	Effective diameter	Open-area percentage
Control	1.21E-05	4.93 $\mu$ m	100%
$I_D/I_G \sim 1.2$	4.53E-06	0.44 $\mu$ m	0.8%
$I_D/I_G \sim 1.0$	1.57E-06	0.15 $\mu$ m	0.09%
$I_D/I_G \sim 0.6$	1.62E-08	0.0024 $\mu$ m	2.3E-5%

The nitrogen permeability has been measured for all of the defective graphene membranes. However, nearly no nitrogen flow is observed in any sample. Many reports in the literature suggest that nitrogen is nearly impermeable in NPG because of the surface adsorption [73], [138], [139]. The nitrogen impermeability of flame-synthesized defective graphene implies the size of defects is mainly sub-nanometer. Such property may afford a wide range of applications in gas separation. Based on current results, flame synthesis appears to have the potential to synthesize directly graphene with tunable defects (number and size), affording a wide range of ion selection and gas separation membrane applications.

The membrane quality still needs to be improved by utilizing some other substrate materials and fabrication techniques. As long as high-quality membrane samples can be consistently prepared, the properties of flame synthesized defective graphene can be systematically studied.



## 6.4 Concluding Remarks

Post-growth hydrogen annealing is performed on graphene samples with different original conditions and substrate materials, such as ultrapure Cu, Cu, Ni, Si and ultrasmooth Cu. The etching effect of hydrogen annealing is predominantly a metal-assisted process because graphene transferred to Si substrate stays unchanged before and after annealing treatment. However, the etching effect can be very strong on graphene sample containing lots of defects, regardless the substrate material. Based on current results, the critical initial  $I_D/I_G$  ratio found in this work is  $\sim 0.6$ . The  $I_D/I_G$  ratio increases dramatically after hydrogen annealing when as-synthesized graphene on Cu exhibits an initial ratio of at least 0.6. However, the  $I_D/I_G$  ratio does not change obviously after annealing if the initial ratio is lower than 0.6. Inspired by such phenomenon, “low-quality” graphene is intentionally produced on low-purity Cu substrate, and then highly defective graphene films with tunable defective level are achieved by employing hydrogen annealing treatments. Current methods mainly use ion irradiation or plasma to damage CVD-synthesized graphene in order to create nanoscale or subnanoscale defects. However, such methods requiring expensive setups, and multiple steps may not be economically viable for large-scale production. Our well-controlled flame method offers a readily available route to synthesize directly highly-defective graphene scalably, economically and rapidly. By controlling the number of defects, a direct band gap can be opened up in flame-synthesized graphene. The BGE is analyzed by UV-Vis spectroscopy. The chemical structure of as-synthesized highly defective graphene is studied using high-resolution TEM. Various

types of defect including point defect, divacancy, and Stone-Wales defect are observed.

Such subnanometer defect sites contribute to the direct BGE, affording many applications.

The filtration property of the highly-defective graphene as a membrane is investigated, showing potential in ion selection and gas separation.

## Chapter 7

### 7. Unconfined Flame Synthesis of CNTs on Metals and Nonmetals

#### 7.1 Introduction

Flame synthesis is a common production method used in manufacturing large-quantity commodity nanoparticles like titania and carbon black. Besides flame aerosol processes, CVD-type flame synthesis has been used in producing nanostructured metal-oxides directly on metal substrates including tungsten [140], [141], zinc [142], copper [90], iron [90] and molybdenum [91]. The synthesis of carbon nanomaterials (e.g., graphene, CNTs) on metal substrates using flame processes have been demonstrated [4], [23], [143]. However, for many electronic applications, CNTs are required to sit on insulation surfaces. The growth of CNTs on a silicon substrate has been done using CVD with pre-seeded catalytic metal particles on the substrate. MWNTs have been synthesized on silicon substrates using diffusion flame synthesis with a shadow mask [144]. Flame synthesis of well-aligned CNT arrays on silicon is also reported using porous alumina film as a nanotemplate [145]. To the best of our knowledge, SWNTs and well-aligned CNT arrays have not been synthesized on Si without a template using a CVD-type flame process to date.

Carbon-metal oxide (CMO) nanocomposites have been extensively investigated because of the increasing demand for energy storage devices. CMO nanocomposites consist of carbon and metal oxides, such as  $\text{TiO}_2$ ,  $\text{V}_2\text{O}_5$ ,  $\text{Mn}_3\text{O}_4$ ,  $\text{Fe}_2\text{O}_3$ ,  $\text{Co}_3\text{O}_4$ ,  $\text{NiO}$ ,  $\text{CuO}$ ,  $\text{ZnO}$ ,  $\text{RuO}_2$ ,  $\text{SnO}_2$ , and  $\text{WO}_3$ , and exhibit improved performance as electrode materials [21]. Flame synthesis that can provide either oxidizing or carbon-rich environment is a well-suited technique for the manufacture of CMOs. Scalability and high production rate make flame synthesis a feasible technique for the mass production of such materials.

Iron oxide nanoparticles have drawn extensive research interest because of its unique magnetic and optoelectronic properties, as well as their potential applications in many fields (e.g., magnetic storage devices, sensors, etc.) [146], [147]. Iron oxides are commonly in the form of magnetite ( $\text{Fe}_3\text{O}_4$ ), maghemite ( $\gamma\text{-Fe}_2\text{O}_3$ ), and hematite ( $\alpha\text{-Fe}_2\text{O}_3$ ). The property of iron oxide nanoparticle is determined by its chemical composition and morphology.  $\gamma\text{-Fe}_2\text{O}_3$  nanoparticles have been produced in an aerosol process using a hydrogen/air diffusion flame [148]. Buyukhatipoglu et al. [149] reported  $\alpha\text{-Fe}_2\text{O}_3$  and  $\text{Fe}_3\text{O}_4$  nanoparticles that formed in co-flow diffusion and inverse diffusion flame configurations.

Since iron is also known as one of the catalysts promoting CNTs growth, flame synthesis can be used to study the growth conditions for both iron oxide nanoparticles and CNTs separately, using the same experimental configuration. Such technique also enables the growth of CNT-iron oxide nanocomposites, which can be used in various applications such as batteries, sensors, and solar cells. The multi-element inverse

diffusion flames (m-IDFs) burner setup is employed in this work. Various seeding recipes used by CVD methods are investigated for the growth of CNTs on Si substrate using flame synthesis.

## 7.2 Experiment

The m-IDF burner operates in inverse mode (see Fig. 7.1). On the burner surface, each individual diffusion flame in the planar array has oxidizer issuing in the center with fuel (e.g.,  $H_2$ ,  $CH_4$ ) issuing around it. In the experiment, pyrolysis gases from the flame can provide both carbon species ( $CH_4$ ,  $C_2H_4$ ,  $C_2H_2$ , etc.) and oxygen species ( $H_2O$ ,  $CO_2$ ,  $CO$ ) needed for the growth of CNTs and iron oxides, respectively. Since bulk iron is not capable of catalyzing the decomposition of methane, it has to be first dispersed. Therefore, various types of stainless steel foils, including type 304, 304L, and 316L, are investigated as the catalytic substrates. The chemical composition of each type of stainless steel is shown in Table 7.1. The main difference between type 304 and 304L stainless steel is the carbon content, while the main difference between type 304L and 316L is the presence of molybdenum. Therefore, by comparing the results using these substrates for the same experimental condition, the impacts of carbon and molybdenum contents on the growth of CNTs and iron oxides can be assessed. Prior to the growth, the substrate is reduced in hydrogen-rich m-IDFs for 10 min to remove the passive oxidation layer. Subsequently, methane is introduced (with a global equivalent ratio of  $\sim 3$ ) for 10 min. The gas flow rate ratio between methane and hydrogen is kept at 1:10.

As the multiple flames result in a radially uniform temperature and profile of species in the downstream, the gas-phase temperature is mainly a function of the axial distance between substrate and burner surface. The axial position of the substrate can be adjusted to maintain suitable growth temperature.

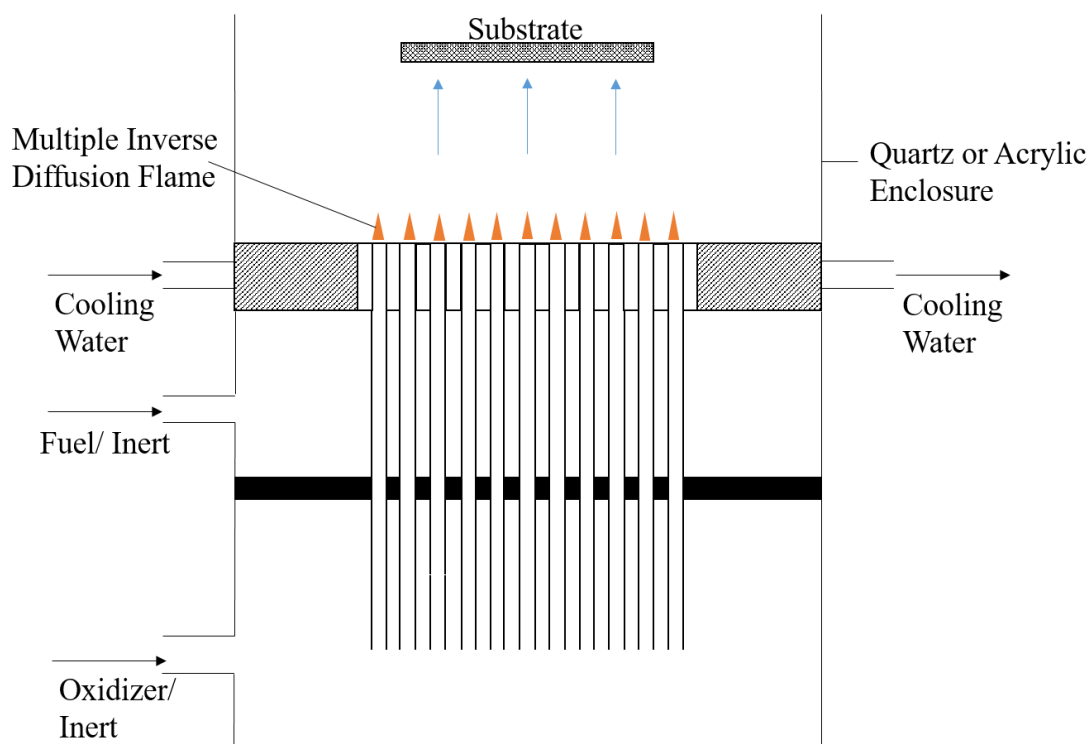


Figure 7.1 Schematic diagram of m-IDF burner used to synthesize CNTs.

Table 7.1 Chemical composition of various types of stainless steel

	Type 304 [wt.%]	Type 304L [wt.%]	Type 316L [wt.%]
Carbon	0.08 max.	0.03 max.	0.03 max.
Manganese	2.00 max.	2.00 max.	2.00 max.
Phosphorus	0.045 max.	0.045 max.	0.045 max.
Sulfur	0.03 max.	0.03 max.	0.03 max.
Silicon	0.75 max.	0.75 max.	0.75 max.
Chromium	18.00-20.00	18.00-20.00	16.00-18.00
Nickel	8.00-12.00	8.00-12.00	10.00-14.00
Nitrogen	0.1 max.	0.1 max.	0.1 max.
Molybdenum	N/A	N/A	2.00-3.00
Iron	Balance	Balance	Balance

Si/SiO<sub>2</sub> is used as the non-metal substrate for CNT growth. Prior to flame synthesis, the silicon substrate is first dipped in a seeding solution for 5-10 min and then baked in an oven at 400 °C, decomposing the seeds to become dispersed metal-oxide nanoparticles. Various CVD-type seeding recipes including FeCl<sub>3</sub>, Co acetate, and Mo acetate in aqueous or alcohol solvent are available [83], [150]. Prior to CNT growth, the substrate is preheated in the multiple inverse hydrogen flames for 10 min to reduce the metal-oxide nanoparticles to metal nano-catalysts. Then growth synthesis starts, and the substrate temperature is maintained at 850 °C, with carbon-nanostructure growth time varying from 10 to 20 min.

X-ray photoelectron spectroscopy (XPS, Thermo Scientific K-Alpha) analysis of Fe 2p orbital is employed to characterize the chemical composition of the stainless steel

substrate. On the raw surface, peaks for Fe 2p<sub>3/2</sub> and Fe 2p<sub>1/2</sub> located at 709.8 eV and 722.8 eV, respectively, are associated with the 2+ ion in Fe<sub>3</sub>O<sub>4</sub> (see Fig. 7.2). There are no identifiable satellite peaks at 718.9 eV or 732.8 eV, corresponding to Fe<sub>2</sub>O<sub>3</sub>. This result confirms that the raw stainless steel foil initially has a multicomponent oxide layer on it. X-ray diffraction (XRD) and Raman spectroscopy (Renishaw 1000, 514 nm laser wavelength, 50× magnification) are used to identify the crystal structures of as-synthesized iron oxides and CNTs. The morphology of the samples is characterized using scanning electron microscope (SEM, Zeiss Sigma 8100).

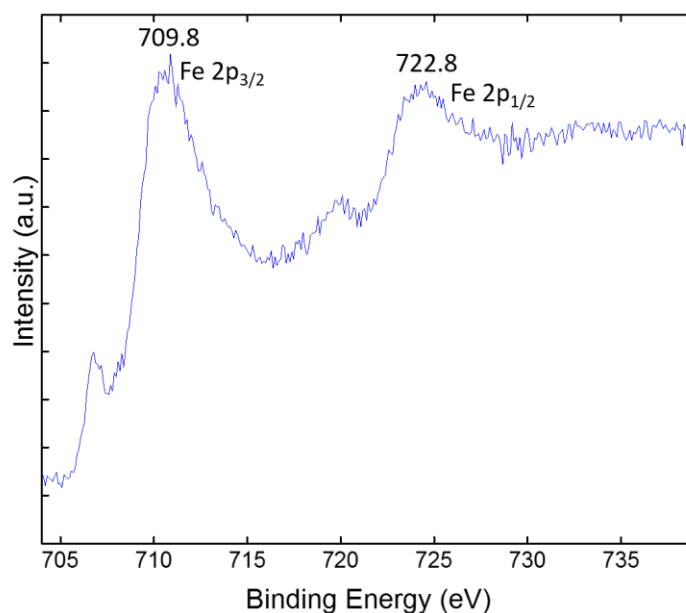


Figure 7.2 Fe 2p XPS spectrum is showing Fe<sub>3</sub>O<sub>4</sub> on raw surface of stainless steel.



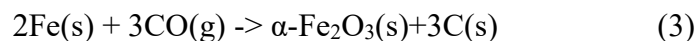
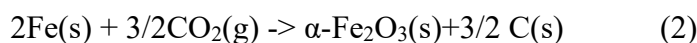
### 7.3 Results and Discussion

#### 7.3.1 Synthesis of CNTs and Iron Oxide Nanoparticles on Stainless Steel

The growth of CNTs and iron oxides on stainless steel are conducted at low temperature (500 °C) and high temperature (850 °C) separately. A low-to-high temperature synthesis is utilized to grow CNTs and iron oxide nanocomposite materials. The effects of different alloys (contents) of stainless steels on the growth of CNTs are studied.

##### *7.3.1.1 Low-Temperature growth of $\alpha$ -Fe<sub>2</sub>O<sub>3</sub> Nanoparticle Film*

First, when type-304 stainless-steel substrate temperature is heated at 500 °C, iron-oxide nanoparticles nucleate on the surface and develop into a nanocrystalline film (see Fig. 7.3a). The raw surface of type-304 stainless-steel is initially covered by a passivative oxide layer, from which, when exposed to product gases of m-IDFs,  $\alpha$ -Fe<sub>2</sub>O<sub>3</sub> nanoparticles precipitate out of the substrate maintained at 500 °C. Since oxygen is completely consumed by the flame, the growth of iron-oxide should be due to the presence of CO<sub>2</sub>, CO, and H<sub>2</sub>O. These species can react with iron substrates via various routes, such as:



Based on the calculated Gibbs free energies (see Table 7.2), the oxidation reactions with H<sub>2</sub>O and CO<sub>2</sub> are spontaneous at temperatures less than ~550 °C, and with CO at

temperatures less than  $\sim 700$  °C. Therefore, at the experimental substrate temperature of 500 °C (773 K), all three oxidation reactions with iron are favorable.

Table 7.2 Gibbs free energies of reactions, calculated with thermochemical data from NIST-JANAF tables (1998) at 1 atm, for the investigated growth of  $\alpha$ -Fe<sub>2</sub>O<sub>3</sub>

T (K)	T (°C)	$\Delta G^\circ$ (kJ/mol), Eq. (1), 2Fe(s) + 3H <sub>2</sub> O(g) $\rightarrow$ $\alpha$ - Fe <sub>2</sub> O <sub>3</sub> (s)+3H <sub>2</sub> (g)	$\Delta G^\circ$ (kJ/mol), Eq. (2), 2Fe(s) + 3/2CO <sub>2</sub> (g) $\rightarrow$ $\alpha$ -Fe <sub>2</sub> O <sub>3</sub> (s)+3/2C(s)	$\Delta G^\circ$ (kJ/mol), Eq. (3), 2Fe(s) + 3CO(g) $\rightarrow$ $\alpha$ -Fe <sub>2</sub> O <sub>3</sub> (s)+3C(s)
700	427	-10.401	-43.740	-116.283
800	527	-0.989	-18.098	-63.986
900	627	7.739	7.112	-12.262
1000	727	208.494	31.963	38.959

Raman spectroscopy is employed to characterize the phase of the iron-oxides. The typical Raman spectrum for m-IDF-treated 304 stainless steel sample is shown in Fig. 7.3b. The major peaks located at 238, 300, 417, 500, 616, 1320 cm<sup>-1</sup> can help to distinguish  $\alpha$ -Fe<sub>2</sub>O<sub>3</sub> (hematite) from other phases. The narrow doublet at 238 and 300 cm<sup>-1</sup> is associated with  $\alpha$ -Fe<sub>2</sub>O<sub>3</sub> [151], where slight shifts occur because of different laser powers [152]. Here, the growth of  $\alpha$ -Fe<sub>2</sub>O<sub>3</sub> leads to a yellowish tint on stainless steel. The same experimental procedure is repeated on types 304L and 316L stainless-steel substrates; and their Raman spectra are shown in Fig. 7.3c and d, respectively. Very similar  $\alpha$ -Fe<sub>2</sub>O<sub>3</sub> nanoparticle film growth is observed in all three alloys of stainless steel. XRD tests are performed on all samples, but only iron signals are recorded, indicating that the oxide layers are a very thin.

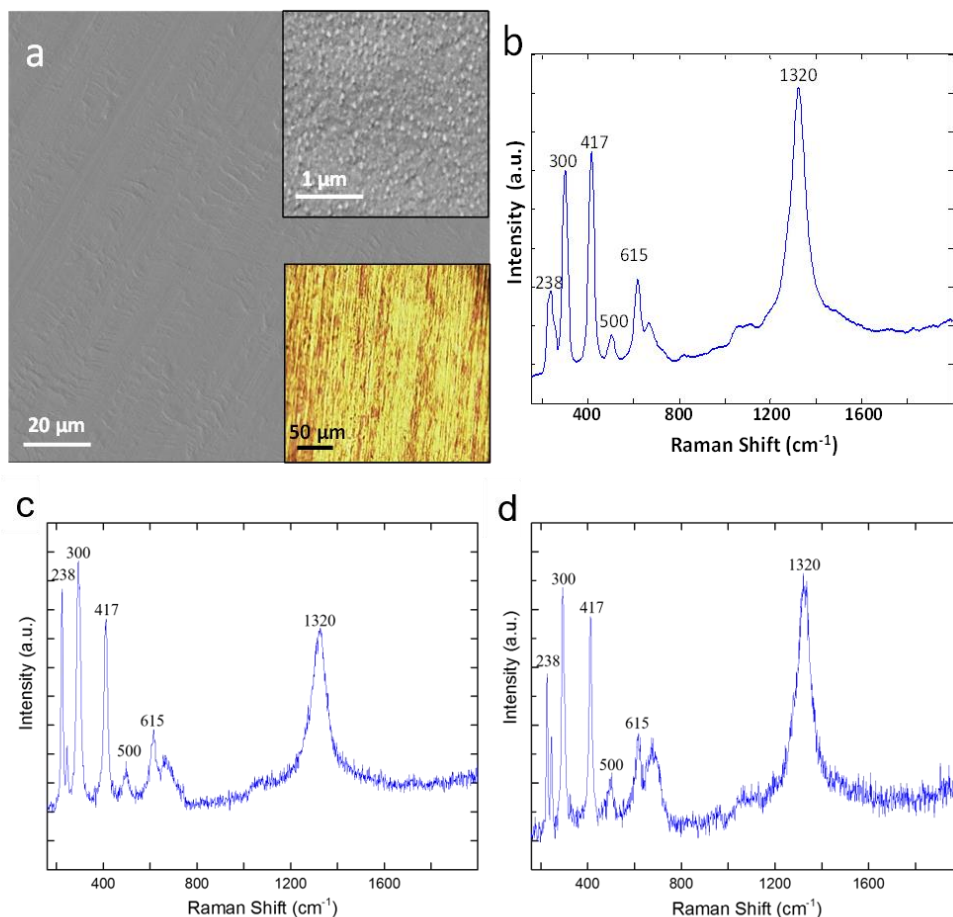


Figure 7.3 Iron oxide nanocrystalline film grown on stainless steel at a temperature of 500 °C. (a) SEM image shows the morphology of iron oxide nanocrystalline film stainless steel. The top right inset shows a magnified image of the film. The bottom right inset shows an optical image of the film. Raman spectrum confirms the  $\alpha$ -Fe<sub>2</sub>O<sub>3</sub> phase growth on 304 (b), 304L (c), 316L (d) stainless steel.

XPS is utilized to characterize the chemical bonding of iron-oxide nanostructures formed on type 304, 304L, and 316L stainless steel. XPS analysis of Fe 2p orbital shows that peaks for Fe 2p<sub>3/2</sub> and Fe 2p<sub>1/2</sub> are located at 710.7 and 724.5 eV, respectively (see Fig. 7.4a, c, e). These peaks correspond to the 3+ ion in Fe<sub>2</sub>O<sub>3</sub>, as the peaks for the 2+ ion in Fe<sub>3</sub>O<sub>4</sub> are located at 709.8 eV (Fe 2p<sub>3/2</sub>) and 722.8 eV (Fe 2p<sub>1/2</sub>) [153]. Additionally, the identified satellite peaks at 718.9 eV and 732.8 eV confirm the composition as Fe<sub>2</sub>O<sub>3</sub> [154]. After argon-ion beam etching (for 10 s) of the sample, the XPS satellite peaks are no longer present (see Fig. 7.4b, d, f), which indicates that only a thin layer (<5 nm) of  $\alpha$ -Fe<sub>2</sub>O<sub>3</sub> covers the surface of the SS substrate.

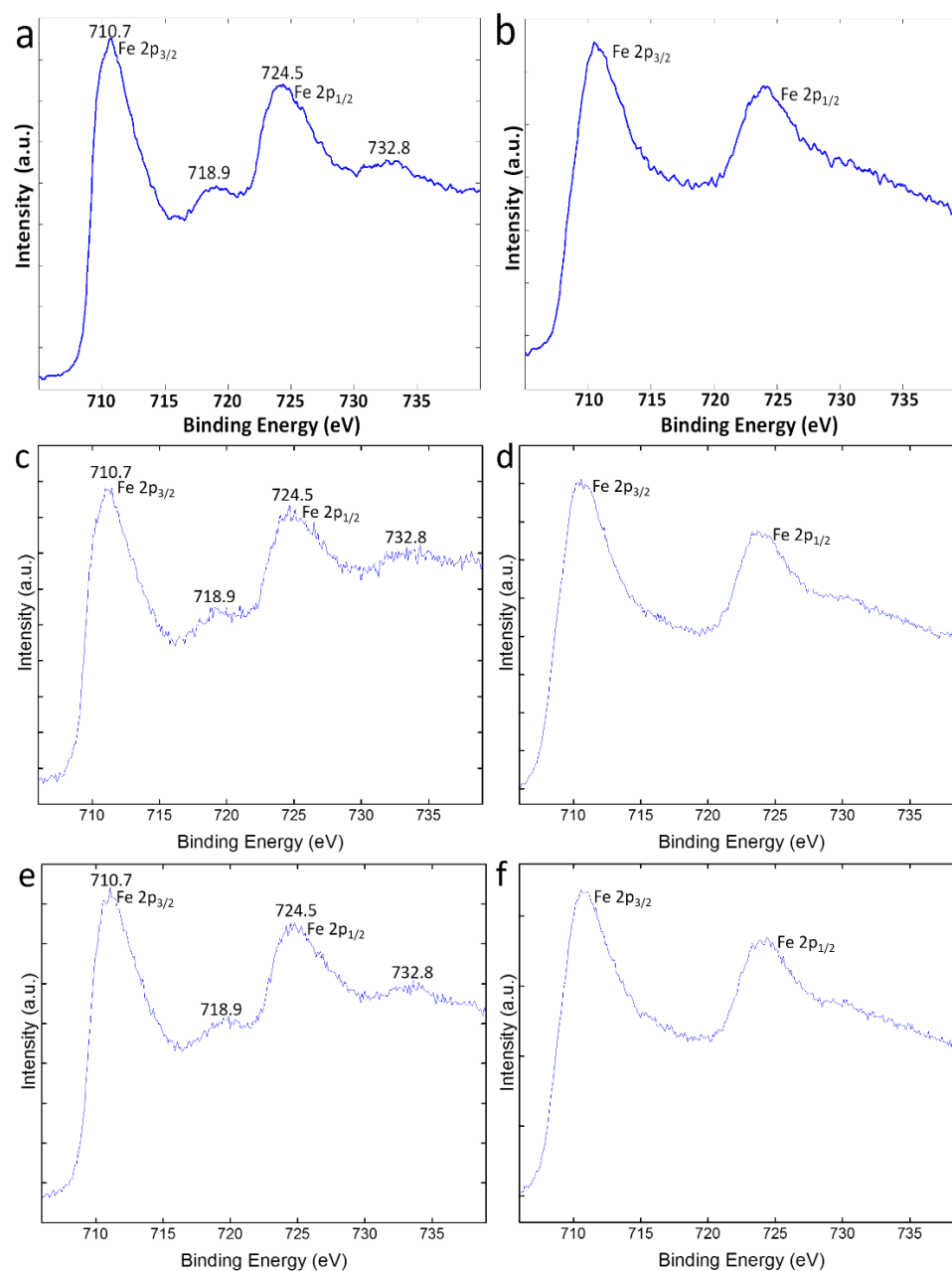


Figure 7.4 Fe 2p XPS spectrum is showing  $\alpha$ -Fe<sub>2</sub>O<sub>3</sub> for the nanocrystalline film growth on type 304 (a), 304L (c), 316L (e) stainless steel at 500 °C. Fe 2p XPS spectrum of the sample on type 304 (b), 304L (d), 316L (f) stainless steel after argon ion beam etching of the surface. It indicates the thickness of the  $\alpha$ -Fe<sub>2</sub>O<sub>3</sub> film is less than 5 nm.

### 7.3.1.2 High-Temperature growth of $\gamma$ -Fe<sub>2</sub>O<sub>3</sub> Nanocrystals, and CNTs

At a substrate temperature of 850 °C, few-layer graphene has been previously grown on copper and nickel substrates using the m-IDF burner. The growth of graphene on stainless steel has been reported for certain conditions using CVD [155]. However, the growth temperature is raised to 850 °C in our m-IDFs setup,  $\gamma$ -Fe<sub>2</sub>O<sub>3</sub> nanocrystals are observed on type 316L and 304L stainless steel (see Fig. 7.5a, b, respectively), while micro- and nanoscale carbon tubes and fibers are observed on type 304 stainless steel (see Fig. 7.5c). The growth of carbon nanostructures requires the nucleation of catalytic iron nanoparticles on the stainless steel substrate. The innate carbon content of the stainless steel plays an important role in forming carbides, such as Cr<sub>3</sub>C<sub>2</sub>, precipitating out at grain boundaries at this temperature. Subsequently, carbon-based species of the m-IDFs products undergo dissociative adsorption and diffuse through the cracks at the grain boundaries to form more Cr<sub>3</sub>C<sub>2</sub> and Fe<sub>3</sub>C, which break up the substrate surface [143], leading to carbon fibers and CNTs growing on the freshly exposed iron nanoparticles. For type 304L and 316L stainless steel, which have a maximum carbon content of 0.03%, no obvious carbon nanostructure is detected using SEM. However, for type 304 stainless steel with a maximum carbon content of 0.08%, the growth of carbon fibers and CNTs occurs readily as the higher innate carbon content promotes carbide-induced breakup and exposure of iron at the surface to form nanoparticles that allow for CNT growth. Interestingly, smaller-sized  $\gamma$ -Fe<sub>2</sub>O<sub>3</sub> nanocrystals are observed with some iron-oxide nanorods grown on type 304L stainless steel but not on type 316L. This can be due to the presence of molybdenum in

type 316L stainless steel, which prevents the growth of iron oxide nanorods and leads the nanocrystals to a larger size.

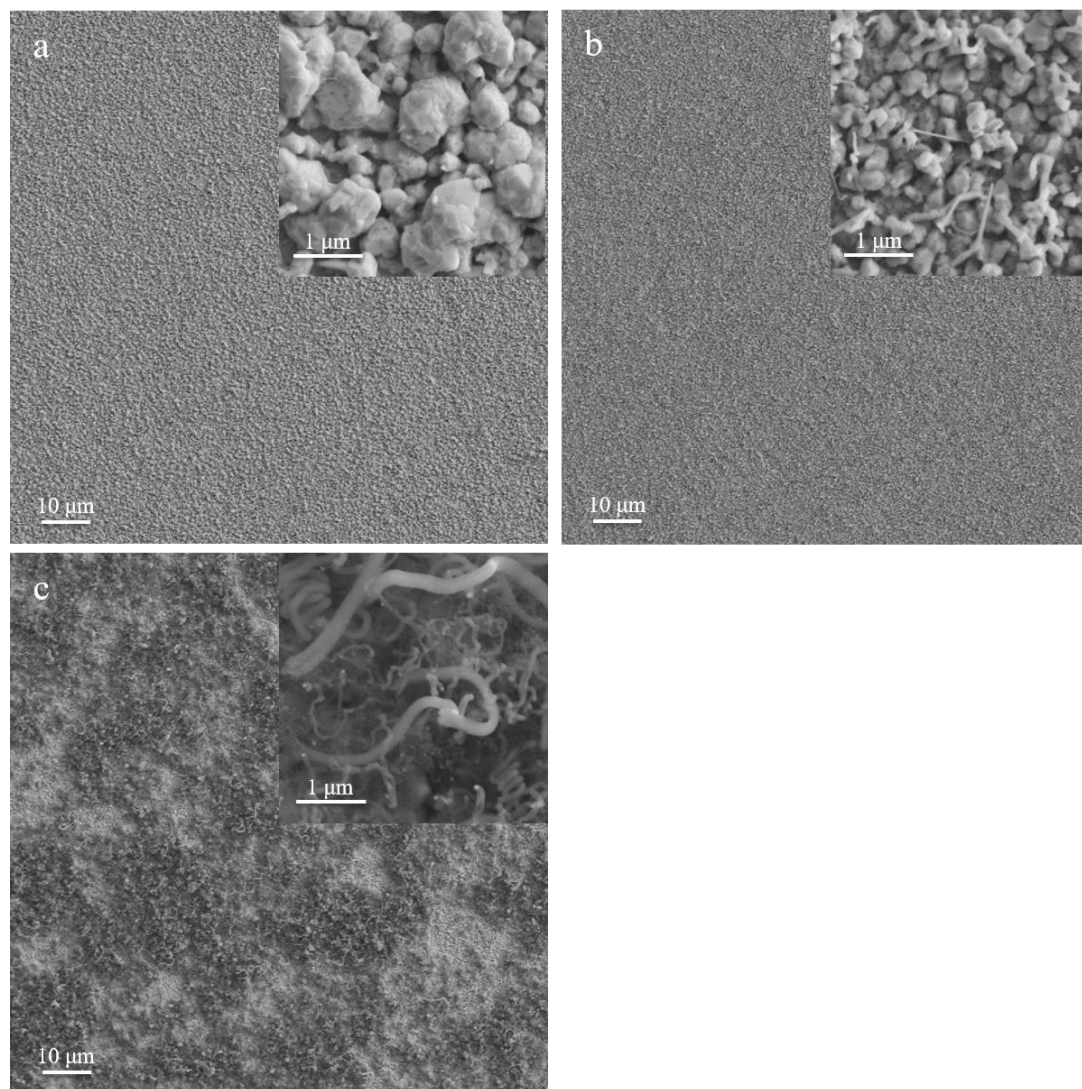


Figure 7.5 SEM images for 850 °C high-temperature growth on stainless steel. (a) The growth of  $\gamma$ -Fe<sub>2</sub>O<sub>3</sub> nanocrystals is observed on type 316L stainless steel. (b) The growth of  $\gamma$ -Fe<sub>2</sub>O<sub>3</sub> nanocrystals with some rogue iron oxide nanorods is observed on type 304L stainless steel. (c) The growth of micro- and nanoscale carbon fibers and tubes are observed on the type 304 stainless steel. The top right insets show the magnified SEM image of the films.

XRD is employed to confirm the growth of  $\gamma$ -Fe<sub>2</sub>O<sub>3</sub> nanocrystals on both 316L and 304L stainless steels (see Fig. 7.6). The appearance of iron background signals suggests that oxide layers on the substrates are very thin films.

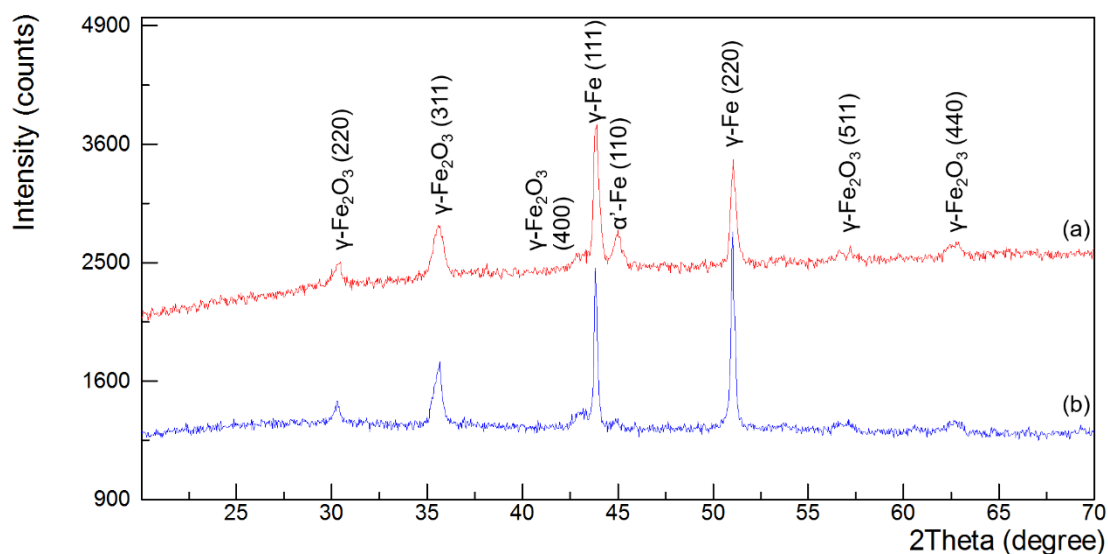


Figure 7.6 XRD for 850 °C high-temperature growth on stainless steel. The growth of  $\gamma$ -Fe<sub>2</sub>O<sub>3</sub> is confirmed on type 316L (a), 304L (b) stainless steel with the appearance of iron background signals implying thin film growth of oxide layer.

### 7.3.1.3 Two-step growth of $\gamma$ -Fe<sub>2</sub>O<sub>3</sub> Nanocrystals and CNTs Hybrid Materials

The synthesis of  $\gamma$ -Fe<sub>2</sub>O<sub>3</sub> nanocrystals is demonstrated on type 304L and 316L stainless steel, while CNTs are grown on type 304 stainless steel at 850 °C using the m-IDF burner.  $\alpha$ -Fe<sub>2</sub>O<sub>3</sub> nanoparticle films grow on 304, 304L, and 316L stainless steel at 500 °C. Thus, such technique enables the direct growth of nanocomposite materials based on  $\gamma$ -Fe<sub>2</sub>O<sub>3</sub> nanoparticles and CNTs. A low-to-high temperature growth process is investigated on type 304 stainless steel as substrate. After 10-min growth at 500 °C, a thin film of



nanocrystalline  $\alpha$ -Fe<sub>2</sub>O<sub>3</sub> is grown across the substrate. Subsequently, the growth temperature is stepped up to 850 °C, and larger-sized  $\gamma$ -Fe<sub>2</sub>O<sub>3</sub> nanocrystals along with carbon nanofibers and CNTs are observed (see Fig. 7.7a). Raman spectroscopy identifies the phase of Fe<sub>2</sub>O<sub>3</sub> nanoparticles. The major peaks located at 1350, 1593 and 2700 cm<sup>-1</sup> correspond to CNTs, while the peaks at 553, 687, and 714 cm<sup>-1</sup> correspond to  $\gamma$ -Fe<sub>2</sub>O<sub>3</sub>. The broad and strong band at 680 to 720 cm<sup>-1</sup> with a shoulder peak is the key feature of the Raman spectrum for  $\gamma$ -Fe<sub>2</sub>O<sub>3</sub> [151]. The transformation from alpha-phase to gamma-phase Fe<sub>2</sub>O<sub>3</sub> has been reported in hydrogen environment [156], [157]. The  $\alpha$ -Fe<sub>2</sub>O<sub>3</sub> nanocrystalline thin film can grow into larger  $\gamma$ -Fe<sub>2</sub>O<sub>3</sub> nanocrystals at 850 °C in the presence of excess hydrogen. The CNT growth occurs because of the innate carbon content, which allows carbide formation and breaks up of the substrate surface.

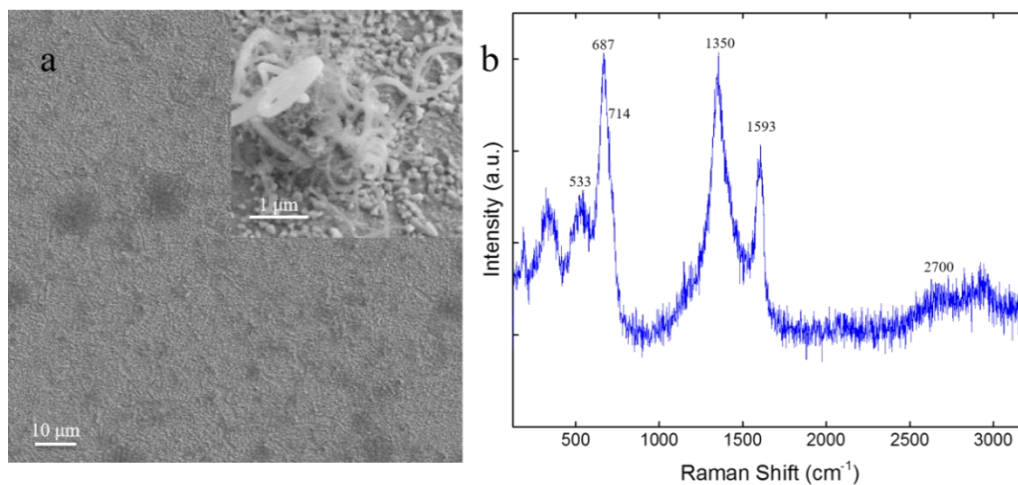


Figure 7.7 (a) FESEM confirms the hybrid growth of CNTs and iron oxide nanocrystals on type 304 stainless steel using 500 °C-to-850 °C two-step growth process. The top right inset shows the magnified SEM image of the film. (b) Raman spectrum is confirming the presences of carbon nanostructure and  $\gamma$ -Fe<sub>2</sub>O<sub>3</sub> particles.

### 7.3.2 CNT Synthesis on Non-metal Substrate

Entangled and well-aligned CNTs on Si or quartz have been achieved using various CVD processes [83], [158]. Metal catalysts are pre-deposited on Si substrate prior to the growth using a wet-chemistry seeding process. By following a similar seeding recipe, the growth of CNTs on Si should be repeatable using CVD-type flame synthesis. However, the high flow flux and large amounts of combustion product species (e.g.,  $\text{H}_2\text{O}$ ,  $\text{OH}$ ,  $\text{CO}$ ,  $\text{CO}_2$ ) keep flame synthesis from being a simple analog to CVD. If the growth conditions for CNTs are not optimal, metal catalysts can be deactivated. The deactivation can be due to the nanoparticles being completely encapsulated by carbon [21], [159] or the formation of oxides [83]. By seeding the substrate surface with catalytic particles, substrate properties can be decoupled from the nano-catalyst formation, and the growth of CNTs on non-metals using the m-IDF setup can be studied with ethylene and hydrogen as fuel. Different seeding recipes are investigated in this work.

#### 7.3.2.1 CNT growth using iron catalyst

Iron is a common metal catalyst for CNT growth. By submerging Si/SiO<sub>2</sub> wafer in FeCl<sub>3</sub> solution and baking in a furnace, nanoparticles of iron oxide are formed on the substrate. Using 10 mMole/L FeCl<sub>3</sub> aqueous seeding solution, entangled CNTs with diameters up to several hundred nanometers are grown on a silicon wafer (see Fig. 7.8a). The large variance in diameter implies that the sizes of catalytic particles are not uniform. Small particles can agglomerate to form larger particles during the heating process. When the

solution concentration is reduced to 1 mMole/L, the average diameter of CNTs is slightly decreased (see Fig. 7.8b), which implies that the average size of catalytic particles is reduced. Catalytic nanoparticles are observed on the tips and in the middle of the as-synthesized carbon nanotubes.

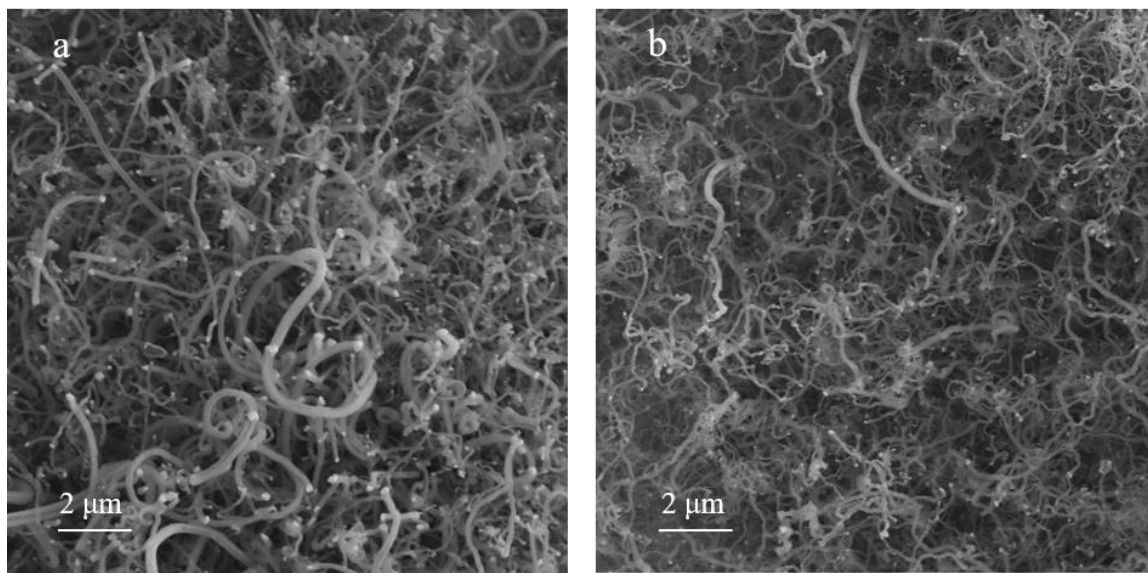


Figure 7.8 SEM image of flame synthesis of CNTs grown on a silicon wafer using 10 mMole/L  $\text{FeCl}_3$  seeding solution (a), and 1 mMole/L  $\text{FeCl}_3$  seeding solution (b).

To improve the quality of CNTs, size-controlled and well-dispersed catalytic nanoparticles are essential. Hydroxylamine has been used in controlling the size of iron oxide nanoparticles for SWNTs growth on quartz because amines are known to be mild reducing agents [150]. 2 mMole/L ethylenediamine ( $\text{C}_2\text{H}_4(\text{NH}_2)_2$ ) is added into 1 mMole/L  $\text{FeCl}_3$  solution to control the size and number density of the nanoparticles. Such seeding process enables the growth of entangled CNTs with nanoparticles on the tips (see Fig. 7.9a). The diameters of CNTs are on the order of 10 nm, implying a significant

decrease in the size of catalytic nanoparticles. However, the lengths of CNTs are much shorter than that from previous results. This result can be due to a lower growth rate for smaller catalysts. When the growth time is increased from 10 min to 20 min, the number density and length of CNTs are increased (see Fig. 7.9b)

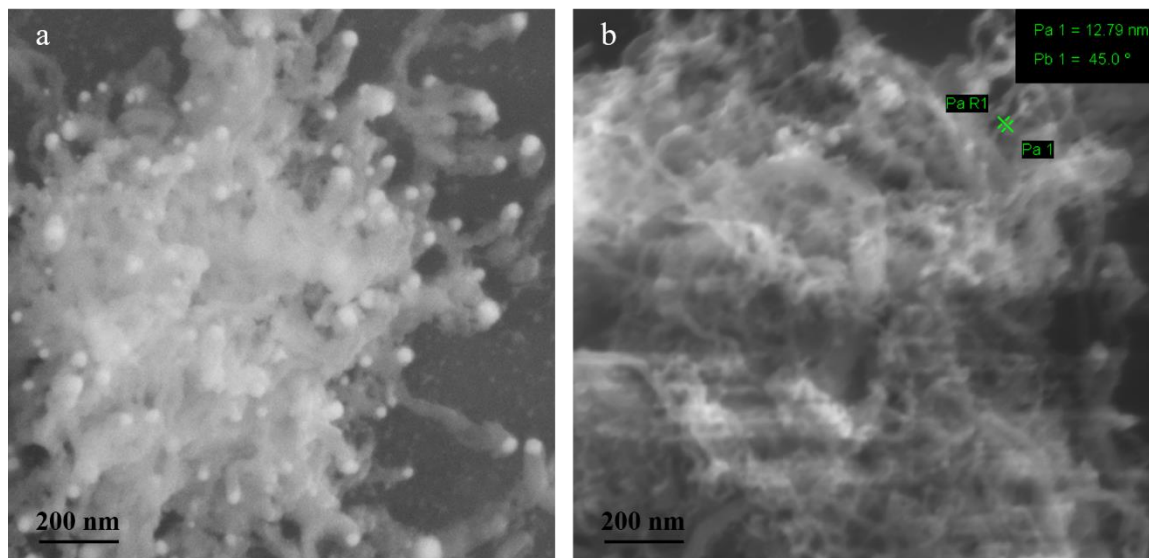


Figure 7.9 SEM image of CNTs grown on silicon wafers using 1 mMole/L  $\text{FeCl}_3$  and 2 mMole/L ethylenediamine ( $\text{C}_2\text{H}_4(\text{NH}_2)_2$ ) seeding solution for 10-min growth (a), and 20-min growth (b).

By reducing the concentration of  $\text{FeCl}_3$  from 1 mMole/L to 0.1 mMole/L and  $\text{C}_2\text{H}_4(\text{NH}_2)_2$  from 2 mMole/L to 0.2 mMole/L, a very dispersed growth of CNTs is observed (see Fig 7.10). The diameter of CNTs remains on the order of 10 nm, while the length is on the order of 100 nm for 10-min growth duration. This result suggests that the number density of catalyst decreases significantly along with the further reduction in the concentration of seeding solution. Based on previous calculations of Gibbs free energy

(see Table 7.2), iron metal catalysts are converted to  $\text{Fe}_2\text{O}_3$  nanoparticles spontaneously at CNT growth temperatures (550-850 °C) in the presence of  $\text{H}_2\text{O}$ ,  $\text{CO}$ , and  $\text{CO}_2$ . The formation of oxides, known as catalyst poisoning, can decrease the growth rate of CNTs [83]. By decreasing the concentration of seeding solution, the dense particle films transform to dispersed small particle films, leading to a much slower growth rate of CNTs. This result may be because the small-size catalytic particles are easier to be deactivated through the formation of oxide layers. Elemental analysis is performed on the sample using energy dispersive X-ray spectroscopy (EDS) on SEM. The high atomic percentage of  $\text{O}_2$  confirms the existence of large quantities of iron oxides on  $\text{Si}/\text{SiO}_2$  substrate (see Table 7.3). In CVD processes, the reaction chamber is normally vacuum sealed to prevent oxidation of the catalyst. However, the high flux of combustion gases ( $\text{H}_2\text{O}$ ,  $\text{CO}$ ,  $\text{CO}_2$ ) in flame synthesis makes it challenging to grow SWNTs by only reducing the size of catalysts.

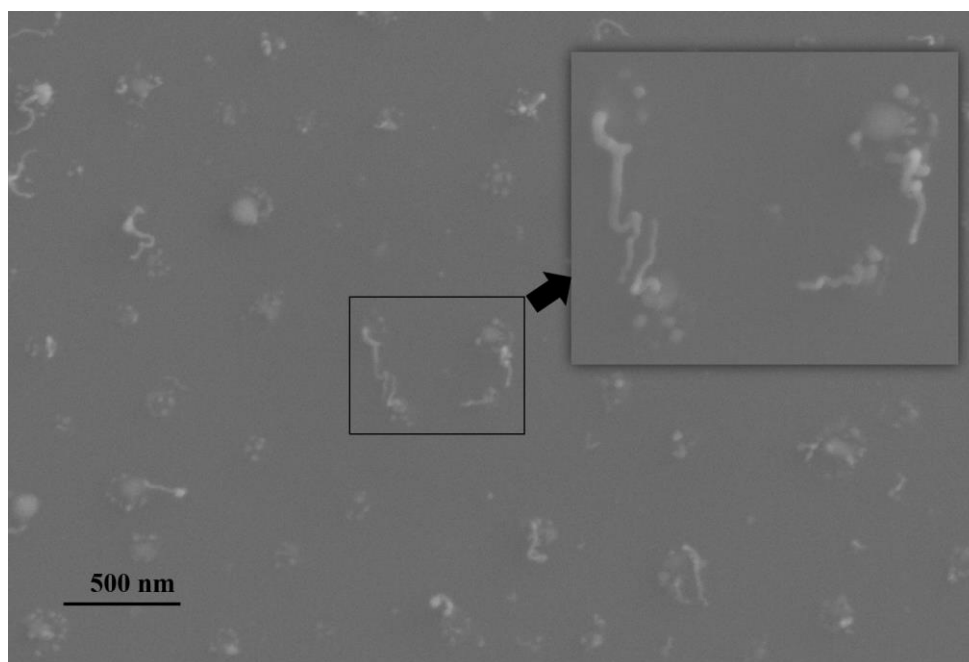


Figure 7.10 SEM image of CNTs grown on silicon wafers using 0.1 mMole/L  $\text{FeCl}_3$  and 0.2 mMole/L ethylenediamine ( $\text{C}_2\text{H}_4(\text{NH}_2)_2$ ) seeding solution. The top-right inset is an enlarged image of the selected area.

Table 7.3 Elemental analysis using EDS on SEM.

Element	Weight%	Atomic%
C	1.64	3.79
O	34.12	59.02
Fe	53.53	26.52
Si	10.17	10.02
Na	0.54	0.65

#### 7.3.2.2 CNT growth using Co-Mo co-catalyst

Some non-active catalysts have been used as co-catalysts to improve CNT growth. Among them, molybdenum is an important co-catalyst for iron and cobalt to form SWNTs [82]. Molybdenum is completely inactive for CNT growth while cobalt is unselective for

SWNTs and MWNTs. Molybdenum can help stabilizing  $\text{Co}^{2+}$  ions and prevent cobalt from sintering in the reduced state and forming large metal aggregates [82]. Vertically aligned SWNTs have been achieved using cobalt-molybdenum (Co-Mo) catalyst in an alcohol CVD process [83]. A similar seeding recipe is employed in this work. The catalyst is deposited on a Si/SiO<sub>2</sub> substrate by dip-coating the substrate in a Co-Mo acetate solution (both 0.01 wt.% in methanol) and calcining at 400 °C. Prior to growth, the substrate is first reduced in hydrogen m-IDFs at 800 °C. Ethylene is used as a substitution for ethanol, which is used in the aforementioned CVD study, because gas-phase precursor is preferred by our flame synthesis setup.

After 10-min growth, both CNTs clusters and distinct CNTs are observed on the substrate (see Fig. 7.11). The catalytic particles are well-dispersed. However, CNTs tend to grow on larger particles, and no CNTs grow on the smaller particles. Similar to iron, cobalt can spontaneously react with CO and CO<sub>2</sub> to form cobalt oxide (CoO) at the temperature range from 550 °C to 850 °C, according to Gibbs free energy calculations (see Table 7.4). Oxidation of cobalt in the CO-CO<sub>2</sub> mixture at high temperature has been reported [160]. Therefore, the dispersed small catalysts can be poisoned by the post-flame gases. The lifetime of catalysts is less than 1 min in conventional hydrocarbon CVD synthesis of CNTs because the process involves two competing reaction pathways: synthesis of CNTs and carbon coating of catalysts (deactivation) [161]. The main catalyst poisoning in CVD is the formation of carbides that completely encapsulate metal particles. However, in CVD-like flame synthesis, the deactivation of catalysts can be the oxidation

layers induced by CO and CO<sub>2</sub>, which are two main products of hydrocarbon combustion. The growth condition of CNT is very critical because dispersed small catalytic particles (<100 nm) are poisoned in the post-flame gases very fast, which decreases the growth rate of CNT significantly. This could be the reason why dense CNT forests have not been reported in flame synthesis using CVD-type solution seeding method.

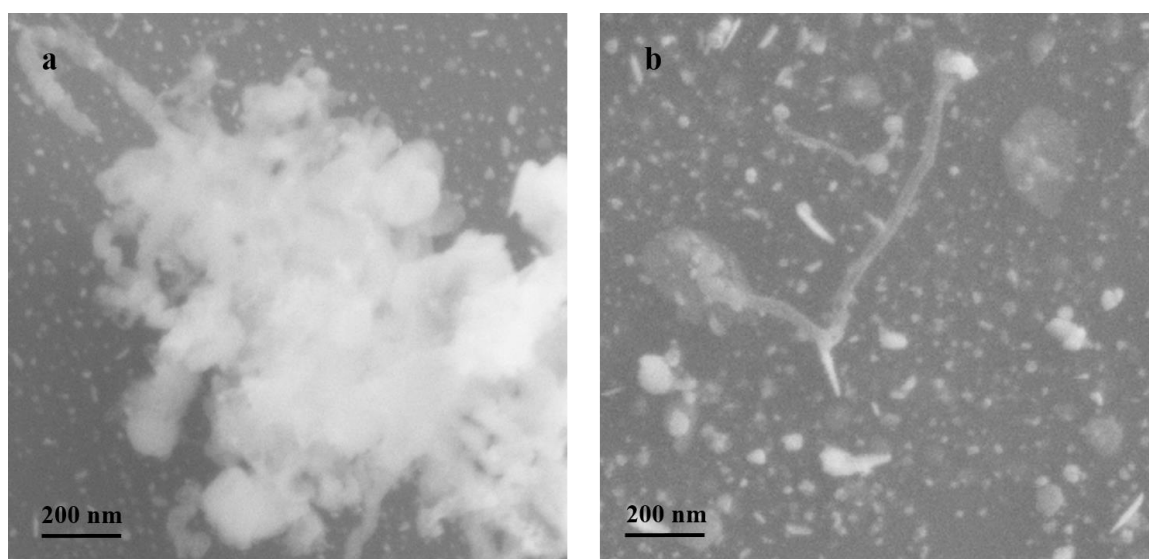


Figure 7.11 SEM image of CNTs cluster (a) and distinct CNTs (b) grown on silicon wafers using Co-Mo catalyst.

Table 7.4 Gibbs free energies of reactions, calculated with thermochemical data from NIST-JANAF tables (1998) at 1 atm, for the investigated growth of CoO.

T (K)	T (°C)	$\Delta G^\circ$ (kJ/mol) Co(s) + H <sub>2</sub> O(g) -> CoO(s)+ H <sub>2</sub> (g)	$\Delta G^\circ$ (kJ/mol) Co(s) + CO <sub>2</sub> (g) -> CoO(s)+CO(g)	$\Delta G^\circ$ (kJ/mol) Co(s) + CO(g) -> CoO(s)+C(s)
800	527	-26.289	36.044	5.29
900	627	-27.874	34.123	21.207
1000	727	-29.339	32.36	37.024
1100	827	-30.724	30.617	52.766



#### 7.4 Concluding Remarks

The role of substrate material and temperature on flame synthesis of iron oxides and CNTs is investigated. At low temperature (500 °C),  $\alpha$ -Fe<sub>2</sub>O<sub>3</sub> nanoparticle films are grown on type 304, 304L, and 316L stainless steels (SS). At high temperature (850 °C), the growth of  $\gamma$ -Fe<sub>2</sub>O<sub>3</sub> nanocrystals is observed on type 304L and 316L SS, while the growth of CNTs is observed on type 304 SS. The higher innate carbon content of 304 SS plays an important role in the formation of carbides, which can break up the substrate surface, leading to carbon fibers and CNTs growing on the freshly exposed iron nanoparticles. By employing a low-to-high-temperature growth step (from 500 °C to 850 °C), the growth of CNTs and  $\gamma$ -Fe<sub>2</sub>O<sub>3</sub> nanocomposites occurs on 304 SS. This flame technique enables a tunable manufacturing method for producing Fe<sub>2</sub>O<sub>3</sub> nanoparticles, CNTs, and their composites.

CNTs grown on non-metal substrate is demonstrated using CVD-type solution seeding methods. Metal catalysts such as Fe, Co, and Mo are deposited on Si/SiO<sub>2</sub> substrate through a dip-coating process. Different seeding recipes are investigated. Using high-concentration FeCl<sub>3</sub> aqueous solution (0.1-1 mMole/L), number dense and entangled MWNTs are observed. The number density and diameter of CNTs decrease along with the number density and size of catalytic nanoparticles. The morphology of metal catalysts is controlled by the concentration of seeding solution and reducing agents such as ethylenediamine. However, the growth rate of CNTs also decreases significantly when the particle size of catalysts decreases because of the formation of oxides poisoning

the catalysts. A recipe of Co-Mo co-catalyst used in alcohol CVD for vertically aligned SWNTs is also investigated in this work. However, only some CNT clusters and distinct CNT growth are observed. Unlike CVD, small-sized and well-dispersed catalytic nanoparticles do not lead to the efficient growth of CNTs. The high flux and large partial pressures of CO and CO<sub>2</sub> in the post-flame gases are inevitable oxidizers for metal catalysts in the temperature range (from 500 °C to 850 °C) of CNTs growth. The small and dispersed metal seeds have a much shorter lifetime of catalytic activity. Therefore, SWNTs forest remains a challenge for open-atmosphere flame synthesis using pure solution seeding methods.

## Chapter 8

### 8. Conclusions

#### 8.1 Summary of Results

Nanostructured carbon materials have attracted great research attention since the discovery of fullerenes and CNTs. In 2004, graphene was isolated and characterized for the first time by Andre Geim and Konstantin Novoselov at University of Manchester. These allotropes of carbon are formed by  $sp^2$ -bonded carbon atoms and define a new class of low-dimensional materials. A graphene layer, a two-dimensional (2D) nanomaterial, is the basic structural element of zero-dimensional (0D) fullerenes, one-dimensional (1D) nanotubes, and three-dimensional (3D) graphite. Nanostructured carbon materials exhibit exceptional electrical, mechanical, photonic, and chemical properties; and therefore, a number of research works have been focused on the synthesis method of such materials. This thesis investigates the controllable fabrication of 1D CNTs and 2D graphene films using novel flame synthesis.

The remarkable physical and chemical properties of graphene enable applications in advanced electronics, energy devices, sensors, and membranes. Graphene's unique conical band structure and ballistic electron transport at room temperature make it the most promising electronic material in the post-silicon era. Because of its high optical

transmittance and mechanical strength, graphene can be applied in flexible displays and touch screens. In recent years, graphene-based functional membranes have made great progress in applications such as water desalination, DNA sequencing, and rechargeable batteries. The main hurdle preventing graphene from commercial applications is the lack of viable and economical production methods for graphene with specified qualities suitable for different applications. Nowadays, chemical vapor deposition (CVD) can produce high-quality graphene over large areas (in one dimension, e.g., roll-to-roll). However, for some applications like ultrafiltering membranes, a “low-quality” graphene with a certain degree of defects is needed. In current approaches, a CVD-synthesized pristine graphene requires a series of modifications, which significantly increase the cost and difficulty of continuous large-scale production. Therefore, there is an urgent need for developing different synthesis methods to meet the demand of specific applications.

Flame synthesis is a robust method, currently used for the production of large-quantity nanoparticles, such as titania, silica, and carbon black. Its main advantages include scalability, fast processing time, and inherent high-temperature process at low costs. Flame-aerosol synthesis of CNTs has been studied for decades using different flame configurations with various catalysts. However, the growth of CNT films on insulating materials using flame synthesis has been limited. CNTs attached to insulators are required by many electronic applications, like field-emission transistors, and now is mainly produced by CVD. Thus, a fundamental study of the CVD-type flame synthesis of CNTs is required to understand the growth mechanism of CNTs in flames.

Unlike the extensive work on flame synthesis of CNTs, very limited work has been done on graphene growth using flame processes. In 2011, few-layer graphene was produced by using two different flame configurations: a dual flame setup and a multiple inverse-diffusion flames setup. The later one offers a scalable way to grow graphene films on copper, nickel, and Cu-Ni alloy in open environments. Flames can provide both the essential high temperature and carbon species needed for graphene growth, leading to an efficient and versatile process. Additionally, the open-atmosphere flame process has higher potential than CVD in the large-scale continuous production of graphene at an affordable cost. However, the synthesis of mono- and bi-layer graphene is still challenging because of the breakdown of copper's "self-limiting" mechanism at elevated pressure.

A modified multi-element inverse-diffusion flames setup is employed in this work to synthesize graphene and CNTs. The setup provides radially uniform profiles of temperature and chemical species in the downstream of the flames suitable for the parametric study of growth conditions. Separate delivery tubes can directly inject precursors into the post-combustion regime at desired temperatures, providing another degree of freedom in the parameters. Compared with previous flame configurations, the main advantage of this novel design is that hydrocarbon precursor decomposition is decoupled from the flame dynamics, enabling a more precise control of precursor properties, which is critical for high-quality graphene growth.

A systematic study of the key parameters influencing graphene growth, including substrate material (Ni, Cu, Si), temperature (750 °C to 1000 °C), hydrocarbon precursor ( $\text{CH}_4$ ,  $\text{C}_2\text{H}_4$ ), flow rate ratio ( $J_{\text{CH}_4}/J_{\text{H}_2} = 1/20$  to  $1/350$ ), and growth time (5 to 20 min) is conducted in this work. Bilayer graphene is produced on copper under a condition of 1000 °C and low methane-to-hydrogen ratio ( $\sim 1/100$ ). However, on nickel substrate, only few-layer graphene is observed in the temperature range from 750 °C to 1000 °C because of the different growth mechanism involved. In order to achieve monolayer graphene, a post-growth hydrogen annealing is applied to remove the adlayers of graphene. At a high temperature ( $\sim 1000$  °C), hydrogen exhibits a strong interaction with weak carbon bonds and dangling bonds. Monolayer graphene is achieved by etching away the adlayers of bilayer graphene in the post-growth-process. Moreover, such phenomenon offers the opportunity to tailor the quality of graphene films by etching weak carbon bonds at growth fronts within adlayers and defective areas.

Graphene grown on copper substrates of different purities exhibits different levels of defects, as characterized by the Raman spectra. Substrate-induced defects are observed on low-purity copper because of the impurity contents. Defective graphene ( $I_{\text{D}}/I_{\text{G}} \sim 0.6$ ) can be produced on 99.8% copper intentionally. The impact of hydrogen annealing on graphene samples with different substrate materials (Cu, Ni, Si) and  $I_{\text{D}}/I_{\text{G}}$  is investigated. A significant etching phenomenon is observed on graphene containing large amounts of defects regardless the substrate materials. For typical flame-synthesized defective graphene ( $I_{\text{D}}/I_{\text{G}} \sim 0.6$ ) supported on copper, the  $I_{\text{D}}/I_{\text{G}}$  increases to  $\sim 1$  and  $\sim 1.2$ , after 5 min

and 10 min hydrogen annealing, respectively. Highly defective graphene ( $I_D/I_G > 1$ ) has great potential in ion selective membrane applications. Other preparation methods require additional ion irradiation treatment on pristine graphene, which is not suitable for large-scale production. In this work, a flame-synthesis method to produce highly defective graphene with tunable defects is demonstrated. As-synthesized samples are fabricated into membranes for permeance and electrical I-V tests. The good ion selection properties of the films are conducive for separation membrane applications such as water desalination. Highly-defective graphene sample also exhibits a series of band gaps near 1.4eV based on preliminary UV-Vis spectroscopy.

The transitional growth of iron oxide nanoparticles to CNTs is studied using stainless-steel substrates. On stainless steel (SS),  $\alpha$ -Fe<sub>2</sub>O<sub>3</sub> nanoparticle films are observed at low temperature (500 °C). At high temperature (850 °C),  $\gamma$ -Fe<sub>2</sub>O<sub>3</sub> nanocrystals are observed on type 304L and 316L SS, while CNTs are observed on type 304 SS. Because of the higher innate carbon content of 304 SS, carbides are formed that can break up the substrate surface, exposing fresh iron that form nanoparticles, catalyzing carbon-fiber and CNT growth. The growth of CNTs and  $\gamma$ -Fe<sub>2</sub>O<sub>3</sub> nanocomposites on 304 SS is achieved by employing a low-to-high-temperature step condition (from 500 °C to 850 °C).

CNTs are grown on Si/SiO<sub>2</sub> by depositing metal catalysts such as Fe, Co, and Mo on the substrate using seeding methods generally employed in CVD synthesis of CNTs. The density, diameter, and growth rate of CNTs are primarily controlled by the morphology of the catalysts. The size and density of the catalysts are determined by the concentration

of the seeding solutions and reducing agents such as ethylenediamine. Dense and entangled MWNTs occur at high-concentrations of  $\text{FeCl}_3$  aqueous solution (0.1-1 mMole/L). The catalytic activity of catalysts reduces significantly, as the size decreases since the formation of oxides can deactivate the metal catalysts. A cobalt-molybdenum co-catalyst recipe is employed in this work. Unlike in CVD where SWNT forests occur, only some CNT clusters and distinct CNT growth are observed using our flame-based setup. The small-sized and well-dispersed catalytic nanoparticles are poisoned rapidly by the high flux of CO and  $\text{CO}_2$  in the post-flame gases in the temperature range (from 500 °C to 850 °C). The low growth rate of CNT in flame makes it very challenging to grow SWNTs forest using pure solution seeding methods.

The modified m-IDFs synthesis setup is a strong research tool to study the growth conditions of nanostructured carbon materials. It offers many degrees of freedom in precisely controlling the synthesis parameters including temperature, chemical species, and flow configuration. Moreover, the method has no problem in scaling-up and is capable of continuous operation. Compared with CVD processes, such technique has advantages in processing time and cost. More importantly, the setup is not confined to a vacuum chamber, presenting the capability of processing nanostructured carbon materials over large areas.



## 8.2 Suggestions for Future Work

Even though flame synthesis of monolayer graphene has been demonstrated; large crystalline monolayer graphene has not been achieved. A major growth factor is the initial nucleation density controlling the domain size of graphene, which seems to be affected by pressure. By lowering the pressure, the growth of large-domain monolayer graphene should be enabled by matching the fluxes with that used in low-pressure CVD. The m-IDFs burner can be a drop-in technology into current CVD reactors, with the advantage of not needing electrical heating, which is energy expensive and has contamination problems.

By employing hydrogen annealing, highly defective graphene films can be directly synthesized on copper. Although Raman spectroscopy can provide a measure of the defect level in graphene layers, it cannot give details of the defects (pores, overlaps, small domains, vacancies, etc.). To understand better the characteristics of the defective graphene samples, advanced imaging techniques like aberration-corrected STEM are needed. Additional investigation of the mechanisms of hydrogen etching on graphene to produce highly-defective graphene with different properties would be invaluable in tailoring the films for various applications.

Other two-dimensional (2D) materials, such as h-BN, bismuth telluride, and transition metal dichalcogenides have attracted enormous attention in recent years. Artificially stacked vertical heterostructures (see Fig. 8.1) can provide properties that can be modified to fit a broad range of possible applications [151]. Randomly stacked layers

of graphene and h-BN have been reported using liquid phase exfoliation methods [38]. It is desirable to expand flame synthesis to such novel nanostructures in combination with other methods such as CVD and pulse laser deposition (PLD). By employing PLD, bismuth telluride ( $\text{Bi}_2\text{Te}_3$ ) thin films have been grown on flame-synthesized graphene sample in our lab. This result proves the potential of fabricating complex artificially stacked 2D materials. However, proper characterization methods are needed to study the inter-layer structures.

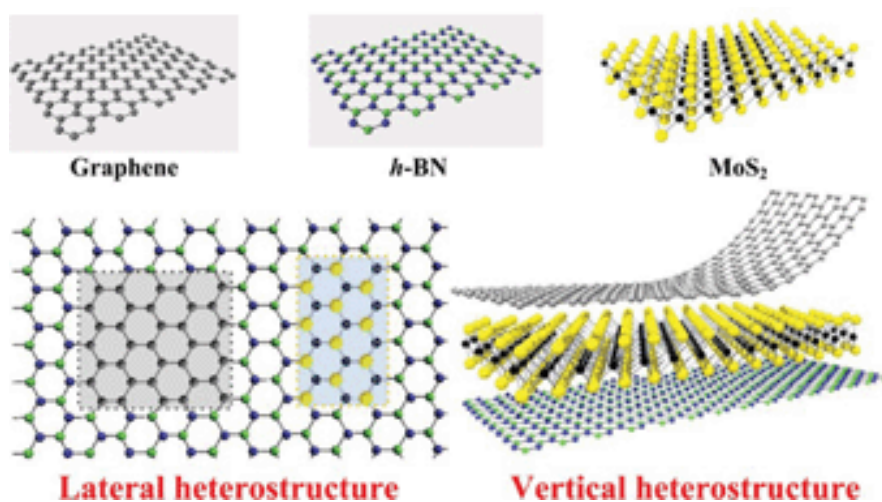


Figure 8.1 A scheme of graphene, h-BN and  $\text{MoS}_2$  lateral and vertical heterostructures (reproduced with caption from [30]).

The high fluxes of combustion gases make the deactivation of catalysts more likely than for low-flux CVD processes. Gas-phase synthesis of CNTs comprises competing pathways, i.e., CNT growth and catalyst deactivation. In order to grow SWNTs or vertically well-aligned CNTs on  $\text{Si/SiO}_2$ , the deactivation mechanism of metal catalysts in

flame synthesis obliges additional investigation. Other catalytic materials and deposition methods can be examined. Finally, Other nanostructured carbon materials, such as nanodiamonds, fullerenes, and graphene-CNT hybrid structures should be studied using flame synthesis.

## References

- [1] “Handbook of Carbon, Graphite, Diamonds and Fullerenes - 1st Edition.” [Online]. Available: <https://www.elsevier.com/books/handbook-of-carbon-graphite-diamonds-and-fullerenes/pierson/978-0-8155-1339-1>. [Accessed: 06-Feb-2017].
- [2] A. M. K. Esawi and M. M. Farag, “Carbon nanotube reinforced composites: Potential and current challenges,” *Materials & Design*, vol. 28, no. 9, pp. 2394–2401, 2007.
- [3] W. Merchan-Merchan, A. V. Saveliev, L. Kennedy, and W. C. Jimenez, “Combustion synthesis of carbon nanotubes and related nanostructures,” *Progress in Energy and Combustion Science*, vol. 36, no. 6, pp. 696–727, Dec. 2010.
- [4] N. K. Memon *et al.*, “Flame synthesis of graphene films in open environments,” *Carbon*, vol. 49, no. 15, pp. 5064–5070, Dec. 2011.
- [5] A. R. Oganov, R. J. Hemley, R. M. Hazen, and A. P. Jones, “Structure, Bonding, and Mineralogy of Carbon at Extreme Conditions,” *Reviews in Mineralogy and Geochemistry*, vol. 75, no. 1, pp. 47–77, Jan. 2013.
- [6] “The rise of graphene,” *Nat Mater*, vol. 6, no. 3, pp. 183–191, Mar. 2007.
- [7] J. B. Oostinga, H. B. Heersche, X. Liu, A. F. Morpurgo, and L. M. K. Vandersypen, “Gate-induced insulating state in bilayer graphene devices,” *Nat Mater*, vol. 7, no. 2, pp. 151–157, Feb. 2008.
- [8] J.-U. Lee, D. Yoon, H. Kim, S. W. Lee, and H. Cheong, “Thermal conductivity of suspended pristine graphene measured by Raman spectroscopy,” *Phys. Rev. B*, vol. 83, no. 8, p. 81419, Feb. 2011.
- [9] C. Lee, X. Wei, J. W. Kysar, and J. Hone, “Measurement of the Elastic Properties and Intrinsic Strength of Monolayer Graphene,” *Science*, vol. 321, no. 5887, pp. 385–388, Jul. 2008.
- [10] R. R. Nair *et al.*, “Fine Structure Constant Defines Visual Transparency of Graphene,” *Science*, vol. 320, no. 5881, pp. 1308–1308, Jun. 2008.

- [11] V. Singh, D. Joung, L. Zhai, S. Das, S. I. Khondaker, and S. Seal, "Graphene based materials: Past, present and future," *Progress in Materials Science*, vol. 56, no. 8, pp. 1178–1271, Oct. 2011.
- [12] K. R. Paton *et al.*, "Scalable production of large quantities of defect-free few-layer graphene by shear exfoliation in liquids," *Nat Mater*, vol. 13, no. 6, pp. 624–630, Jun. 2014.
- [13] S. ( 1 ) Bhaviripudi, M. s. ( 1 Dresselhaus 3 ), J. ( 1 ) Kong, and X. ( 2 ) Jia, "Role of kinetic factors in chemical vapor deposition synthesis of uniform large area graphene using copper catalyst," *Nano Letters*, vol. 10, no. 10, pp. 4128–4133, 13 2010.
- [14] S. Bae *et al.*, "Roll-to-roll production of 30-inch graphene films for transparent electrodes," *Nat Nano*, vol. 5, no. 8, pp. 574–578, Aug. 2010.
- [15] Z.-J. Wang *et al.*, "Direct observation of graphene growth and associated copper substrate dynamics by in situ scanning electron microscopy," *ACS Nano*, vol. 9, no. 2, pp. 1506–1519, Feb. 2015.
- [16] X. Li *et al.*, "Transfer of Large-Area Graphene Films for High-Performance Transparent Conductive Electrodes," *Nano Lett.*, vol. 9, no. 12, pp. 4359–4363, Dec. 2009.
- [17] P. Sun, K. Wang, and H. Zhu, "Recent Developments in Graphene-Based Membranes: Structure, Mass-Transport Mechanism and Potential Applications," *Adv. Mater.*, vol. 28, no. 12, pp. 2287–2310, Mar. 2016.
- [18] S. J. Heerema and C. Dekker, "Graphene nanodevices for DNA sequencing," *Nat Nano*, vol. 11, no. 2, pp. 127–136, Feb. 2016.
- [19] H. Dai, "Carbon nanotubes: opportunities and challenges," *Surface Science*, vol. 500, no. 1–3, pp. 218–241, Mar. 2002.
- [20] E. T. Thostenson, Z. Ren, and T.-W. Chou, "Advances in the science and technology of carbon nanotubes and their composites: a review," *Composites Science and Technology*, vol. 61, no. 13, pp. 1899–1912, Oct. 2001.
- [21] S. Li, Y. Ren, P. Biswas, and S. D. Tse, "Flame aerosol synthesis of nanostructured materials and functional devices: Processing, modeling, and diagnostics," *Progress in Energy and Combustion Science*, vol. 55, pp. 1–59, Jul. 2016.

- [22] Z. Li *et al.*, “Flame synthesis of few-layered graphene/graphite films,” *Chem. Commun.*, vol. 47, no. 12, pp. 3520–3522, Mar. 2011.
- [23] M. J. Height, “Flame synthesis of carbon nanotubes and metallic nanomaterials,” Thesis, Massachusetts Institute of Technology, 2003.
- [24] C. R. Brundle, C. A. Evans, and S. Wilson, *Encyclopedia of Materials Characterization: Surfaces, Interfaces, Thin Films*. Gulf Professional Publishing, 1992.
- [25] A. C. Ferrari, “Raman spectroscopy of graphene and graphite: Disorder, electron–phonon coupling, doping and nonadiabatic effects,” *Solid State Communications*, vol. 143, no. 1–2, pp. 47–57, Jul. 2007.
- [26] L. M. Malard, M. A. Pimenta, G. Dresselhaus, and M. S. Dresselhaus, “Raman spectroscopy in graphene,” *Physics Reports*, vol. 473, no. 5–6, pp. 51–87, Apr. 2009.
- [27] K. S. Kim *et al.*, “Large-scale pattern growth of graphene films for stretchable transparent electrodes,” *Nature*, vol. 457, no. 7230, pp. 706–710, Feb. 2009.
- [28] R. Muñoz and C. Gómez-Aleixandre, “Review of CVD Synthesis of Graphene,” *Chem. Vap. Deposition*, vol. 19, no. 10–11–12, pp. 297–322, Dec. 2013.
- [29] S. P. Surwade *et al.*, “Water desalination using nanoporous single-layer graphene,” *Nat Nano*, vol. 10, no. 5, pp. 459–464, May 2015.
- [30] H. Wang, F. Liu, W. Fu, Z. Fang, W. Zhou, and Z. Liu, “Two-dimensional heterostructures: fabrication, characterization, and application,” *Nanoscale*, vol. 6, no. 21, pp. 12250–12272, Oct. 2014.
- [31] S. E. Pratsinis, “Flame aerosol synthesis of ceramic powders,” *Progress in Energy and Combustion Science*, vol. 24, no. 3, pp. 197–219, 1998.
- [32] W. Y. Teoh, “A Perspective on the Flame Spray Synthesis of Photocatalyst Nanoparticles,” *Materials*, vol. 6, no. 8, pp. 3194–3212, Jul. 2013.
- [33] A. H. Castro Neto, F. Guinea, N. M. R. Peres, K. S. Novoselov, and A. K. Geim, “The electronic properties of graphene,” *Rev. Mod. Phys.*, vol. 81, no. 1, pp. 109–162, Jan. 2009.

- [34] P. Avouris, “Graphene: Electronic and Photonic Properties and Devices,” *Nano Lett.*, vol. 10, no. 11, pp. 4285–4294, 2010.
- [35] X. Wang, L. Zhi, and K. Müllen, “Transparent, Conductive Graphene Electrodes for Dye-Sensitized Solar Cells,” *Nano Lett.*, vol. 8, no. 1, pp. 323–327, 2007.
- [36] K. S. Novoselov *et al.*, “Electric Field Effect in Atomically Thin Carbon Films,” *Science*, no. 5696, p. 666, 2004.
- [37] H. W. Kroto, J. R. Heath, S. C. O’Brien, R. F. Curl, and R. E. Smalley, “C<sub>60</sub>: Buckminsterfullerene,” *Nature*, vol. 318, no. 6042, pp. 162–163, Nov. 1985.
- [38] P. M. Ajayan, *Artificially Stacked Atomic Layers: Toward New van der Waals Solids*. .
- [39] Y. Zhang, Y.-W. Tan, H. L. Stormer, and P. Kim, “Experimental observation of the quantum Hall effect and Berry’s phase in graphene,” *Nature*, vol. 438, no. 7065, pp. 201–204, Nov. 2005.
- [40] K. S. Novoselov *et al.*, “Two-dimensional gas of massless Dirac fermions in graphene,” *Nature*, vol. 438, no. 7065, pp. 197–200, Nov. 2005.
- [41] E. V. Castro *et al.*, “Biased Bilayer Graphene: Semiconductor with a Gap Tunable by the Electric Field Effect,” *Phys. Rev. Lett.*, vol. 99, no. 21, p. 216802, Nov. 2007.
- [42] J.-H. Chen, C. Jang, S. Xiao, M. Ishigami, and M. S. Fuhrer, “Intrinsic and extrinsic performance limits of graphene devices on SiO<sub>2</sub>,” *Nat Nano*, vol. 3, no. 4, pp. 206–209, Apr. 2008.
- [43] A. Akturk and N. Goldsman, “Electron transport and full-band electron-phonon interactions in graphene,” *Journal of Applied Physics*, vol. 103, no. 5, p. 53702, Mar. 2008.
- [44] A. A. Balandin *et al.*, “Superior thermal conductivity of single-layer graphene,” *Nano Lett.*, vol. 8, no. 3, pp. 902–907, Mar. 2008.
- [45] W. Cai *et al.*, “Thermal Transport in Suspended and Supported Monolayer Graphene Grown by Chemical Vapor Deposition,” *Nano Letters*, vol. 10, pp. 1645–1651, May 2010.
- [46] X. Xu *et al.*, “Length-dependent thermal conductivity in suspended single-layer graphene,” *Nat Commun*, vol. 5, p. 3689, Apr. 2014.

- [47] K. F. Mak, M. Y. Sfeir, Y. Wu, C. H. Lui, J. A. Misewich, and T. F. Heinz, "Measurement of the Optical Conductivity of Graphene," *Phys. Rev. Lett.*, vol. 101, no. 19, p. 196405, Nov. 2008.
- [48] N. Liu, F. Luo, H. Wu, Y. Liu, C. Zhang, and J. Chen, "One-Step Ionic-Liquid-Assisted Electrochemical Synthesis of Ionic-Liquid-Functionalized Graphene Sheets Directly from Graphite," *Adv. Funct. Mater.*, vol. 18, no. 10, pp. 1518–1525, 2008.
- [49] Y. Hernandez *et al.*, "High-yield production of graphene by liquid-phase exfoliation of graphite," *Nat Nano*, vol. 3, no. 9, pp. 563–568, Sep. 2008.
- [50] J. Penuelas *et al.*, "Surface morphology and characterization of thin graphene films on SiC vicinal substrate," *Phys. Rev. B*, vol. 79, no. 3, p. 33408, Jan. 2009.
- [51] K. V. Emtsev *et al.*, "Towards wafer-size graphene layers by atmospheric pressure graphitization of silicon carbide," *Nat Mater*, vol. 8, no. 3, pp. 203–207, Mar. 2009.
- [52] I. Pletikosić *et al.*, "Dirac Cones and Minigaps for Graphene on Ir(111)," *Phys. Rev. Lett.*, vol. 102, no. 5, p. 56808, Feb. 2009.
- [53] Q. Yu, J. Lian, S. Siriponglert, H. Li, Y. P. Chen, and S.-S. Pei, "Graphene segregated on Ni surfaces and transferred to insulators," *Applied Physics Letters*, vol. 93, no. 11, p. 113103, Sep. 2008.
- [54] X. Li *et al.*, "Large-Area Synthesis of High-Quality and Uniform Graphene Films on Copper Foils," *Science*, vol. 324, no. 5932, pp. 1312–1314, Jun. 2009.
- [55] X. Li *et al.*, "Graphene Films with Large Domain Size by a Two-Step Chemical Vapor Deposition Process," *Nano Lett.*, vol. 10, no. 11, pp. 4328–4334, 2010.
- [56] X. Hu, T. Björkman, H. Lipsanen, L. Sun, and A. V. Krasheninnikov, "Solubility of Boron, Carbon, and Nitrogen in Transition Metals: Getting Insight into Trends from First-Principles Calculations," *The Journal of Physical Chemistry Letters*, vol. 6, no. 16, pp. 3263–3268, Aug. 2015.
- [57] Y. Yao, Z. Li, Z. Lin, K.-S. Moon, J. Agar, and C. Wong, "Controlled Growth of Multilayer, Few-Layer, and Single-Layer Graphene on Metal Substrates," *J. Phys. Chem. C*, vol. 115, no. 13, pp. 5232–5238, Apr. 2011.



- [58] X. Li *et al.*, “Large-Area Graphene Single Crystals Grown by Low-Pressure Chemical Vapor Deposition of Methane on Copper,” *J. Am. Chem. Soc.*, vol. 133, no. 9, pp. 2816–2819, 2011.
- [59] A. W. Robertson and J. H. Warner, “Hexagonal Single Crystal Domains of Few-Layer Graphene on Copper Foils,” *Nano Lett.*, vol. 11, no. 3, pp. 1182–1189, Mar. 2011.
- [60] C. ( 1 ) Mattevi, H. ( 1 ) Kim, and M. ( 1 Chhowalla 2 ), “A review of chemical vapour deposition of graphene on copper,” *Journal of Materials Chemistry*, vol. 21, no. 10, pp. 3324–3334, 14 2011.
- [61] N. Woehrl, O. Ochedowski, S. Gottlieb, K. Shibasaki, and S. Schulz, “Plasma-enhanced chemical vapor deposition of graphene on copper substrates,” *AIP Advances*, vol. 4, no. 4, p. 47128, Apr. 2014.
- [62] A. Dato, V. Radmilovic, Z. Lee, J. Phillips, and M. Frenklach, “Substrate-free gas-phase synthesis of graphene sheets,” *Nano Lett.*, vol. 8, no. 7, pp. 2012–2016, Jul. 2008.
- [63] Y. Zhang *et al.*, “Direct observation of a widely tunable bandgap in bilayer graphene,” *Nature*, vol. 459, no. 7248, pp. 820–823, Jun. 2009.
- [64] T. Ohta, A. Bostwick, T. Seyller, K. Horn, and E. Rotenberg, “Controlling the Electronic Structure of Bilayer Graphene,” *Science*, vol. 313, no. 5789, pp. 951–954, Aug. 2006.
- [65] B. Guo, L. Fang, B. Zhang, and J. R. Gong, “Graphene Doping: A Review,” *Insciencs J.*, vol. 1, no. 2, pp. 80–89, 2011.
- [66] D. Wei, Y. Liu, Y. Wang, H. Zhang, L. Huang, and G. Yu, “Synthesis of N-Doped Graphene by Chemical Vapor Deposition and Its Electrical Properties,” *Nano Lett.*, vol. 9, no. 5, pp. 1752–1758, May 2009.
- [67] “Bismuth doping of graphene,” *Appl. Phys. Lett.*, vol. 96, no. 8, p. 81914, Feb. 2010.
- [68] Y.-M. Lin *et al.*, “Wafer-Scale Graphene Integrated Circuit,” *Science*, vol. 332, no. 6035, pp. 1294–1297, Jun. 2011.

- [69] J. Song, Z. Yu, M. L. Gordin, and D. Wang, “Advanced Sulfur Cathode Enabled by Highly Crumpled Nitrogen-Doped Graphene Sheets for High-Energy-Density Lithium–Sulfur Batteries,” *Nano Lett.*, vol. 16, no. 2, pp. 864–870, Feb. 2016.
- [70] Z. Fan *et al.*, “Asymmetric Supercapacitors Based on Graphene/MnO<sub>2</sub> and Activated Carbon Nanofiber Electrodes with High Power and Energy Density,” *Adv. Funct. Mater.*, vol. 21, no. 12, pp. 2366–2375, Jun. 2011.
- [71] J. S. Bunch *et al.*, “Impermeable Atomic Membranes from Graphene Sheets,” *Nano Lett.*, vol. 8, no. 8, pp. 2458–2462, Aug. 2008.
- [72] S. C. O’Hern *et al.*, “Selective Ionic Transport through Tunable Subnanometer Pores in Single-Layer Graphene Membranes,” *Nano Lett.*, vol. 14, no. 3, pp. 1234–1241, Mar. 2014.
- [73] H. Du, J. Li, J. Zhang, G. Su, X. Li, and Y. Zhao, “Separation of Hydrogen and Nitrogen Gases with Porous Graphene Membrane,” *J. Phys. Chem. C*, vol. 115, no. 47, pp. 23261–23266, Dec. 2011.
- [74] G. G. Tibbetts, “Why are carbon filaments tubular?,” *Journal of Crystal Growth*, vol. 66, no. 3, pp. 632–638, May 1984.
- [75] S. Iijima, “Helical microtubules of graphitic carbon,” *Nature*, vol. 354, no. 6348, pp. 56–58, Nov. 1991.
- [76] J. Hone, M. Whitney, C. Piskoti, and A. Zettl, “Thermal conductivity of single-walled carbon nanotubes,” *Phys. Rev. B*, vol. 59, no. 4, pp. R2514–R2516, Jan. 1999.
- [77] M.-F. Yu, O. Lourie, M. J. Dyer, K. Moloni, T. F. Kelly, and R. S. Ruoff, “Strength and Breaking Mechanism of Multiwalled Carbon Nanotubes Under Tensile Load,” *Science*, vol. 287, no. 5453, pp. 637–640, Jan. 2000.
- [78] S. Hong and S. Myung, “Nanotube Electronics: A flexible approach to mobility,” *Nat Nano*, vol. 2, no. 4, pp. 207–208, Apr. 2007.
- [79] Z. Shi *et al.*, “Large scale synthesis of single-wall carbon nanotubes by arc-discharge method,” *Journal of Physics and Chemistry of Solids*, vol. 61, no. 7, pp. 1031–1036, Jul. 2000.

- [80] T. Guo, P. Nikolaev, A. Thess, D. T. Colbert, and R. E. Smalley, "Catalytic growth of single-walled nanotubes by laser vaporization," *Chemical Physics Letters*, vol. 243, no. 1, pp. 49–54, Sep. 1995.
- [81] L. Yu, L. Sui, Y. Qin, F. Du, and Z. Cui, "Catalytic synthesis of carbon nanofibers and nanotubes by the pyrolysis of acetylene with iron nanoparticles prepared using a hydrogen-arc plasma method," *Materials Letters*, vol. 63, no. 20, pp. 1677–1679, Aug. 2009.
- [82] A.-C. Dupuis, "The catalyst in the CCVD of carbon nanotubes—a review," *Progress in Materials Science*, vol. 50, no. 8, pp. 929–961, Nov. 2005.
- [83] S. Maruyama, E. Einarsson, Y. Murakami, and T. Edamura, "Growth process of vertically aligned single-walled carbon nanotubes," *Chemical Physics Letters*, vol. 403, no. 4–6, pp. 320–323, Feb. 2005.
- [84] S. H. Jin *et al.*, "Using nanoscale thermocapillary flows to create arrays of purely semiconducting single-walled carbon nanotubes," *Nat Nano*, vol. 8, no. 5, pp. 347–355, May 2013.
- [85] S.-F. Zheng, J.-S. Hu, L.-S. Zhong, W.-G. Song, L.-J. Wan, and Y.-G. Guo, "Introducing Dual Functional CNT Networks into CuO Nanomicrospheres toward Superior Electrode Materials for Lithium-Ion Batteries," *Chem. Mater.*, vol. 20, no. 11, pp. 3617–3622, Jun. 2008.
- [86] Z. Jian *et al.*, "Core–Shell-Structured CNT@RuO<sub>2</sub> Composite as a High-Performance Cathode Catalyst for Rechargeable Li–O<sub>2</sub> Batteries," *Angew. Chem. Int. Ed.*, vol. 53, no. 2, pp. 442–446, Jan. 2014.
- [87] D. J. Li *et al.*, "Molybdenum Sulfide/N-Doped CNT Forest Hybrid Catalysts for High-Performance Hydrogen Evolution Reaction," *Nano Lett.*, vol. 14, no. 3, pp. 1228–1233, Mar. 2014.
- [88] T. Johannessen, J. R. Jensen, M. Mosleh, J. Johansen, U. Quaade, and H. Livbjerg, "Product Design and Engineering Flame Synthesis of Nanoparticles," *Chemical Engineering Research and Design*, vol. 82, no. 11, pp. 1444–1452, Nov. 2004.
- [89] P. Roth, "Particle synthesis in flames," *Proceedings of the Combustion Institute*, vol. 31, no. 2, pp. 1773–1788, Jan. 2007.

- [90] P. M. Rao and X. Zheng, "Rapid catalyst-free flame synthesis of dense, aligned  $\alpha$ -Fe<sub>2</sub>O<sub>3</sub> nanoflake and CuO nanoneedle arrays," *Nano Lett.*, vol. 9, no. 8, pp. 3001–3006, Aug. 2009.
- [91] L. Cai, P. M. Rao, and X. Zheng, "Morphology-controlled flame synthesis of single, branched, and flower-like  $\alpha$ -MoO<sub>3</sub> nanobelt arrays," *Nano Lett.*, vol. 11, no. 2, pp. 872–877, Feb. 2011.
- [92] J. B. Howard, J. T. McKinnon, Y. Makarovskiy, A. L. Lafleur, and M. E. Johnson, "Fullerenes C<sub>60</sub> and C<sub>70</sub> in flames," *Nature*, vol. 352, no. 6331, pp. 139–141, Jul. 1991.
- [93] L. Yuan, K. Saito, W. Hu, and Z. Chen, "Ethylene flame synthesis of well-aligned multi-walled carbon nanotubes," *Chemical Physics Letters*, vol. 346, no. 1–2, pp. 23–28, Sep. 2001.
- [94] F. Xu, X. Liu, and S. D. Tse, "Synthesis of carbon nanotubes on metal alloy substrates with voltage bias in methane inverse diffusion flames," *Carbon*, vol. 44, no. 3, pp. 570–577, Mar. 2006.
- [95] W. Merchan-Merchan, A. Saveliev, L. A. Kennedy, and A. Fridman, "Formation of carbon nanotubes in counter-flow, oxy-methane diffusion flames without catalysts," *Chemical Physics Letters*, vol. 354, no. 1–2, pp. 20–24, Mar. 2002.
- [96] R. L. Vander Wal, L. J. Hall, and G. M. Berger, "Proceedings of the Combustion Institute The chemistry of premixed flame synthesis of carbon nanotubes using supported catalysts," *Proceedings of the Combustion Institute*, vol. 29, no. 1, pp. 1079–1085, Jan. 2002.
- [97] M. J. Height, J. B. Howard, J. W. Tester, and J. B. Vander Sande, "Flame synthesis of single-walled carbon nanotubes," *Carbon*, vol. 42, no. 11, pp. 2295–2307, 2004.
- [98] C. J. Unrau, R. L. Axelbaum, P. Biswas, and P. Fraundorf, "Synthesis of single-walled carbon nanotubes in oxy-fuel inverse diffusion flames with online diagnostics," *Proceedings of the Combustion Institute*, vol. 31, no. 2, pp. 1865–1872, Jan. 2007.
- [99] N. K. Memon, S. D. Tse, M. Chhowalla, and B. H. Kear, "Role of substrate, temperature, and hydrogen on the flame synthesis of graphene films," *Proceedings of the Combustion Institute*, vol. 34, no. 2, pp. 2163–2170, 2013.

- [100] N. K. Memon, F. Xu, G. Sun, S. J. B. Dunham, B. H. Kear, and S. D. Tse, “Flame synthesis of carbon nanotubes and few-layer graphene on metal-oxide spinel powders,” *Carbon*, vol. 63, pp. 478–486, Nov. 2013.
- [101] N. K. Memon, B. H. Kear, and S. D. Tse, “Transition between graphene-film and carbon-nanotube growth on Nickel alloys in open-atmosphere flame synthesis,” *Chemical Physics Letters*, vol. 570, pp. 90–94, May 2013.
- [102] A. C. Ferrari and J. Robertson, “Interpretation of Raman spectra of disordered and amorphous carbon,” *Phys. Rev. B*, vol. 61, no. 20, pp. 14095–14107, May 2000.
- [103] A. Reina *et al.*, “Large Area, Few-Layer Graphene Films on Arbitrary Substrates by Chemical Vapor Deposition,” *Nano Lett.*, vol. 9, no. 1, pp. 30–35, Jan. 2009.
- [104] S. Xing, W. Wu, Y. Wang, J. Bao, and S.-S. Pei, “Kinetic study of graphene growth: Temperature perspective on growth rate and film thickness by chemical vapor deposition,” *Chemical Physics Letters*, vol. 580, pp. 62–66, Aug. 2013.
- [105] Q. Li *et al.*, “Growth of Adlayer Graphene on Cu Studied by Carbon Isotope Labeling,” *Nano Lett.*, vol. 13, no. 2, pp. 486–490, Feb. 2013.
- [106] J. Chen *et al.*, “Oxygen-Aided Synthesis of Polycrystalline Graphene on Silicon Dioxide Substrates,” *J. Am. Chem. Soc.*, vol. 133, no. 44, pp. 17548–17551, Nov. 2011.
- [107] B. Liu *et al.*, “Importance of Oxygen in the Metal-Free Catalytic Growth of Single-Walled Carbon Nanotubes from SiO<sub>x</sub> by a Vapor–Solid–Solid Mechanism,” *J. Am. Chem. Soc.*, vol. 133, no. 2, pp. 197–199, Jan. 2011.
- [108] M. Qi *et al.*, “Hydrogen Kinetics on Scalable Graphene Growth by Atmospheric Pressure Chemical Vapor Deposition with Acetylene,” *J. Phys. Chem. C*, vol. 117, no. 27, pp. 14348–14353, Jul. 2013.
- [109] Z. Luo *et al.*, “Pyridinic N doped graphene: synthesis, electronic structure, and electrocatalytic property,” *Journal of Materials Chemistry*, vol. 21, no. 22, pp. 8038–8044, 2011.
- [110] M. E. Ramón *et al.*, “CMOS-Compatible Synthesis of Large-Area, High-Mobility Graphene by Chemical Vapor Deposition of Acetylene on Cobalt Thin Films,” *ACS Nano*, vol. 5, no. 9, pp. 7198–7204, Sep. 2011.

- [111] C. Wang, B. Xiao, and Y. Ding, “Theoretical investigation on the healing mechanism of divacancy defect in graphene growth by reaction with ethylene and acetylene,” *New Journal of Chemistry*, vol. 37, no. 3, pp. 640–645, 2013.
- [112] “Chemical Vapor Deposition Repair of Graphene Oxide: A Route to Highly Conductive Graphene Monolayers (PDF Download Available),” *ResearchGate*.
- [113] J. Zhang *et al.*, “CVD growth of large area and uniform graphene on tilted copper foil for high performance flexible transparent conductive film,” *J. Mater. Chem.*, vol. 22, no. 35, pp. 18283–18290, Aug. 2012.
- [114] X. Liu, M. E. Smith, and S. D. Tse, “In situ Raman characterization of nanoparticle aerosols during flame synthesis,” *Appl. Phys. B*, vol. 100, no. 3, pp. 643–653, Sep. 2010.
- [115] H. Wang *et al.*, “Controllable Synthesis of Submillimeter Single-Crystal Monolayer Graphene Domains on Copper Foils by Suppressing Nucleation,” *J. Am. Chem. Soc.*, vol. 134, no. 8, pp. 3627–3630, Feb. 2012.
- [116] I. Vlassiuk *et al.*, “Graphene Nucleation Density on Copper: Fundamental Role of Background Pressure,” *J. Phys. Chem. C*, vol. 117, no. 37, pp. 18919–18926, Sep. 2013.
- [117] I. Vlassiuk *et al.*, “Role of hydrogen in chemical vapor deposition growth of large single-crystal graphene,” *ACS Nano*, vol. 5, no. 7, pp. 6069–6076, Jul. 2011.
- [118] Y. Yao and C. Wong, “Monolayer graphene growth using additional etching process in atmospheric pressure chemical vapor deposition,” *Carbon*, vol. 50, no. 14, pp. 5203–5209, Nov. 2012.
- [119] J. Chen *et al.*, “Self healing of defected graphene,” *Applied Physics Letters*, vol. 102, no. 10, p. 103107, Mar. 2013.
- [120] L. G. Cançado *et al.*, “Quantifying Defects in Graphene via Raman Spectroscopy at Different Excitation Energies,” *Nano Lett.*, vol. 11, no. 8, pp. 3190–3196, Aug. 2011.
- [121] M. M. Lucchese *et al.*, “Quantifying ion-induced defects and Raman relaxation length in graphene,” *Carbon*, vol. 48, no. 5, pp. 1592–1597, Apr. 2010.

- [122] B. Hu *et al.*, “Epitaxial growth of large-area single-layer graphene over Cu(1 1 1)/sapphire by atmospheric pressure CVD,” *Carbon*, vol. 50, no. 1, pp. 57–65, Jan. 2012.
- [123] E. McCann and V. I. Fal’ko, “Landau level degeneracy and quantum Hall effect in a graphite bilayer,” *Physical Review Letters*, vol. 96, no. 8, Mar. 2006.
- [124] O. Cretu, A. V. Krashenninnikov, J. A. Rodríguez-Manzo, L. Sun, R. M. Nieminen, and F. Banhart, “Migration and Localization of Metal Atoms on Strained Graphene,” *Phys. Rev. Lett.*, vol. 105, no. 19, p. 196102, Nov. 2010.
- [125] W. Yuan, J. Chen, and G. Shi, “Nanoporous graphene materials,” *Materials Today*, vol. 17, no. 2, pp. 77–85, Mar. 2014.
- [126] M. H. Griep, E. Sandoz-Rosado, T. M. Tumlin, and E. Wetzel, “Enhanced Graphene Mechanical Properties through Ultrasooth Copper Growth Substrates,” *Nano Lett.*, vol. 16, no. 3, pp. 1657–1662, Mar. 2016.
- [127] W. T. Mozet, “Investigation of fundamental growth mechanisms in pulsed laser deposition synthesis of nanostructured materials,” Rutgers University - Graduate School - New Brunswick, 2016.
- [128] M. Wojdyr, “Fityk: a general-purpose peak fitting program,” *J Appl Cryst, J Appl Crystallogr*, vol. 43, no. 5, pp. 1126–1128, Oct. 2010.
- [129] W. S. Leong, C. T. Nai, and J. T. L. Thong, “What Does Annealing Do to Metal–Graphene Contacts?,” *Nano Lett.*, vol. 14, no. 7, pp. 3840–3847, Jul. 2014.
- [130] A. T. Murdock *et al.*, “Controlling the Orientation, Edge Geometry, and Thickness of Chemical Vapor Deposition Graphene,” *ACS Nano*, vol. 7, no. 2, pp. 1351–1359, Feb. 2013.
- [131] H. Gao, L. Wang, J. Zhao, F. Ding, and J. Lu, “Band Gap Tuning of Hydrogenated Graphene: H Coverage and Configuration Dependence,” *J. Phys. Chem. C*, vol. 115, no. 8, pp. 3236–3242, Mar. 2011.
- [132] A. . Pennington, A. . Okonmah, D. . Munoz, G. Tsilomelekis, and F. . Celik, “Unravelling the Compositional Changes in P25-TiO<sub>2</sub> During Pretreatment by Differential Diffuse Reflectance Spectral Analysis, Manuscript Prepared,” *Journal of Physical Chemistry C*.

- [133] R. Su, S. F. Lin, D. Q. Chen, and G. H. Chen, "Study on the Absorption Coefficient of Reduced Graphene Oxide Dispersion," *J. Phys. Chem. C*, vol. 118, no. 23, pp. 12520–12525, Jun. 2014.
- [134] C.-K. Chang *et al.*, "Band Gap Engineering of Chemical Vapor Deposited Graphene by in Situ BN Doping," *ACS Nano*, vol. 7, no. 2, pp. 1333–1341, Feb. 2013.
- [135] F. J. Tölle, M. Fabritius, and R. Mülhaupt, "Emulsifier-Free Graphene Dispersions with High Graphene Content for Printed Electronics and Freestanding Graphene Films," *Adv. Funct. Mater.*, vol. 22, no. 6, pp. 1136–1144, Mar. 2012.
- [136] R. C. Rollings, A. T. Kuan, and J. A. Golovchenko, "Ion selectivity of graphene nanopores," *Nature Communications*, vol. 7, p. ncomms11408, Apr. 2016.
- [137] "Single-layer MoS<sub>2</sub> nanopores as nanopower generators : Nature : Nature Research." [Online]. Available: <http://www.nature.com/nature/journal/v536/n7615/full/nature18593.html?foxtrotcallback=true>. [Accessed: 07-Sep-2017].
- [138] H. W. Kim *et al.*, "Selective Gas Transport Through Few-Layered Graphene and Graphene Oxide Membranes," *Science*, vol. 342, no. 6154, pp. 91–95, Oct. 2013.
- [139] C. Sun *et al.*, "Mechanisms of Molecular Permeation through Nanoporous Graphene Membranes," *Langmuir*, vol. 30, no. 2, pp. 675–682, Jan. 2014.
- [140] F. Xu, S. D. Tse, J. F. Al-Sharab, and B. H. Kear, "Flame synthesis of aligned tungsten oxide nanowires," *Applied Physics Letters*, vol. 88, no. 24, pp. 243115–243115–3, Jun. 2006.
- [141] Z. Dong, J. F. Al-Sharab, B. H. Kear, and S. D. Tse, "Combined Flame and Electrodeposition Synthesis of Energetic Coaxial Tungsten-Oxide/Aluminum Nanowire Arrays," *Nano Lett.*, vol. 13, no. 9, pp. 4346–4350, 2013.
- [142] F. Xu, X. Liu, S. D. Tse, F. Cosandey, and B. H. Kear, "Flame synthesis of zinc oxide nanowires," *Chemical Physics Letters*, vol. 449, no. 1–3, pp. 175–181, Nov. 2007.
- [143] F. Xu, H. Zhao, and S. D. Tse, "Carbon nanotube synthesis on catalytic metal alloys in methane/air counterflow diffusion flames," *Proceedings of the Combustion Institute*, vol. 31, no. 2, pp. 1839–1847, Jan. 2007.



- [144] C. Li, G. Fang, N. Liu, X. Yang, and X. Zhao, "Flame-synthesis of carbon nanotubes on silicon substrates and their field emission properties," *Diamond and Related Materials*, vol. 17, no. 6, pp. 1015–1020, Jun. 2008.
- [145] W. Hu *et al.*, "Growth of well-aligned carbon nanotube arrays on silicon substrates using porous alumina film as a nanotemplate," *Applied Physics Letters*, vol. 79, no. 19, pp. 3083–3085, Nov. 2001.
- [146] A. K. Gupta and M. Gupta, "Synthesis and surface engineering of iron oxide nanoparticles for biomedical applications," *Biomaterials*, vol. 26, no. 18, pp. 3995–4021, Jun. 2005.
- [147] A. S. Teja and P.-Y. Koh, "Synthesis, properties, and applications of magnetic iron oxide nanoparticles," *Progress in Crystal Growth and Characterization of Materials*, vol. 55, no. 1–2, pp. 22–45, Mar. 2009.
- [148] B. Guo and I. M. Kennedy, "Gas-Phase Flame Synthesis and Characterization of Iron Oxide Nanoparticles for Use in a Health Effects Study," *Aerosol Science and Technology*, vol. 41, no. 10, pp. 944–951, Aug. 2007.
- [149] K. Buyukhatipoglu and A. M. Clyne, "Controlled flame synthesis of  $\alpha\text{Fe}_2\text{O}_3$  and  $\text{Fe}_3\text{O}_4$  nanoparticles: effect of flame configuration, flame temperature, and additive loading," *J Nanopart Res*, vol. 12, no. 4, pp. 1495–1508, May 2010.
- [150] H. C. Choi *et al.*, "Efficient Formation of Iron Nanoparticle Catalysts on Silicon Oxide by Hydroxylamine for Carbon Nanotube Synthesis and Electronics," *Nano Lett.*, vol. 3, no. 2, pp. 157–161, Feb. 2003.
- [151] F. Froment, A. Tournié, and P. Colomban, "Raman identification of natural red to yellow pigments: ochre and iron-containing ores," *J. Raman Spectrosc.*, vol. 39, no. 5, pp. 560–568, May 2008.
- [152] "Raman microspectroscopy of some iron oxides and oxyhydroxides - de Faria - 1997 - Journal of Raman Spectroscopy - Wiley Online Library." [Online]. Available: [http://onlinelibrary.wiley.com/doi/10.1002/\(SICI\)1097-4555\(199711\)28:11%3C873::AID-JRS177%3E3.0.CO;2-B/abstract](http://onlinelibrary.wiley.com/doi/10.1002/(SICI)1097-4555(199711)28:11%3C873::AID-JRS177%3E3.0.CO;2-B/abstract). [Accessed: 27-Aug-2016].
- [153] P. C. J. Graat and M. A. J. Somers, "Simultaneous determination of composition and thickness of thin iron-oxide films from XPS Fe 2p spectra," *Applied Surface Science*, vol. 100, pp. 36–40, Jul. 1996.

- [154] P. M. Rao and X. Zheng, "Unique magnetic properties of single crystal  $\gamma$ -Fe<sub>2</sub>O<sub>3</sub> nanowires synthesized by flame vapor deposition," *Nano Lett.*, vol. 11, no. 6, pp. 2390–2395, Jun. 2011.
- [155] R. L. Vander Wal and L. J. Hall, "Carbon nanotube synthesis upon stainless steel meshes," *Carbon*, vol. 41, no. 4, pp. 659–672, 2003.
- [156] A. Aharoni, E. H. Frei, and M. Schieber, "Some properties of  $\gamma$ -Fe<sub>2</sub>O<sub>3</sub> obtained by hydrogen reduction of  $\alpha$ -Fe<sub>2</sub>O<sub>3</sub>," *Journal of Physics and Chemistry of Solids*, vol. 23, no. 6, pp. 545–554, Jun. 1962.
- [157] Y. Watanabe, K. Ishii, N. Ishikawa, K. Furuya, and M. Kato, "In situ observation of transformation in  $\alpha$ -Fe<sub>2</sub>O<sub>3</sub> under hydrogen implantation," *J. Phys.: Condens. Matter*, vol. 14, no. 49, p. 13643, 2002.
- [158] S. Fan, M. G. Chapline, N. R. Franklin, T. W. Tombler, A. M. Cassell, and H. Dai, "Self-Oriented Regular Arrays of Carbon Nanotubes and Their Field Emission Properties," *Science*, vol. 283, no. 5401, pp. 512–514, Jan. 1999.
- [159] K. Kuwana, H. Endo, K. Saito, D. Qian, R. Andrews, and E. A. Grulke, "Catalyst deactivation in CVD synthesis of carbon nanotubes," *Carbon*, vol. 43, no. 2, pp. 253–260, 2005.
- [160] F. S. Pettit and J. B. Wagner, "Oxidation of cobalt in CO-CO<sub>2</sub> mixtures in the temperature range 920°C–1200°C," *Acta Metallurgica*, vol. 12, no. 1, pp. 41–47, Jan. 1964.
- [161] T. Yamada *et al.*, "Revealing the Secret of Water-Assisted Carbon Nanotube Synthesis by Microscopic Observation of the Interaction of Water on the Catalysts," *Nano Lett.*, vol. 8, no. 12, pp. 4288–4292, Dec. 2008.
- [162] K. S. Novoselov, V. I. Fal'ko, L. Colombo, P. R. Gellert, M. G. Schwab, and K. Kim, "A roadmap for graphene," *Nature*, vol. 490, no. 7419, pp. 192–200, Oct. 2012.